Université d'Ottawa · University of Ottawa

THE USE OF RADARSAT-1 IMAGERY FOR LITHOLOGICAL AND STRUCTURAL MAPPING IN THE CANADIAN HIGH ARCTIC

by

Simon Riopel

A Thesis

Submitted to the School of Graduate Studies and Research

in Partial Fulfillment of the Requirements for the

Degree of Master of Science in Earth Sciences

Ottawa-Carleton Geoscience Centre

Department of Earth Sciences

University of Ottawa

Ottawa, Ontario

0-612-57178-5

ABSTRACT

RADARSAT-1 images of the northern part of Axel Heiberg Island were acquired to define a selection of preferable beam modes for geological mapping in this cold and arid environment with locally rugged topography. Fine, Standard, and Extended High beam mode images with different resolutions, areas of coverage, look directions, incidence angles, and dates of acquisition were analyzed in this study. Major geological contacts in this part of the Sverdrup Basin and the Franklinian Mobile Belt are well identified in these images. Numerous post-Paleozoic tabular intrusive bodies were also identified. Although shadowing and other geometric effects were accentuated, structural features and lineaments were best highlighted in RADARSAT-1 images with higher incidence angles where less topographic displacement is present. Significant seasonal changes in radar image tone associated with localized melting of the active layer were clearly visible between winter and summer images.

RADARSAT-1 beam modes were successfully used to make stereo-pairs. Two overlapping images with the same look direction provided better results because of the parallax problem with opposite side-looking, particularly in areas with more rugged topography. Even though stereo-pairs work with a small angle of stereo intersection, it is preferable to have a larger angle to ensure the maximum parallax difference (e.g. 13° for S3/S7 stereo-pair). Standard stereo-pairs used for qualitative analysis and interpretation were also used to generate a Digital Elevation Model (DEM). DEM was used for quantitative planimetric and altimetric purposes, including orthorectification of RADARSAT-1 images and calculation of strike and dip.

The capability of RADARSAT-1 images to take images regardless of illumination and atmospheric conditions, and to produce stereo-pairs, DEM, integrated products and perspective images make it an innovative and important tool for geological investigation in the Canadian High Arctic.

RÉSUMÉ

Des images couvrant le secteur nord de l'île Axel Heiberg ont été acquises dans le but de choisir les meilleurs produits disponibles du satellite RADARSAT-1 pour la cartographie géologique dans cet environnement froid et aride où la topographie est relativement accidentée. Ces images acquises avec les faisceaux fin, standard et prolongé ont différentes résolutions, couvertures, directions de visée, angles d'incidence et dates d'acquisition. Les principaux contacts géologiques dans cette région du Bassin de Sverdrup et de la Zone Mobile Franklinienne sont identifiés sur ces images. De nombreuses intrusions tabulaires post-Paléozoïques ont été aussi identifiées. Même si des problèmes d'ombrage et des distorsions géométriques sont observés, les éléments structuraux et les linéaments sont davantage marqués dans les images acquises avec des angles d'incidence élevés où le repliement est restreint. Les variations saisonnières de la teinte des images associées à la fonte locale du mollisol sont clairement visibles lorsqu'on compare les images RADARSAT-1 acquises en hiver et en été.

Les images RADARSAT-1 peuvent être utilisées comme couples stéréoscopiques. Le couple stéréoscopique S3/S7 dont les images ont été acquises avec la même direction de visée pour limiter les problèmes de parallaxe dans les environnements où la topographie est relativement accidentée, comme c'est le cas dans la région d'étude. Même si la vision stéréoscopique est possible avec une petite différence entre les angles d'incidence des deux images, une grande différence est préférable pour assurer un maximum de parallaxe (i.e. 13° pour le couple S3/S7). Ce couple stéréoscopique a été utilisé pour l'analyse qualitative et l'interprétation ainsi que pour générer un modèle numérique d'altitude (MNA). Ce MNA a

permis une analyse planimétrique et altimétrique comme l'orthorectification d'images RADARSAT-1 et le calcul de direction et de pendage.

La capacité du satellite RADARSAT-1 d'acquérir des images indépendamment de l'illumination et des conditions métérologiques et la possibilité de générer à partir des images RADARSAT-1 des couples stéréoscopiques, des MNA, des produits intégrés ainsi que des images en perspective indique que RADARSAT-1 est un outil important et innovateur pour la cartographie géologique dans l'Arctique Canadien.

ACKNOWLEDGEMENTS

I would greatly acknowledged the following persons:

- Dr. André Desrochers for offered me this project and for helping me with various suggestions and revisions all along this two year research project.
- Dr. Marc D'Iorio for useful suggestions and revisions.
- Mr. Paul Budkewitsch for important discussions about this project and for providing the meteorological data.
- Dr. Benoit Beauchamp for important discussions, field photographs and an ortho-photo of the study area that help me understanding the geology of the northern part of Axel Heiberg Island.
- Dr. Ulrich Mayr of GSC-Calgary for providing a digital copy of the geological map of the Sverdrup Basin for the study area, not yet release.
- Dr. Thierry Toutin of CCRS and Mr. René Chénier of Consultants TGIS inc. for helpful discussions and the stereoscopic plotting of Ground Control Points (GCPs) with the DVP for the DEM generation.
- My life companion Dominique Henrie and my family for helping me to complete this project.

The RADARSAT-1 scenes used in this study are part of the Application Development and Research Opportunity, Project ID #87 sponsored by the Canadian Space Agency, Radarsat International and supported by the Canada Centre for Remote Sensing (CCRS). Finally, the CCRS for support and use of the Application Division Geology Laboratory, the Ministry of Education and Training for scholarships and the University of Ottawa for scholarships and teaching assistantships are also acknowledged.

TABLE OF CONTENTS

LIST OF FIGURES

LIST OF TABLES

INTRODUCTION

Introduction

Geological mapping in the Canadian Arctic has been, and is still, difficult due to various logistical and financial aspects. The large territory to cover and the short summer period further complicate traditional field campaigns. Because of these factors, remote sensing can significantly contribute to the geological mapping in these regions. This earth observation technique produces images from which it is possible to derive a regional preliminary geological map. Preliminary map can help the planning of future field campaigns and thereby reduces the cost and time required for a mapping project. The geologist is exposed to several problems, like atmospheric conditions and earth surface characteristics, when remote sensing images are used for geological mapping. The relative independence of RADARSAT-1 imagery to illumination and weather conditions is important in this arctic environment allowing to acquire images in the winter period when there is no illumination and no soil moisture component. The sensitivity of RADARSAT-1 satellite to topography, surface roughness and soil moisture contributes to make it an essential tool for present and future geological mapping, particularly in inaccessible and/or poorly documented and mapped regions. In addition, the low vegetation cover of the arctic environment results in a radar backscatter signal more influenced by the nature of the surficial deposits and the bedrock geology.

Objectives

The general purpose of this study is to evaluate the potential of RADARSAT-1 images for geological mapping in an arctic environment. The specific objectives are:

1. To describe the parameters influencing the radar backscatter in an arctic environment.
2. To assess lithological mapping at different scales using RADARSAT-1 images.
3. To evaluate structural mapping using RADARSAT-1 images.
4. To demonstrate the variety of products that can be derived from RADARSAT-1 images for geological mapping.
5. To apply a photogrammetric strike and dip calculation method using generated Digital Elevation Model (DEM) and RADARSAT-1 ortho-images.
6. To define a selection of preferable beam modes for geological mapping in a cold and arid environment with local rugged topography.

Methodology

In order to reach the above-mentioned objectives, the following products have been produced by the present author:

1. Georeferencing of ten RADARSAT-1 images using a polynomial method;
2. Generating a DEM from a RADARSAT-1 stereo-pair;
3. Orthorectificating two RADARSAT-1 images;
4. Creating derived products such as chromo-stereoscopic images, radar and geological map integrated images, as well as perspective images.
5. Calculating strike and dip using generated DEM and RADARSAT-1 ortho-images.

Thesis Format

This thesis is written in a scientific paper format. We have consciously chosen to write it in such a way to facilitate future publications of this research. Consequently, this document is not composed of the classical chapter headings usually found in scholar thesis. It is nevertheless divided into different sections, which are identified in the table of contents.

LOCATION OF STUDY

This study investigates in detail the northern part of Axel Heiberg Island located around 80° north and 92° west (Fig. 1). The study area is covered by a standard beam mode RADARSAT-1 image size (100km x 100km; Fig. 2). The Axel Heiberg Island forms part of the Queen Elizabeth Islands, a group of islands north of the Parry Channel in the Arctic Archipelago that covers 1,3 million km^2. An important percentage of the Canadian resources in petroleum, metals, and coal are present in the Arctic Archipelago. 17 hydrocarbon fields have been found in the Upper Triassic to Lower Cretaceous sandstones of the western Sverdrup Basin. One field has also been discovered in Devonian strata (Trettin, 1989). Major coal resources are located in the Upper Cretaceous-Paleogene Eureka Sound Group present in the eastern part of Axel Heiberg and in the west-central part of Ellesmere Islands (Trettin, 1989).

CLIMATE SETTING

The climate present in the Queen Elizabeth Islands is dry and arid because of the low annual precipitation as demonstrated by the 64 mm of annual precipitation recorded at the

Figure 1. Location map showing the northern part of the Queen Elizabeth Islands and the study area covering the extreme northern portion of Axel Heiberg Island (modified form Hearty *et al.*, 1996).

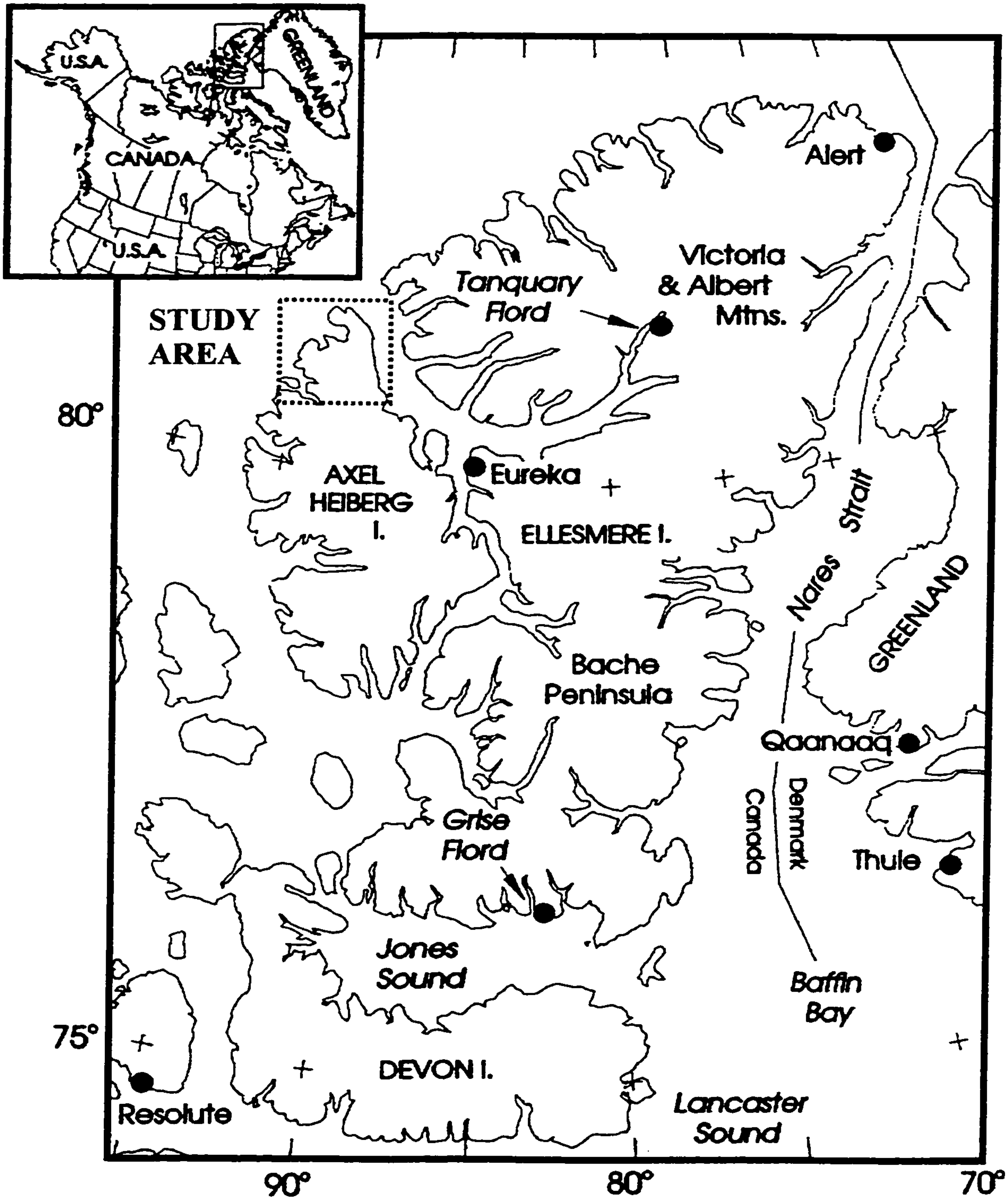
U.S.A.
CANADA
U.S.A.
GREENLAND
STUDY AREA
Alert
Victoria & Albert Mtns.
Tanquary Fiord
80°
AXEL HEIBERG I.
Eureka
ELLESMERE I.
Nares Strait
GREENLAND
Bache Peninsula
Qaanaaq
Canada
Denmark
Grise Fiord
Thule
Jones Sound
Baffin Bay
75°
DEVON I.
Resolute
Lancaster Sound
90°
80°
70°

Figure 2. Standard RADARSAT-1 image covering the entire study area and showing the location of the sub-images presented in this paper. The sub-images used in this thesis are shown by numbered red boxes and correspond to the figure names used in the text. The acquisition parameters are listed beside the RADARSAT-1 image.

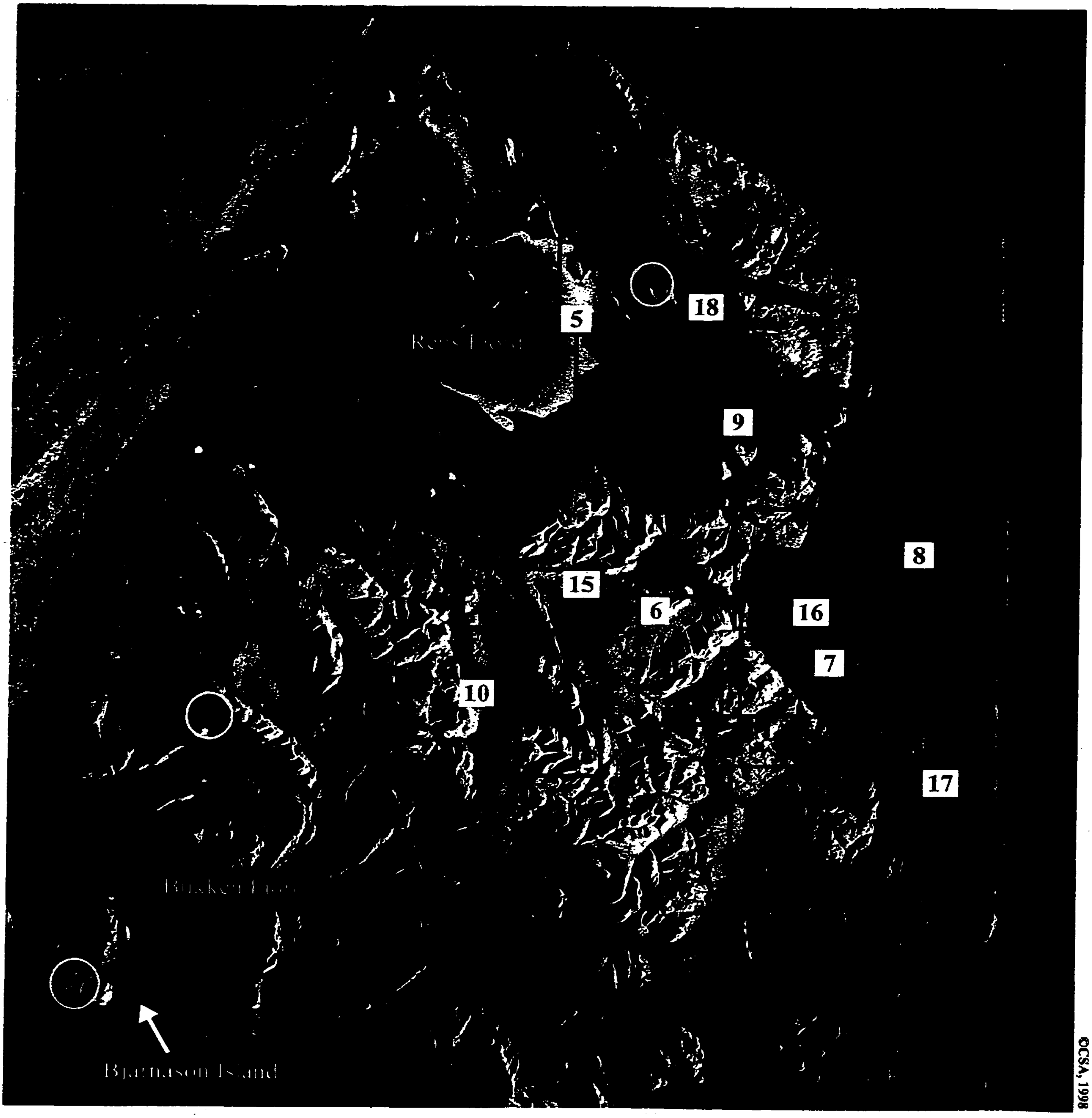

5
18
9
8
15
6
16
7
10
17
Bjarnason Island

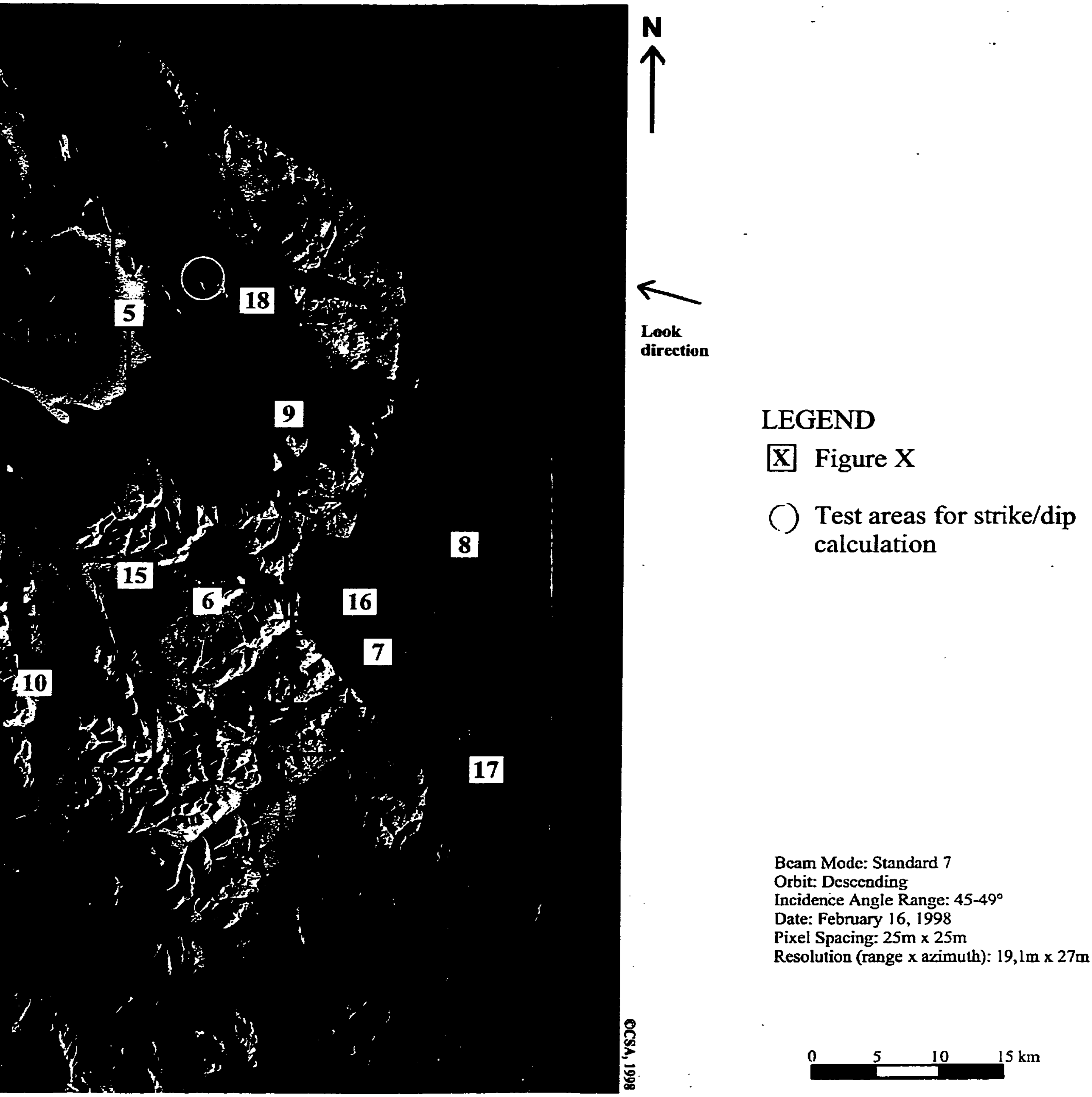
N
Look direction
5
18
9
8
15
6
16
7
10
17
©CSA, 1998
LEGEND
X Figure X
Test areas for strike/dip calculation
Beam Mode: Standard 7
Orbit: Descending
Incidence Angle Range: 45-49°
Date: February 16, 1998
Pixel Spacing: 25m x 25m
Resolution (range x azimuth): 19,1m x 27m
0 5 10 15 km

Eureka Weather Station (see Fig. 1; Lewkowicz and Duguay, 1999). The mean daily temperatures range from –16°C to –19°C explaining the permafrost presence in the Queen Elizabeth Islands (thickness of 500 meters near the Eureka Station; Hodgson, 1991). The permafrost, an all year long frozen layer, is overlaid by the active layer melting or freezing according to surface temperature variations (French, 1996). The active layer thickness measured around the Eureka Station range from 40 cm to 90 cm (Lewkowicz and Duguay, 1999). The vegetation present in the study area passes from shrub-herb transition in the southeastern part to entirely herbaceous in the northwestern part (Hodgson, 1991).

GEOLOGICAL SETTING

In the study area, two major geological provinces are present, the Franklinian Mobile Belt and the Sverdrup Basin (Fig. 3).

Franklinian Mobile Belt

This province is composed of rocks that range in age from Middle Proterozoic to Lower Devonian lying on the Archean to Lower Proterozoic metamorphic and plutonic basement and Lower to Upper Proterozoic sedimentary and volcanic succession of the Canadian Shield (Trettin, 1989). The Franklinian Mobile Belt comprises the Shelf Province, dominated by carbonates with clastics and evaporites, the Deep Water Basin dominated by sediment gravity flows, graptolitic mudrock and radiolarian chert and the Pearya Terrane composed of metamorphic, sedimentary and volcanic rocks (Trettin, 1991). The Deep Water Basin is further subdivided into a Sedimentary and a Sedimentary-Volcanic Subprovinces. The Sedimentary-Volcanic Subprovince constitutes the Clements Markham and Northern

Figure 3. This figure illustrates the major tectono-stratigraphic successions present in the northern part of Axel Heiberg Island: the Cambrian-Devonian succession of the Franklinian Mobile Belt (grey), the Carboniferous-Permian (blue), the Triassic-Cretaceous and the Cretaceous-Tertiary (green) successions of the Sverdrup Basin, and the Quaternary sediments (yellow). This figure was generating in SPANS 6.0 by reclassifying the more detailed digital geological map of the Sverdrup Basin (Mayr et al., 1998).

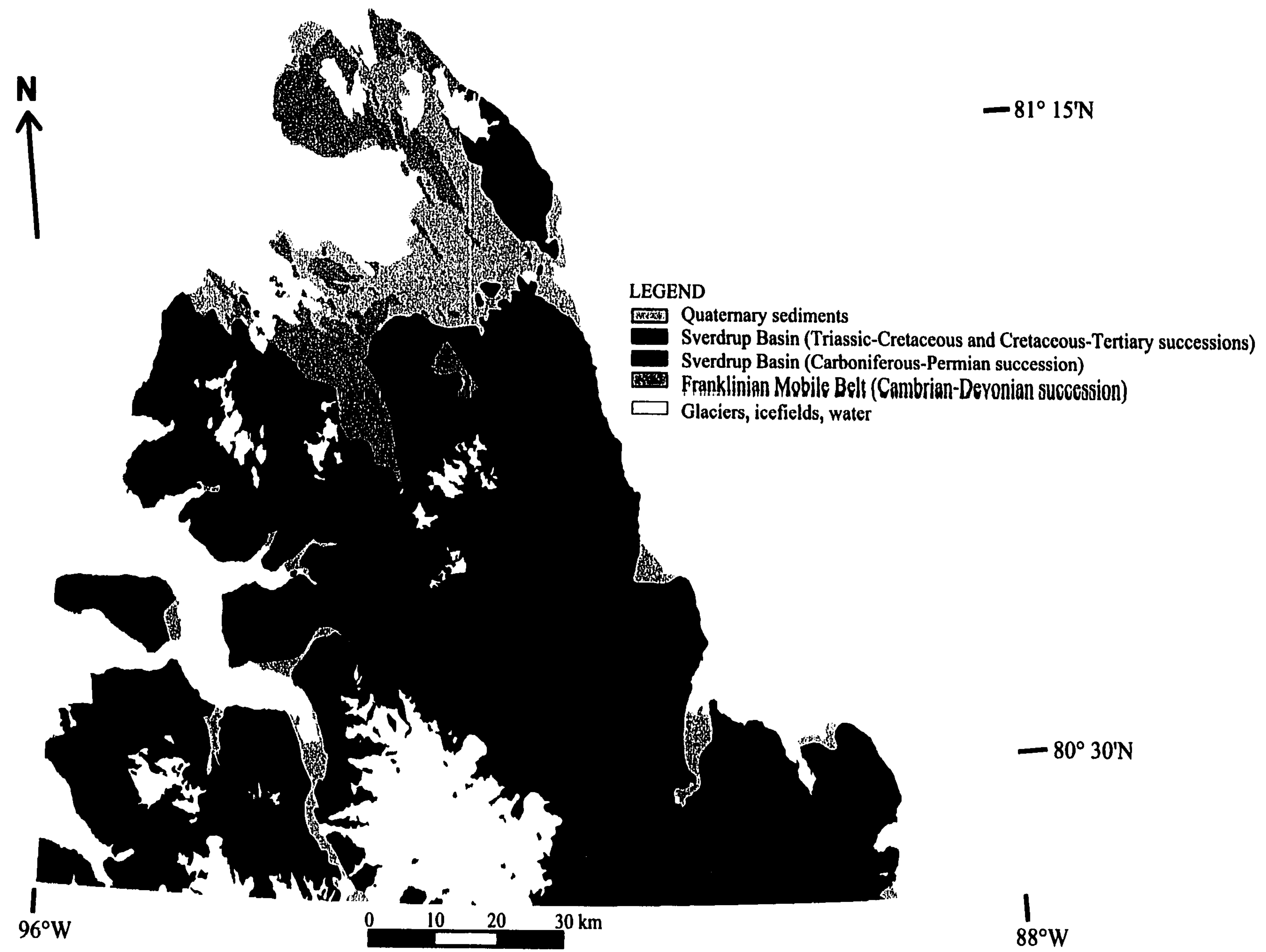
N
81° 15'N
80° 30'N
96°W
88°W
0 10 20 30 km
LEGEND
Quaternary sediments
Sverdrup Basin (Triassic-Cretaceous and Cretaceous-Tertiary successions)
Sverdrup Basin (Carboniferous-Permian succession)
Franklinian Mobile Belt (Cambrian-Devonian succession)
Glaciers, icefields, water

Heiberg Fold Belts (Trettin, 1989), the latter being well exposed in the study area. The Franklinian Mobile Belt was affected by various orogenic events during the Late Silurian to Early Carboniferous (Trettin, 1989). The latest deformation affecting the belt was associated with the Late Devonian-Early Carboniferous Ellesmerian Orogeny. Upper Cretaceous(?) mafic dykes oriented N-S intruded the Northern Heiberg Fold Belt (Trettin, 1998; see below).

Sverdrup Basin

This basin of 1300 km by 400 km developed from the Late Early Carboniferous to the Paleogene. The Sverdrup Basin, lying in angular unconformity on the Franklinian Mobile Belt (Trettin, 1998), is composed of three successions: the Carboniferous-Permian (up to 3km thick), the Triassic-Cretaceous (up to 9km thick) and latest Cretaceous-Tertiary (more than 3 km thick) (Trettin, 1991). The Carboniferous-Permian succession is mainly composed of map units ranging from shallow water carbonates and clastics to slope and basinal cherts, shales and evaporites organised into seven transgressive-regressive sequences (Beauchamp *et al.*, 1989a and b). The Triassic-Cretaceous and latest Cretaceous-Tertiary successions are dominated by marine clastic sediments (Trettin, 1991). The Triassic-Cretaceous succession is divided into 30 transgressive-regressive sequences where sandstone strata are abundant at basin margins and shale-silstone strata prevail at the basin center (Embry, 1991).

The Sverdrup Basin deposition history was influenced by tectonic events. First, a thermal uplift occurred in the Early Carboniferous where some basalt flows took place as a consequence of this high thermal activity. After, from Early Carboniferous to Early Permian, the main rifting period started where faults were active and important deformations took place. Following, in the Early Permian, a strike-slip faulting event named the Melvillian Disturbance affected the region (Beauchamp et al., 1989a and b). From Early Permian to earliest Cretaceous, a period of thermal subsidence began. The deposition of the Carboniferous-Permian succession ended by an important sea level fall in the Permian time marking the base contact with the Triassic-Cretaceous succession (Trettin, 1989). This contact between the Carboniferous-Permian and the Triassic-Cretaceous successions is generally conformable (Embry, 1991). From Middle Jurassic to Early Cretaceous a rifting period affected the western Arctic Islands, associated with the opening of the Amerasian Basin (Trettin, 1989; Embry, 1991). Following this rifting period, sea-floor spreading and thermal subsidence occurred in the Late Cretaceous (Trettin, 1989; Embry, 1991). Finally, from the Early Cretaceous to Oligocene rifting followed by sea-floor spreading occurred in the southeasthern part of the Archipelago (related with the development of the Labrador Basin). However, in the northeastern part of the Arctic Islands, sedimentation and deformation took place from the latest Cretaceous to Paleogene. The resulting succession, known as the Eureka Sound Group and present in the southeastern part of the study area, is composed of clastic sedimentary rocks derived from the erosion of the surrounding successions (Trettin, 1989).

Mafic dykes and sills related to an episode of Cretaceous volcanism intruded the Carboniferous-Permian and the Triassic-Cretaceous successions (Embry, 1991). N-S oriented mafic dykes that intruded the Triassic-Cretaceous succession are well exposed in the study area.

Tertiary And Quaternary Events and Deposition

After the Eureka Sound Group deposition, the Eurekan Orogeny affected the Arctic Islands. This intense period of deformation was active during the Paleogene (Trettin, 1989). In the northern part of Axel Heiberg, the Princess Margaret Arch and several faults were created by these orogenic movements (Trettin, 1989; Okulitch and Trettin, 1991).

The fiords and seaways present in the archipelago were formed by the development of an important Tertiary drainage system (Trettin, 1989). Drift sediments resulting from glaciations is abundant on the islands south of the Parry Channel but sparsely occurred in the Queen Elizabeth Islands. The abundant surficial deposits on the Queen Elizabeth Islands originated mainly from bedrock weathering. These weathering deposits and the drift sediments form the Quaternary sediments of the Arctic Islands (Hodgson, 1991).

RADARSAT-1 CAPABILITY

RADARSAT-1, the first Canadian remote sensing satellite, was launched in 1995. This satellite carries a Synthetic Aperture Radar sensor (right-looking) taking images in C-band frequency (5,30 GHz) with HH polarization (Parashar *et al.*, 1993). RADARSAT-1 has the capability to acquire images in 27 different beam modes differing by variation in incidence angles (10-59°), in approximate resolution (8-100m) and/or area of coverage (50km x 50km to 500km x 500km) (Luscombe *et al.*, 1993). Also, ascending (east looking direction) *versus* descending (west looking direction) orbits can be selected (Parashar *et al.*, 1993). The radar wavelength can penetrate clouds cover and dry snow (Ulaby, 1982; 1986). This active sensor can acquire images day and night (Parashar *et al.*, 1993).

DATA ACQUISITION

With the Application Development and Research Opportunity (ADRO) support, sponsored by the Canadian Space Agency, ten RADARSAT-1 images were acquired for this research (Table 1). The Standard, Extended High and Fine beam modes were selected representing: i) Various incidence angles, from 30° to 59°, ii) approximate resolutions that range from 8m to 25m, and iii) areas of coverage, less than 50km x 50km to 100km x 100km (Luscombe *et al.*, 1993). Different dates of acquisition and look directions (i.e. ascending versus descending) were also selected. Information from 1:250 000 topographic maps (NTS 560A and 560D), geological maps (Trettin 1996; Thorsteinsson and Trettin, 1972a and b; Mayr *et al.* 1998) and an ortho-photo (i.e. ortho-mosaic of 37 1:60 000 1958-1959 aerial photos from the National Air Photo Library covering an area east of Rens Fiord, resolution = 2,5m, produced by RJ Da Roza Geomatics in 1997) were also used in this research. Finally, Environment Canada meteorological data from the Eureka weather Station were obtained for the years 1996 to 1998 from the Canada Centre for Remote Sensing.

BEAM MODE	ORBIT	INCIDENCE ANGLE RANGE (°)	DATE OF ACQUISITION	RESOLUTION (range x azimuth)	PRODUCT TYPE
Fine 1	Ascending	36,8 – 39,9	1997, August 25	8,3m x 8,4m	SGX
Fine 1 Near	Descending	36,4 – 39,6	1997, August 02	8,3m x 8,4m	SGX
Fine 1 Near	Ascending	36,4 – 39,6	1998, February 16	8,3m x 8,4m	SGX
Fine 1	Descending	36,8 – 39,9	1998, February 17	8;3m x 8,4m	SGX
Fine 3 Far	Descending	41,8 – 44,3	1998, February 11	7,6m x 8,4m	SGX
Standard 3	Ascending	30 – 37	1996, May 06	25m x 27m	SGF
Standard 3	Descending	30 – 37	1998, February 13	25m x 27m	SGX
Standard 7	Descending	45 – 49	1998, February 15	19,1m x 27m	SGX
Extended High 6	Ascending	57 – 59	1998, February 13	16,4m x 27m	SGX
Extended High 6	Ascending	57 – 59	1997, August 05	16,4m x 27m	SGX

Table 1. Description of the RADARSAT-1 images acquired for this research (RADARSAT User Guide, 1998); SGX = system georeferenced x, SGF = system georeferenced full image (Denyer *et al.*, 1993).

DATA PROCESSING

The RADARSAT-1 images acquired for this study are in ground range but are not georeferenced nor corrected for distortions caused by topographic displacement. Georeferencing and orthorectification were accomplished using PCI software modules. PCI is an image analysis software for remote sensing and GIS, allowing data processing and visualization and also digital photogrammetry and radargrammetry. First, the ten images were georeferenced. Then, a DEM was generated using a radargrammetric method. Finally, ortho-images, fused images, perspectives images and strike and dip measurements were produced.

Georeferencing using the Polynomial Method

Georeferencing can be done by selecting Ground Control Points (GCPs) and using a polynomial equation best fitting these GCPs. This equation orients the image in space relative to a coordinate system without considering the relief of the terrain image and the orbital informations (Toutin, 1995). This method was chosen because the resulting georeferenced images conserved distortions relative to the displacement of the relief induced by the side-looking sensor of the radar platform. This allows identification of geological features such as geological contacts, dykes, faults, and folds, and comparison with other images taken with different acquisition parameters. These are the steps followed in our study:

1. Resampling: The images were all resampled to 25m x 25m pixel spacing to reduce speckle.

2. Linear Stretching: The images were linearly stretched to increase the tonal contrast.

3. Scaling: The images were scaled from 16-bit to 8-bit to reduce the number of grey levels.

4. GCPs Selection: GCPs were selected in the X and Y directions from 1:250 000 topographic maps for two images (Fine and Standard beam mode images) subsequently used as master images in an image-to-image GCPs selection for the eight other uncorrected images.

5. Georeferencing: The 10 images were georeferenced in the Universal Transverse Mercator (UTM) coordinate system with GCPs using the polynomial method.

The resulting ten images were georeferenced using a first or a second order polynomial depending on the best fit. The Root Mean Square (RMS) errors in the X and Y directions of GCPs were less than 2 pixels for the ten images.

DEM Generation

The DEM was generated to demonstrate the versatility of RADARSAT-1 images, to obtain a more accurate DEM than those derived from 1:250 000 topographic maps available at the Centre for Topographic Information for the study area (150m and 250m in planimetry for NTS 560D and NTS 560A respectively, and 100m in altimetry; André Bérubé, Centre for Topographic Information, pers. comm.). Although the planimetric precision should theorically be ± 79m for 1:250 000 topographic maps (Bannari *et al.*, 1997), in our study area the planimetric precision is less because of the poorly precise instrument used to make these maps and because no extra triangulation points were added to increase the planimetric precision of these maps when they were scanned from the paper format (Centre for Topographic Information, pers. comm.). The DEM was also used to produce ortho-images, fused images, perspectives images and strike and dip calculations. A radargrammetric method using a RADARSAT-1 stereo-pair and GCPs common to the two images was selected. This method considers the terrain relief, the orbital informations and the cartographic projection to create the DEM (Toutin, 1995; Toutin and Carbonneau, 1992). These are the steps followed in our study (Fig.4):

1. Stereo-pairs Selection: A RADARSAT-1 stereo-pair, S3 and S7 descending beam modes, was selected for DEM generation in order to minimize the radiometric disparities (small angle of stereo intersection) but to maximize also the geometric disparities (large vertical parallax ratio, defined by the elevation parallax on the elevation of the target) in our study area characterized by a rugged topography (more than 1200m) (Toutin, 1999; 1998b). RADARSAT-1 stereo-pair was acquired in the winter rather than in the summer where the soil moisture effect on the radar backscatter is reduced, limiting the radiometric disparities.

2. GCPs Collection: GCPs common to the two images of the RADARSAT-1 stereo-pairs were selected as input to the mathematical model in order to generate the DEM using a radargrammetric method. In mountainous areas, GCPs should be collected on well-defined ridges that have a low dip in the fore-slope direction to obtain more accurate location of the GCPs (Toutin *et al.*, 1998). Steep fore-slopes generate more topographic displacement, especially in images acquired with a small incidence angle causing localization errors.

The collection of GCPs can be done with monoscopic or stereoscopic plotting. The monoscopic plotting of GCPs induces errors in the mathematical model. This error is caused by an artificial parallax between the two images, most severe in the X and Z directions. The

Figure 4. This flow chart illustrating the steps for the following operations used in our study: DEM generation from a RADARSAT-1 stereo-pair, orthorectification of RADARSAT-1 images, fused images creation and perspective images generation (see text for explanation).

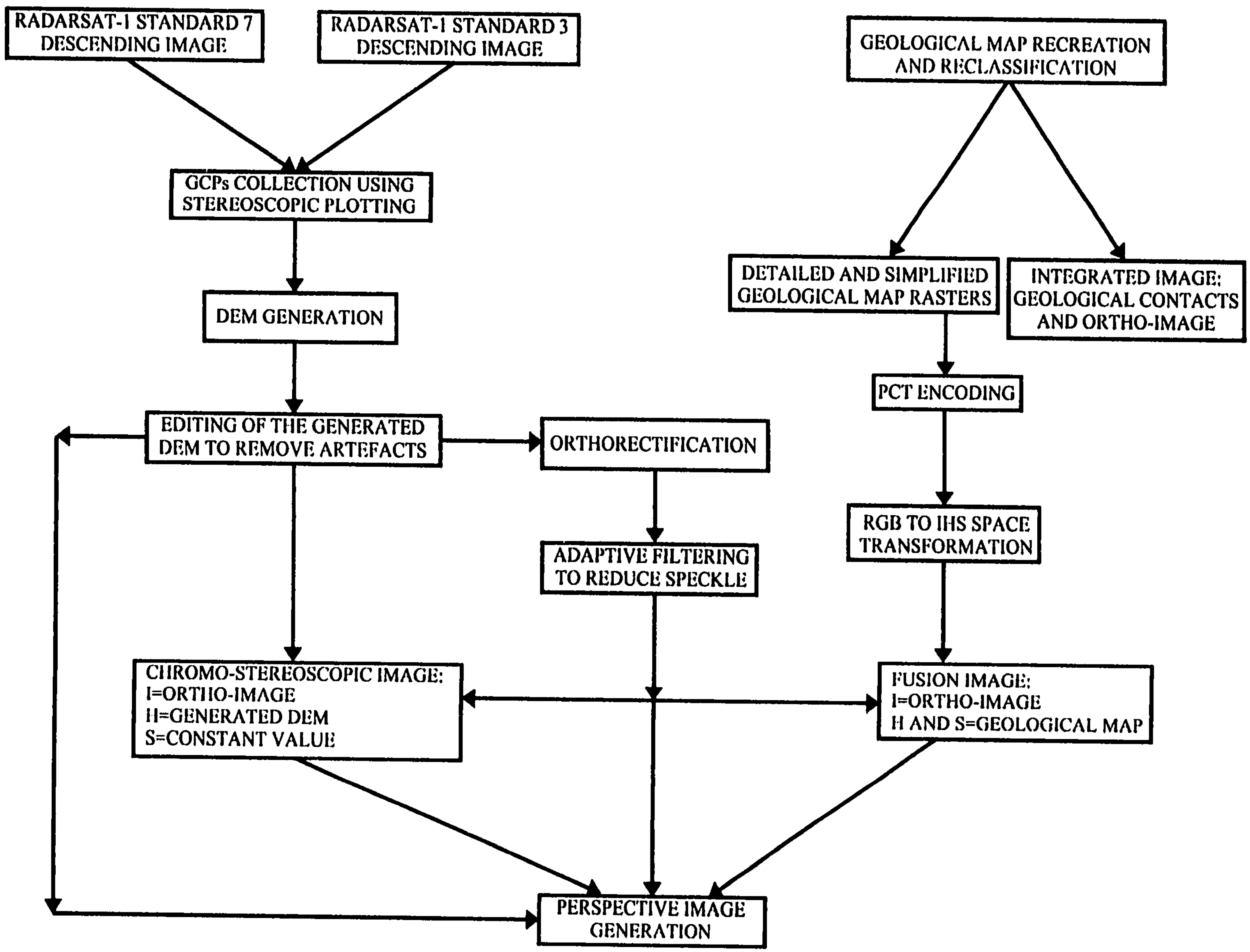
RADARSAT-1 STANDARD 7 DESCENDING IMAGE
RADARSAT-1 STANDARD 3 DESCENDING IMAGE
GEOLOGICAL MAP RECREATION AND RECLASSIFICATION
GCPs COLLECTION USING STEREOSCOPIC PLOTTING
DETAILED AND SIMPLIFIED GEOLOGICAL MAP RASTERS
INTEGRATED IMAGE: GEOLOGICAL CONTACTS AND ORTHO-IMAGE
DEM GENERATION
PCT ENCODING
EDITING OF THE GENERATED DEM TO REMOVE ARTEFACTS
ORTHORECTIFICATION
RGB TO IHS SPACE TRANSFORMATION
ADAPTIVE FILTERING TO REDUCE SPECKLE
CHROMO-STEREOSCOPIC IMAGE:
I=ORTHO-IMAGE
H=GENERATED DEM
S=CONSTANT VALUE
FUSION IMAGE:
I=ORTHO-IMAGE
H AND S=GEOLOGICAL MAP
PERSPECTIVE IMAGE GENERATION

stereoscopic plotting of GCPs is preferred because it decreases the root mean square (RMS) error of GCPs from more than 10 times the resolution (depending on the RADARSAT-1 stereo-pairs) to 1 or less times the resolution of the image (Toutin, 1998a). Consequently, the DEM accuracy is affected, increasing by a factor of 20-40% (Toutin, 1998b).

Only 10-12 GCPs are usually required for the stereo model when using 1:50 000 topographic maps (Toutin, 1998a). In the case where only 1:250 000 topographic maps are available, 20-30 GCPs should be collected, if possible, to compensate for the lower accuracy of the GCP locations. These are the steps followed in this study:

i) **GCPs collection using monoscopic plotting.** The GCPs were plotted with OrthoEngine Satellite edition module of PCI software.

ii) **GCPs collection using stereoscopic plotting.** The GCPs plotted in monoscopy were reselected in stereoscopy using a DVP, a digital stereo workstation.

The RMS errors of the 15 GCPs common to the two images using monoscopic plotting versus stereoscopic plotting are listed in the Table 2. These results demonstrate the advantage of stereoscopic plotting, using a digital stereo workstation, to decrease the RMS error of GCPs.

	X – RMS	Y – RMS	Z – RMS
Monoscopic Plotting	31,5m	29,5m	27,7m
Stereoscopic Plotting	21,1m	19,8m	15,0m

Table 2. RMS errors of 15 GCPs in the X, Y, and Z directions using monoscopic plotting versus stereoscopic plotting.

3. Mathematical Model Creation: Mathematical models are required to generate a DEM using a radargrammetric method. The mathematical models are a three-dimensional reconstruction of the imaged terrain (Toutin, 1995; Toutin and Carbonneau, 1992) created from GCPs and the orbital information.

4. DEM Generation: To achieve a georeferenced DEM without any artefacts, three steps have to be completed: i) DEM generation: the stereo matching between the two images was done using mathematical models, ii) DEM editing: the artifacts resulting from errors in the stereo matching were removed, iii) DEM georeferencing: the DEM was oriented relative to north in the UTM coordinate system for future analysis.

The accuracy of the DEM generated from S3-S7 stereo-pair using the radargrammetric method with stereoscopic plotting GCPs is in the order of two Standard beam mode resolutions (i.e. ~ 50m) with 90% confidence, based on the results of Toutin (1999).

Georeferencing using the Radargrammetric Method (Orthorectification)

The radargrammetric method georeferences, and removes the distortions such as layover, foreshortening and shadowing. This method is superior to the polynomial method because it considers the relief of the terrain imaged (a DEM is required), the orbital information and the cartographic projection (Toutin, 1995; Toutin and Carbonneau, 1992). The resulting georeferenced images are termed "ortho-images". The ortho-images can be fused with other data minimizing the shift and blur problems. These are the steps followed

(Fig. 4) in our study:

1. Image selection: The RADARSAT-1 Standard 7 and Fine 3 Far descending beam mode images were preferred to lower incidence angle beam mode images for the orthorectification process based on the increase of the ortho-image planimetric error with decrease of the incidence angle for a given DEM (Toutin and Rivard, 1997). Before selecting the GCPs on the Fine 3 Far beam mode image, this image was resampled (pixel spacing increases from 3,125m x 3,125m to 8m x 8m) to reduce the large amount of speckle.

2. GCPs collection: GCPs were selected to satisfy to the maximum extent as possible the condition of the higher planimetric and altimetric range.

3. Mathematical model creation: GCPs and orbital information are used to calculate the mathematical model.

4. Orthorectification: Using the geometric model and a DEM, an ortho-image is created.

5. Filtering: The resulting ortho-images were processed with adaptive filters (i.e. Enhanced Lee or Gamma Map) to reduce speckle.

The RMS errors of GCPs used as input to the mathematical model are approximately one resolution cell for both Standard 7 and Fine 3 Far uncorrected images (Table 3). The resulting Standard 7 and Fine 3 Far ortho-images are corrected for distortions and have a planimetric error in the order of 50m based only on the DEM accuracy and the incidence angle of the image being orthorectified. The planimetric error is also influenced by the accuracy of the GCPs which significantly increase the planimetric error of the generated ortho-images (Toutin and Rivard, 1997).

	X-RMS	Y-RMS	XY-RMS	NUMBER OF GCPs
STANDARD 7 IMAGE	21,0m	20,9m	29,6m	15
FIN 3 FAR IMAGE	5,45m	7,71m	9,44m	12

Table 3. RMS errors of GCPs used as input to the mathematical model.

Derived Products

Chromo-stereoscopic Image Generation

The generated DEM and the standard 7 ortho-image were fused to produce a chromo-stereoscopic image of the study area using the Intensity-Hue-Saturation (IHS) to Red-Green-Blue (RGB) transformation. The chromo-stereoscopic image enables depth perception with ChromaDepth^{tm} glasses (Toutin, 1997). Accurate geometric correction using the radargrammetric method was required to prevent shifts that can blur the chromo-stereoscopic image. These are the steps (Fig. 4) followed in that study:

1. *Stretching*: The DEM and the ortho-image were respectively stretched using an equal-area quantization and a square root function to increase the tonal contrast.

2. *Scaling*: The generated DEM and the RADARSAT-1 ortho-image were scaled from 16-bit signed and 16-bit unsigned respectively to 8-bit to facilitate the manipulations in the IHS space.

3. *Dynamic Range* Compression: A compression of the ortho-image dynamic range (Digital Number (DN) = 0-200) and the DEM dynamic range (DN = 0-200) were applied, allowing a good depth perception and feature identification (Toutin, 1997).

4. *IHS to RGB* transformation: The ortho-image was assigned to the intensity (I), the DEM to the hue (H) and a constant value (125) for the saturation (S). The resulting Red-Green-Blue

(RGB) image is a chromo-stereoscopic image (Toutin, 1997).

Locally, the colour saturation of the chromo-stereoscopic image was not adequate to enable a good visualization. Another chromo-stereoscopic image was produced where the DEM and the ortho-image were stretched using a linear function, scaled, and their dynamic range respectively compressed (DN = 0-180, DN = 0-200).

RADAR and Geological Map Fused Image Generation

A digital copy of the geological map of the Sverdrup Basin successions present on the northern part of Axel Heiberg Island (Mayr *et al.*, 1998) was obtain in E00 format (Data Interchange File). These files were processed in the Geographic Information System (GIS) program SPANS 6.0. The geological contact (vectors) and lithological units (polygons) of the geological map were integrated with the Standard 7 ortho-image. These are the steps (Fig. 4) followed in that study:

1. Stretching: The ortho-image was stretched using a square root function to increase the tonal contrast.

2. Scaling: The ortho-image was scaled from 16-bit unsigned to 8-bit to facilitate the manipulations in the IHS space.

3. Dynamic Range Compression: A compression of the ortho-image dynamic range (DN = 0-200) was applied.

4. Recreation and Reclassification of the Geological Map: The E00 files were imported in SPANS 6.0 and the geological map was recreated. This detailed geological map containing the formations of the Sverdrup Basin was reclassified to obtain a simplified map showing the major successions (Fig. 3) present in the northern part of Axel Heiberg. The geological contacts vector files of both the detailed and simplified geological map were exported in PCI and superposed on the ortho-image. The geological maps were transformed to a raster format and exported in PCI.

5. Pseudocolour Encoding: The geological raster maps were encoded with the legend colours (using a pseudocolour table) producing 3 RGB 8-bit channels (Harris *et al.*, 1990; 1994)

6. RGB to IHS Space Transformation: The 3 RGB 8-bit channels of the geological map were transformed to 3 IHS channels (Harris *et al.*, 1990; 1994).

7. IHS to RGB Space Transformation: The ortho-image replaced the intensity channel. For the fusion with the simplified geological map, the saturation was lowered by assigning a value of DN = 60 to the value of DN = 255 in the saturation channel. The saturation remains unchanged in the fusion using the detailed geological map. The new intensity, the unchanged hue and the new or unchanged saturation channels were retransformed in the RGB space resulting in a RGB fused image (Harris *et al.*, 1990; 1994).

Perspective Sub-images Generation

Perspective sub-images were generated from fused images and ortho-images using the generated DEM (Fig. 4) for sub-regions using various parameters (i.e. elevation exaggeration, viewing position (X,Y,Z), field of view angle, number of front pixels and view angles: direction and inclination).

Strike and Dip Calculation

Using the Fine 3 Far and the Standard 7 ortho-images, strike and dip calculations were completed for several strata in the study area using a three points method (Haneberg, 1990). The DIP program in PCI (v.6.3) calculates the strike and dip with three points selected on the same strata that have X, Y and Z components.

DISCUSSION AND INTERPRETATION

The interpretation section will be subdivided into three parts. First, the parameters influencing the radar backscatter and consequently the amount of geological information that can be extracted from radar images will be described. After the discussion of these parameters, a lithological and structural analysis of the study area will be respectively presented.

Radar Backscatter - Influencing Parameters

This study investigates the geological mapping in an arctic environment where the climate is cold and arid. Various parameters influencing the radar backscatter specific to this environment must be evaluated by the image analyst. These parameters can be grouped into those related to the acquisition parameters and those related to the surface characteristics. The acquisition parameters include the opposite orbits, variation in incidence angles, date of acquisition, pixel spacing, resolution and area of coverage, polarization, and wavelength. In this study, neither polarization modes nor wavelengths were available; HH polarization and a wavelength of 5,6 cm (C-band frequency) being the specifications of RADARSAT-1 (Parashar *et al.*, 1993). The surface characteristics comprise the soil moisture, topography and surface roughness. Although interrelated, the acquisition parameters and the surface characteristics will be described individually with an emphasis on those ones more relevant to our lithological and structural interpretation.

Acquisition Parameters

Opposite Orbits

Each orbit or looking direction gives different detection potential in relation with the orientation of the geological structures. Structures oriented perpendicular to the look direction are more easily detected (Sabins, 1997; Lewis *et al.*, 1998). The loss of information for a given look direction is, however, enabled by the opposite one; thus ascending and descending look directions being essentially complementary.

This complementary concept of opposite orbits is well illustrated in Figure 5. This figure is composed of NW-SE striking strata of the Northern Heiberg Fold Belt and Quaternary sediments. The Northern Heiberg Fold Belt is part of the Franklinian Mobile Belt and is restricted to the northern part of Axel Heiberg Island (see Fig. 3). Early Cambrian and/or older to Lower Devonian sedimentary and volcanic rocks are present along this belt (Trettin, 1998).

When comparing the two sub-images taken with opposite look directions, formational units with their dip direction matching the look direction show a more realistic representation of their true dip, as illustrated by the two members of the Stallworthy Formation (Fig. 5a). On the other hand, the subdivision of units into distinct mappable sub-units is accentuated when the dip direction is opposite to the look direction (i.e. on the back-slopes). Subtle changes in radar tones are accentuated and individual units within a formation or a member can be more easily recognized and mapped (Fig. 5b). Figure 5c is a perspective image illustrating these NW-SE striking strata of the Northern Heiberg Fold Belt.

Figure 5. This figure illustrates the lower Paleozoic NW-SE striking formations of the Northern Heiberg Fold Belt (Trettin, 1998) overlain by Quaternary sediments. Four formations are present in the study area: the volcanic flows and tuff of the Jaeger Lake Formation, the dolostone of the Aurland Fiord Formation, the volcanogenic sandstone and mudrock of the Member B of the Svartevaeg Formation and the Member A (chert conglomerate, quartzose sandstone and siltstone) and Member B (quartzose sandstone, chert conglomerate and breccia) of the Stallworthy Formation. These formations with moderate relief display a bright tone helping their identification and delineation with respect to the unconsolidated material forming the Quaternary sediments.

The two sub-images (Figs.5a and b) are from the same region but have been acquired with opposite orbits. The northeastward dipping of the Stallworthy Formation is poorly seen in the descending sub-image (Fig.5b) in comparison to the ascending sub-image (Fig.5a). On the other hand, in the descending sub-image, the subdivision of the Member B of the Stallworthy Formation into two sub-units unmapped on the geological map (Trettin, 1996) is more clearly recognized (see text for explanation). The figure 5c is a perspective image created from the chromo-stereoscopic image (red=highest elevation, blue=lowest elevation). illustrating these NW-SE striking formations.

The August 2nd sub-image (i.e. Fig. 5b) is relatively dark in comparison to the August 25th sub-image (i.e. Fig. 5a). The higher level of soil moisture in the August 2nd sub-image induces a brighter radar backscatter signal (see Soil Moisture section). The acquisition parameters or the creation parameters are listed below the sub-images. The geological contacts are derived from Trettin (1996). For location of the sub-area see Figure 2.

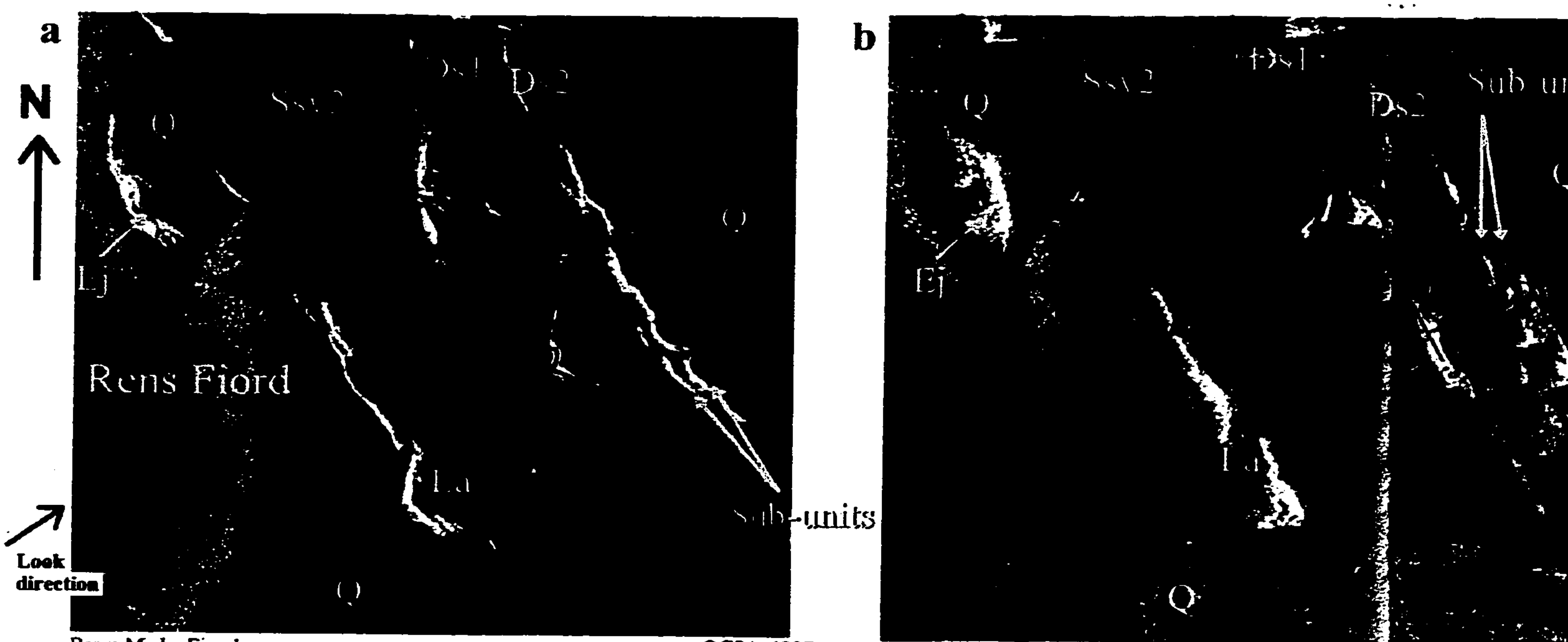

Beam Mode: Fine 1
Orbit: Ascending
Incidence Angle Range: 36,8 - 39,9°
Date: August 25, 1997
Pixel Spacing: 25m x 25m
Resolution (range x azimuth): 8,3m x 8,4m

0 2 4 6 km

Beam Mode: Fine 1 Near
Orbit: Descending
Incidence Angle Range: 36,4 - 39,6°
Date: August 2, 997
Pixel Spacing: 2. m x 25m
Resolution (range x azimuth): 8,3m x 8

LEGEND

	Quaternary	
Q	Unconsolidated sediments	
	Carboniferous	
Ce	Shale and sandstone of the Emma Fiord Formation	
	Upper Silurian(?) and Lower Devonian	
Ds2	Quartzose sandstone, chert pebble and coble conglomerate and breccia of the Member B, Stallworthy Formation	
Ds1	Chert pebble conglomerate, quartzose sandstone and siltstone of the Member A, Stallworthy Formation	
	Lower Silurian	
Ssv2	Volcanogenic sandstone, mudrock and minor conglomerate of the Svartevaeg Formation	
	Cambrian and/or older	
Ea	Dolostone of the Aurland Fiord Formation	
Ej	Volcanic flows and tuff	

- — — Fault
- Eetookashoo Bay Thrust fault
- Bedding
- Geological contact (defined, assumed)
- Look direction for the perspective image generation (Fig. 5c)

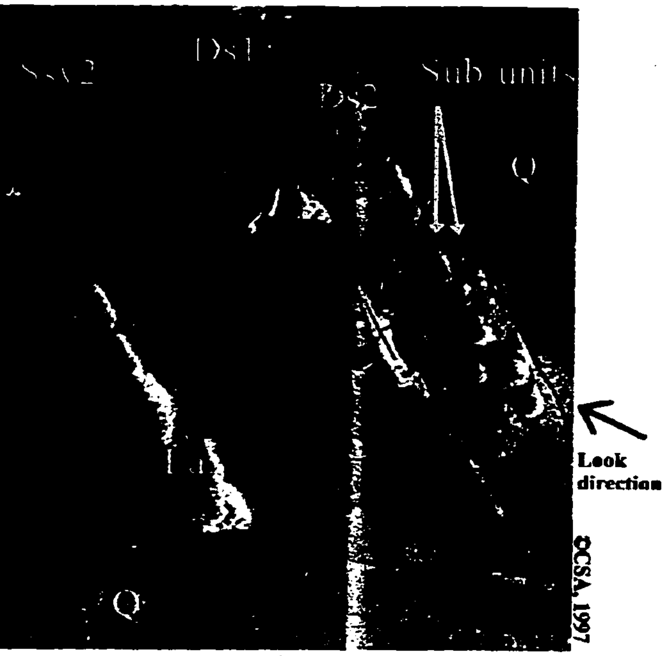

Beam Mode: Fine i Near
Orbit: Descending
Incidence Angle R ange: 36,4 - 39,6°
Date: August 2, 1[illegible]7
Pixel Spacing: 25r x 25m
Resolution (range ~ azimuth): 8,3m x 8,4m

c

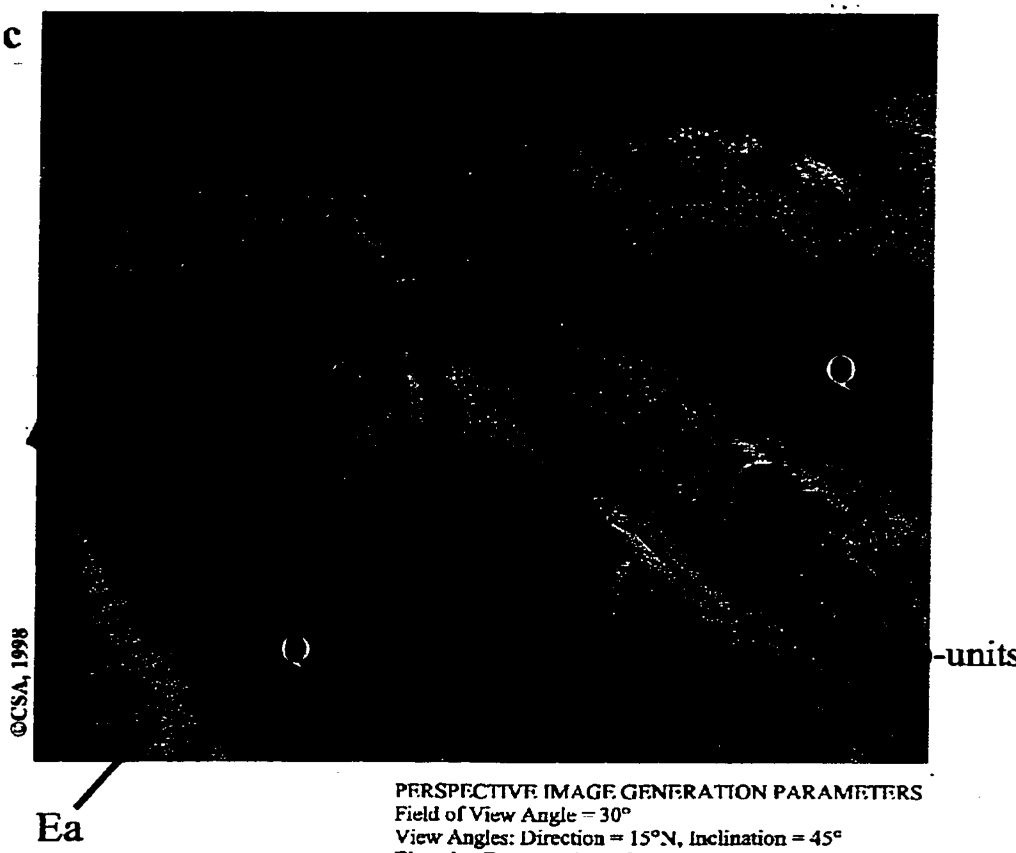

PERSPECTIVE IMAGE GENERATION PARAMETERS
Field of View Angle = 30°
View Angles: Direction = 15°N, Inclination = 45°
Elevation Exaggeration = 2
Viewing Height =2000m (above sea level)
Front Pixels = 200

r B, Stallworthy Formation
worthy Formation

ion

The complementary concept of opposite orbit images was demonstrated by layering identification (D'Iorio *et al.*, 1997). Layering is better seen in the back-slopes compared to the fore-slopes where topographic displacement occurs giving a brighter characteristic tone masking the stratal layering.

Opposite orbit images are important in a geological study to ensure a complementary interpretation of geological structures. Good representation of structural attitudes and sub-units is then available. The accessibility of RADARSAT-1 images coupled with the capability of acquiring images day or night and independent of weather conditions makes opposite orbit images available for geological investigation, especially helpful in the remote Canadian High Arctic environment, with costly field access.

Variation in Incidence Angles

The amount of topographic displacement in the radar images is inversely proportional to the incidence angle (Raney, 1998). The displacement is also accentuated in regions where high relief slopes are locally facing the look direction. In high relief regions, it is thus suitable to choose higher incidence angles to decrease the topographic displacement that can mask geological features. On the other hand, radar images with high incidence angles will display more shadowing of the poorly illuminated back-slopes (Raney, 1998). For geological investigations shadow is, however, helpful by accentuating the visibility of geological features on the images. In low relief regions, lower incidence angles can contribute to identifying geological structures because subtle relief changes are accentuated by the displacement, contributing to the identification.

Figure 6 shows formations of the Carboniferous-Permian succession of the Sverdrup Basin (Mayr *et al.*, 1998). These formations, dominated by limestone and chert form high relief slopes due to physical weathering processes largely the result of cryogenic fragmentation (Hodgson, 1991; Plaut *et al.*, 1999). Severe topographic displacement is visible in Figure 6a acquired with an incidence angle of 30-37°. The amount of topographic displacement can be reduced by using a high incidence angle image (45-49°) as shown in Figure 6b where a selected back-slope area appears shorter. The displacement can be further reduced by the use of an orthorectified version of the same image. This is illustrated in Figure 6c where the original position of the back-slope is restored. The shadow produced with higher incidence angle is helpful to delineate geological structures as exemplified in Figure 7a. This figure shows a portion of a major thrust fault sharply defined by the presence of shadow when compared to Figure 7b, acquired with a lower incidence angle (30-37°).

For mountainous terrains (slopes >40°) higher incidence angles (40-59°) are preferred to reduce the topographic displacement limiting the interpretation (Singhroy and St-Jean, 1998). For moderate to low relief terrains, low incidence angle are suitable. Images with relatively low incidence angles are useful to enhance low relief geological features characterized by subtle topographic displacement

It is then more suitable to choose higher incidence angles in high relief regions to decrease the topographic displacement on the images. Shadow, associated with higher incidence angle, is useful to localize and recognize more accurately geological features such

Figure 6. This figure demonstrates the effect of different incidence angles on the amount of topographic displacement. Four formations of the Carboniferous-Permian succession are present in these sub-images. The limestone of the Nansen Formation (the most common lithology in this sub-area), the chert of Trappers Cove Formation, the limestone with chert nodules of the Great Bear Cape Formation and the sandstone and shale of the Trold Fiord Formation. These formations form locally high relief slopes displaced by the side-looking sensor of RADARSAT-1. Note that the displacement is reduced first from figure 6a to 6b and second from figure 6b to 6c (see text for explanation). The ortho-image (Fig.6c) appears blurrier because an Enhanced Lee filter (window of 5x5) was applied during the orthorectification process to reduce speckle. The acquisition parameters are listed below the sub-images. For location of the sub-area see Figure 2.

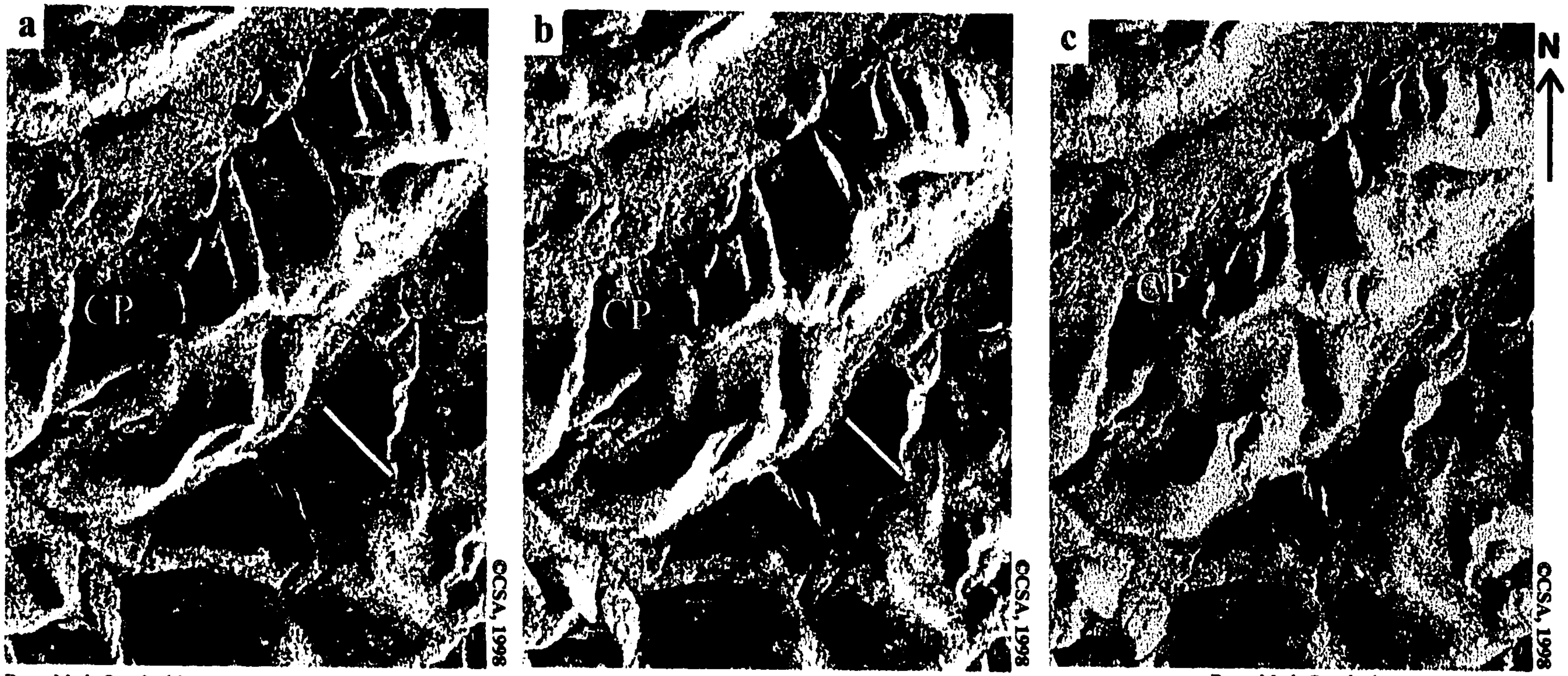

a
Beam Mode:Standard 3
Orbit: Descending
Incidence Angle Range: 30-37°
Date: February 13, 1998
Pixel Spacing: 25m x 25m
Resolution (range x azimuth): 25m x 27m

Look direction

b
Beam Mode:Standard 7
Orbit: Descending
Incidence Angle Range: 45-49°
Date: February 15, 1998
Pixel Spacing: 25m x 25m
Resolution (range x azimuth): 19,1m x 27m

Look direction

c
Beam Mode:Standard 7
Orbit: Descending
Incidence Angle Range: 45-49°
Date: February 15, 1998
Pixel Spacing: 16m x 16m
Resolution (range x azimuth): 19,1m x 27m

LEGEND
CP: Permian
- Trold Fiord Formation: sandstone, shale and calcareous sandstone
- Great Bear Cape Formation: medium bedded limestone with chert nodules
- Trappers Cove Formation: thin to medium bedded chert and limestone flasers

Carboniferous-Permian
- Nansen Formation: thick bedded to massive limestone

Topographic displacement
Corrected back-slope

0 2 4 6 km

Figure 7. This figure illustrates the benefit of shadow for delineating geological structures. The thrust fault present in this figure represents thrusting of Carboniferous-Permian formations over Triassic-Cretaceous formations. This thrust is more easily traced on the Extended High 6 sub-image (Fig.7a) than on the Standard 3 sub-image (Fig.7b) because of the more accentuated shadowing effect caused by higher incidence angle image. This thrust separates lithologies with distinct radar tones. The distinctive but variable bright and dark tones of the Carboniferous-Permian succession contrast with the more uniform darker tone of the Triassic-Cretaceous succession. The acquisition parameters are listed below the sub-images. The geological contacts are derived from Mayr *et al.* (1998). The sub-images are duplicated both with an annotated version below the interpreted version. For location of the sub-area see Figure 2.

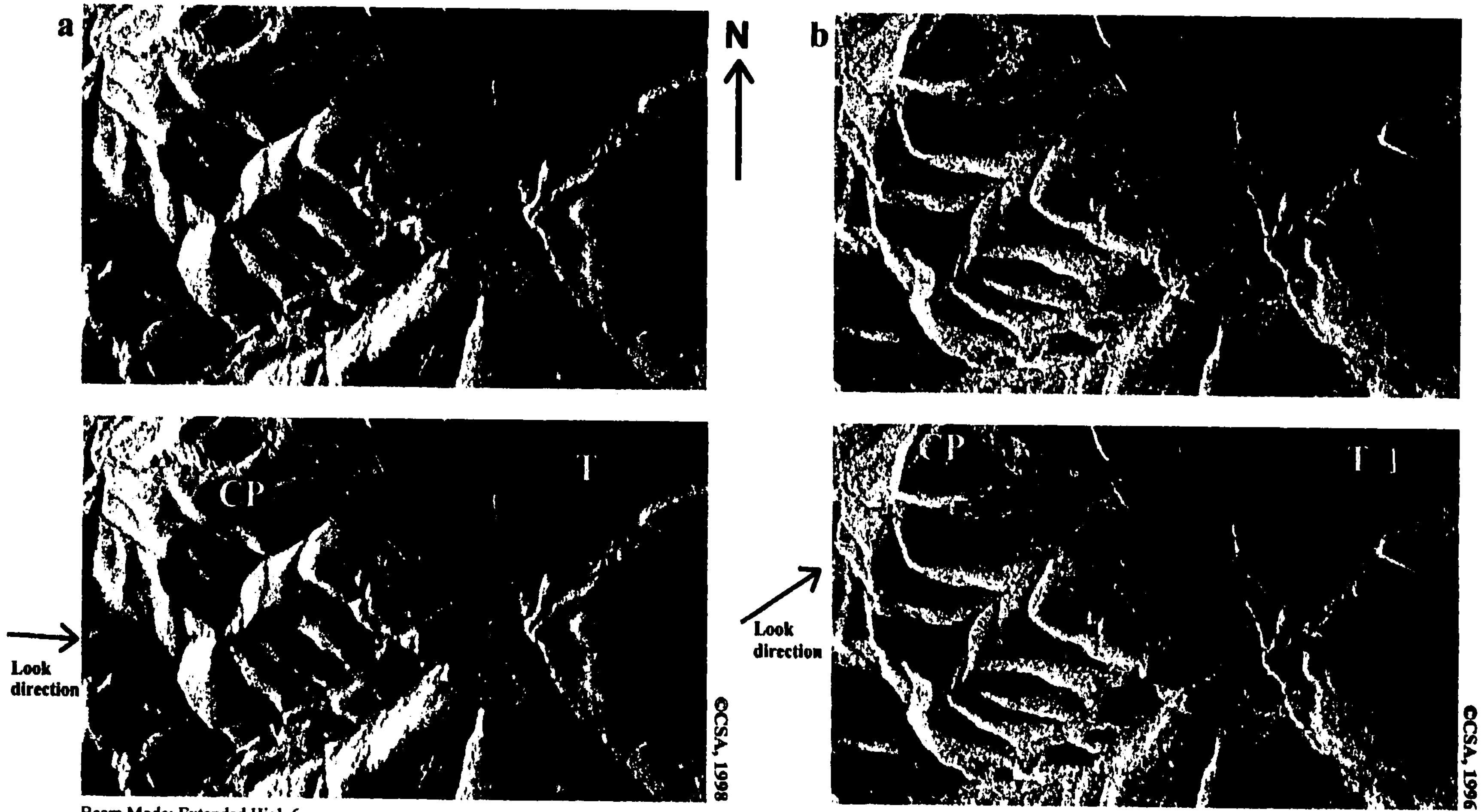

0 1 2 3 km

Beam Mode: Extended High 6
Orbit: Ascending
Incidence Angle Range: 57-59°
Date: February 13, 1998
Pixel Spacing: 25m x 25m
Resolution (range x azimuth): 16,4m x 27m

Beam Mode: Standard 3
Orbit: Ascending
Incidence Angle Range: 30-37°
Date: May 6, 1996
Pixel Spacing: 25m x 25m
Resolution (range x azimuth): 25m x 27m

LEGEND

T: Triassic
- Hoyle Bay Formation: shale and calcareous siltstone
- Roche Point Formation: shale with ironstone concretions, micritic limestone and calcareous siltstone
- Murray Harbour: shale
- Blind Fiord Formation: siltstone and silty shale

CP: Permian
- Trold Fiord Formation: sandstone, shale and calcareous sanstone
- Great Bear Cape Formation: medium bedded limestone with chert nodules
- Trappers Cove Formation: thin to medium bedded chert and limestone flasers

Carboniferous-Permian
- Nansen Formation: thick bedded to massive limestone

Geological contact (thrust fault)

as thrusts, faults, folds, dykes and geological contacts. In low incidence angle images, the dipping of the strata is exaggerated and consequently appears more easily visible in comparison with an image acquired with higher incidence angle. The ability of RADARSAT-1 satellite to acquire images with a large range of incidence angles provides geologists a flexible tool for geological mapping in an environment such as the Canadian High Arctic locally characterized by rugged topography.

Date of Acquisition

The date of acquisition is a critical parameter to consider when ordering a radar image. Seasonal effects (i.e. melting of the active layer) and variations in daily weather conditions (i.e. rain and snow precipitation) affect the soil moisture and consequently the radar backscatter. Geological units if characterized by different soil moisture conditions could be potentially mapped by radar imagery. The choice of acquisition dates, being closely related to the soil moisture especially in a barren arctic environment with permafrost, will be discussed below in the Soil Moisture section.

Pixel Spacing

SGX (Path Image Plus) and SGF (Path Image) product types have been chosen in this study. SGX RADARSAT-1 images have smaller pixel spacing than SGF images. The SGX pixel spacing respects the Nyquist sampling criterion stipulating that the pixel spacing should be less than half the resolution (Raney, 1998). With a smaller pixel spacing, information loss is prevented. Depending on the computer capabilities, SGX images with their large file size can be problematic.

The Table 4 summarizes information about the Standard, Fine and Extended High beam mode resolutions and pixel spacing. The Nyquist sampling criterion must be respected for both the azimuth and range resolutions. The SGX and SGF products for Standard and Extended High beam modes respect the Nyquist sampling criterion for the azimuth resolution. The pixel spacing of all Fine beam modes conforms to the criterion except for SGF products as indicated in Table 4. For the range resolution, the Standard 3 beam mode is the only acceptable SGF product. On the other hand, all SGX products listed in Table 4 respect the pixel spacing requirement for the range resolution.

	S1	S2	S3	S4	S5	S6	S7
Range resolution (m)	24	20	25	23	22	20	19.1
Azimuth resolution (m)	27	27	27	27	27	27	27
SGF pixel spacing (range x azimuth) (m)	12.5 x 12.5	12.5 x 12.5	12.5 x 12.5	12.5 x 12.5	12.5 x 12.5	12.5 x 12.5	12.5 x 12.5
SGX pixel spacing (range x azimuth) (m)	8 x 8	8 x 8	8 x 8	8 x 8	8 x 8	8 x 8	8 x 8

	F1N, F1, F1F	F2N, F2, F2F	F3N, F3, F3F	F4N, F4, F4F	F5N, F5, F5F
Range resolution (m)	8.3	7.9	7.6	7.3	7.1
Azimuth resolution (m)	8.4	8.4	8.4	8.4	8.4
SGF pixel spacing (range x azimuth) (m)	6.25 x 6.25	6.25 x 6.25	6.25 x 6.25	6.25 x 6.25	6.25 x 6.25
SGX pixel spacing (range x azimuth) (m)	3.125 x 3.125	3.125 x 3.125	3.125 x 3.125	3.125 x 3.125	3.125 x 3.125

	EXTH1	EXTH2	EXTH3	EXTH4	EXTH5	EXTH6
Range resolution (m)	18.2	17.7	17.3	16.8	16.6	16.4
Azimuth resolution (m)	27	27	27	27	27	27
SGF pixel spacing (range x azimuth) (m)	12.5 x 12.5	12.5 x 12.5	12.5 x 12.5	12.5 x 12.5	12.5 x 12.5	12.5 x 12.5
SGX pixel spacing (range x azimuth) (m)	8 x 8	8 x 8	8 x 8	8 x 8	8 x 8	8 x 8

Table 4. Comparison of SGF versus SGX products for Standard, Fine and Extended High beam modes (RADARSAT User Guide, 1998).

The superiority of SGX format is now well established (Toutin, 1998a). The accuracy of GCPs chosen from the SGF Fine images was more than 1 resolution when compared to less than 1 resolution for SGX Fine images. When the pixel spacing respects the Nyquist criterion, we observe no reduction in the geometric accuracy nor loss in information.

SGX images were preferred in this study based on the Nyquist sampling criterion even if the file size increases by a factor of 4 (8000 pixels x 8000 lines for SGF and 16000 pixels x 16000 lines for SGX Fine beam modes).

Resolution and Area of Coverage

These two parameters are closely linked because a RADARSAT-1 image with a higher resolution covers a smaller area. Standard beam modes (see Table 5) were selected for regional reconnaissance while fine (see Table 5) beam modes were used for more detailed local investigations. Extended High beam modes (incidence angle range: 49° to 59°) were also acquired in order to have images with higher incidence angles than Fine and Standard beam modes (incidence angle up to 48° and 49° respectively). The area of coverage of Extended High beam modes (Table 5) is, however, reduced in spite of a resolution comparable or even better than those of the Standard beam modes.

	F1N to F5F	S1 to S7	EXTH1 to EXTH6
Resolution (range x azimuth)	7.1m to 8.3m x 8.4m	19.1m to 24m x 27.0m	16.4m to 18.2m x 27.0m
Area of coverage (real time)	50km x 50km (Tape recorded: 37-45km x 50km)	100km x 100km	75km x 75km

Table 5. Resolution and area of coverage of Standard, Fine and Extended High Beam mode (RADARSAT User Guide, 1998).

Figure 8 illustrates the better resolution of a Fine beam mode with respect to a Standard beam mode. The more resistant shale with ironstone concretions of the Roche Point Formation is easily traced on the Fine beam mode image (Fig. 8a) while the Standard beam mode image (Fig. 8b) does not provide enough contrast for its recognition.

Standard beam modes with their large area of coverage are useful for preliminary geological reconnaissance. In addition, generation of large area DEMs and data integration without any mosaicking is greatly facilitated. The higher resolution of Fine beam modes is, however, required for the recognition of local scale geological features. Higher incidence angle images (i.e. Extended High beam modes) are also essential in areas of with high relief (i.e. our study in the Canadian High Arctic) in order to reduce the topographic displacement even at the expense of a smaller area of coverage.

<u>Surface Characteristics</u>

Soil Moisture

The soil moisture level affects the dielectric constant of the surface cover (Ulaby, 1982; 1986). In an arctic environment with permafrost such as the study area, the state of the active layer and the nature of the bedrock affects the radar backscatter signal. The tonal differences between summer and winter images are more important in regions where an active layer is present. The warmer temperature of the summer months causes the active layer above the impermeable permafrost to be saturated with water.

The temporal soil moisture variations in the active layer can be detected on the

Figure 8. This figure demonstrates the difference in resolution for identifying geological features. The three Triassic formations present in this sub-image are part of the Triassic-Cretaceous succession of the Sverdrup Basin (Fig. 3). The more resistant shale with ironstone concretions of the Roche Point Formation contrasts with the adjacent shales of the Murray Harbour and Hoyle Bay formations. When comparing the Fine 1 Near sub-image (resolution=8,3m x 8,4m; Fig. 8a) with the Standard 3 sub-image (resolution=25m x 27m Fig. 8b), the Roche Point Formation is clearly traced in the Fine 1 Near sub-image because of the better spatial resolution. The sub-images are both duplicated with an annotated version below the interpreted version. The geological contacts are derived from Mayr *et al.* (1998). The acquisition parameters are listed below the sub-images. For location of the sub-area see Figure 2.

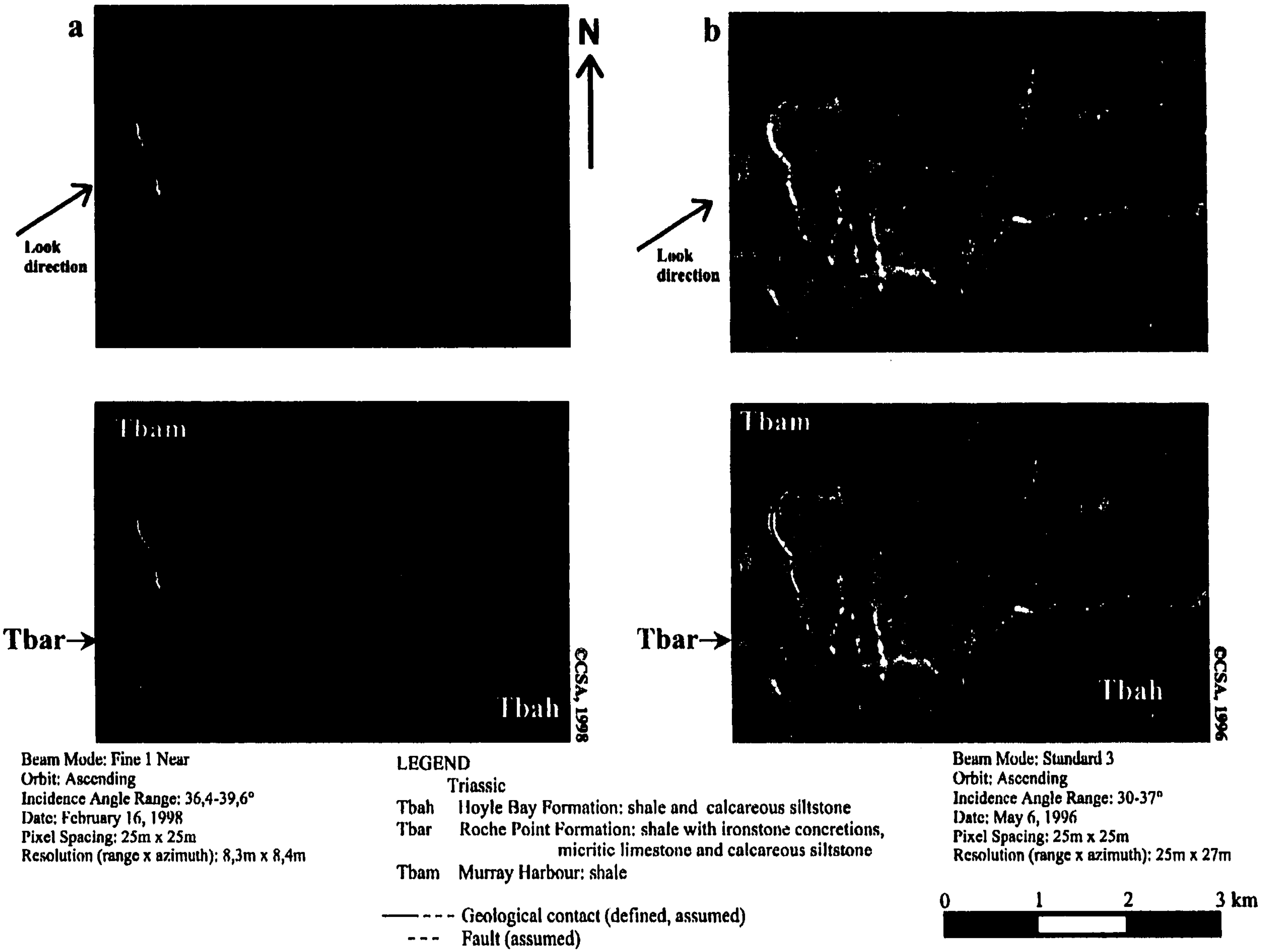
a
N
b
Look direction
Look direction
Tbam
Tbam
Tbar→
Tbar→
Tbah
Tbah
©CSA, 1998
©CSA, 1996
Beam Mode: Fine 1 Near
Orbit: Ascending
Incidence Angle Range: 36,4-39,6°
Date: February 16, 1998
Pixel Spacing: 25m x 25m
Resolution (range x azimuth): 8,3m x 8,4m
LEGEND
Triassic
Tbah Hoyle Bay Formation: shale and calcareous siltstone
Tbar Roche Point Formation: shale with ironstone concretions, micritic limestone and calcareous siltstone
Tbam Murray Harbour: shale
Geological contact (defined, assumed)
Fault (assumed)
Beam Mode: Standard 3
Orbit: Ascending
Incidence Angle Range: 30-37°
Date: May 6, 1996
Pixel Spacing: 25m x 25m
Resolution (range x azimuth): 25m x 27m
0
1
2
3 km

RADARSAT-1 images. Changes in radar tone are clearly visible in the summer/winter images (Fig. 9). As listed in the Table 6, the summer and winter images in Figure 9 were acquired respectively with a ground temperature above and below 0°C. In the winter image, the frozen state of the active layer induces a relatively dark tone whereas the summer image display a brighter tone related to the melting of the active layer (Fig. 9). The discrimination between units of the Northern Heiberg Fold Belt and the Quaternary sediments is more accentuated in the winter image (Fig. 9).

Acquisition Dates of EXTH 6 Images	5-Aug-97	13-Feb-98
Daily Maximum Temperature (°C)	7.1	-42.4
Daily Minimum Temperature (°C)	3.2	-46.8
Daily Mean Temperature (°C)	5.2	-44.6
Rain (cm)	0.4	0
Snow (cm)	0	0
Total Precipitation (rain and snow) (cm)	0.4	0
Snow on Ground (cm)	0	11

Table 6. Meteorological data at Eureka Weather Station, located 150 km south-east of the study area (see Fig. 1; data provided by CCRS).

The temporal tonal variations of the Quaternary sediments (i.e. winter *versus* summer images) are caused by seasonal changes in the state of the active layer. In the future, multi-date RADARSAT-1 images could enable monitoring the long-term evolution of the active layer. This application of RADARSAT-1 makes it an interesting tool to measure the effects of global warming, particularly at high latitudes where the effects may be more accentuated (Lewkowicz and Duguay, 1999).

The difference in contrast between radar images acquired at different seasons has been well demonstrated in other arctic environments (Budkewitsch *et al.*, 1997). When the

Figure 9. These two sub-images illustrate the soil moisture effect on the radar backscatter signal. This region is mainly composed of Quaternary sediments with some bedrock exposures of the Upper Silurian(?) and Lower Devonian Member B (quartzose sandstone, chert pebble and coble conglomerate and breccia) of the Stallworthy Formation and the Lower Cambrian Grant Land Formation (quartzite, phyllite and slate). The Quaternary sediments are highly saturated in water during the warm summer months taking a brighter tone (Fig.9b). The winter sub-image (Fig.9a) displays a darker tone because of the frozen state of the water contain in the sediments. In addition, the reduction of the dielectric constant effect on the radar backscatter signal in the winter image shows more contrast between the Lower Paleozoic Grant Land and Stallworthy formations (Member B) of the Northern Heiberg Fold Belt and the Quaternary sediments. The acquisition parameters are listed below the RADARSAT-1 images. The geological contacts are derived from Trettin (1996). For location of the sub-scene see Figure 2.

a

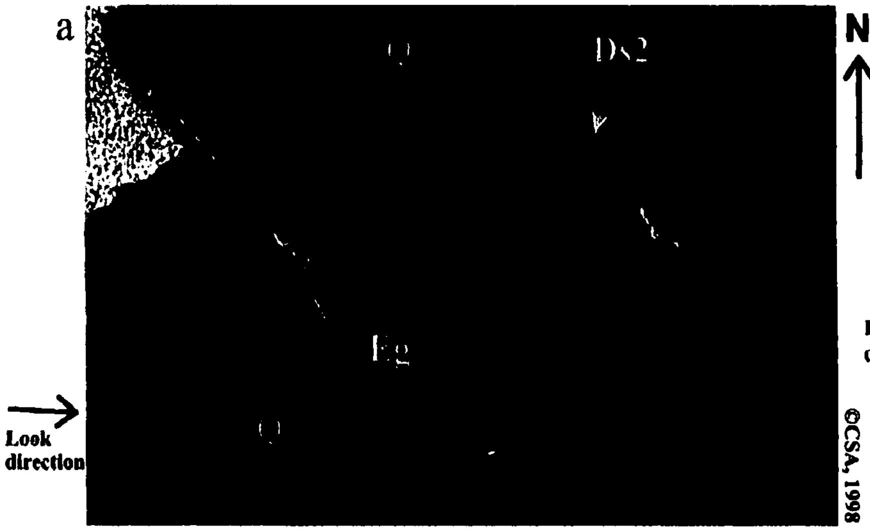

©CSA, 1998

Beam Mode: Extended High 6
Orbit: Ascending
Incidence Angle Range: 57-59°
Date: February 13, 1998
Pixel Spacing: 25m x 25m
Resolution (range x azimuth): 16,4m x 27m

b

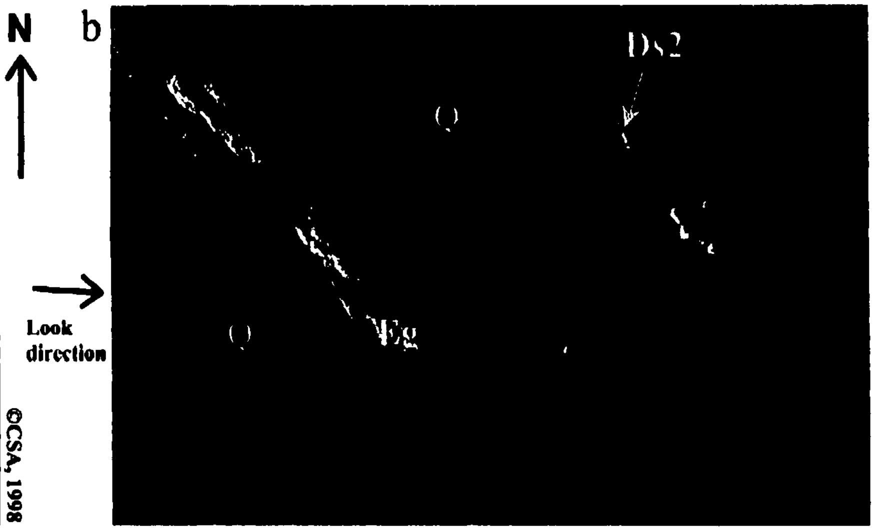

©CSA, 1997

Beam Mode: Extended High 6
Orbit: Ascending
Incidence Angle Range: 57-59°
Date: August 5, 1997
Pixel Spacing: 25m x 25m
Resolution (range x azimuth): 16,4m x 27m

LEGEND

Q Quaternary sediments

Ds2 Upper Silurian(?) and Lower Devonian quartzose sandstone, chert pebble and coble conglomerate and breccia of the Member B, Stallworthy Formation

Eg Lower Cambrian quartzite, phyllite and slate forming the Grant Land Formation

— Geological contact

0 2 4 6 km

temperature is below 0°C, the contrast is maximized between bedrock and the surrounding vegetation cover because of the reduced effect of the dielectric constant on the radar backscatter due to the absence of water (Budkewitsch *et al.*, 1997).

Topography

In high relief regions, the radar tones are largely influenced by the topography (Ford *et al.*, 1998). The topographic relief (Sabins, 1997) influences the amount of displacement in a radar image causing the fore-slopes to be brighter whereas the back-slopes appear darker (Raney, 1998). Unlike the high relief regions, the radar tones in low relief regions are mainly controlled by the surface roughness (Ford *et al.*, 1998; Budkewitsch *et al.*, 1996; see below).

Surface Roughness

The surface roughness is derived from the variations in ground height, at the resolution of the image (Sabins, 1997). These variations affect the resolution cell tone and consequently the texture of the image. In the low vegetation of the arctic environment, the surface roughness is mainly a function of the size and shape of the grains forming the surficial sediments and the surface of exposed bedrock. The surficial material is directly derived from the *in situ* breaking of the various rock types in response to physical weathering processes, especially cryogenic fragmentation (Hodgson, 1991; Plaut *et al.*, 1999).

Figure 10 illustrates the radar tone variations resulting from a difference in surface roughness between two formations of the Northern Heiberg Fold Belt; a dolostone unit and a

Figure 10. This figure shows tonal variations resulting from difference in surface roughness between two formations of the Northern Heiberg Fold Belt; the Early Cambrian and/or older dolostone of the Aurland Fiord Formation and the Lower Cambrian quartzite, phyllite and slate forming the Grant Land Formation. The thrust-faulted contact between the brighter dolostone and darker quartzite, phyllite and slate is easily traced because of the tonal differences. The acquisition parameters are listed below the sub-ortho-image. The geological contacts are derived from Trettin (1996). For location of the sub-area see Figure 2.

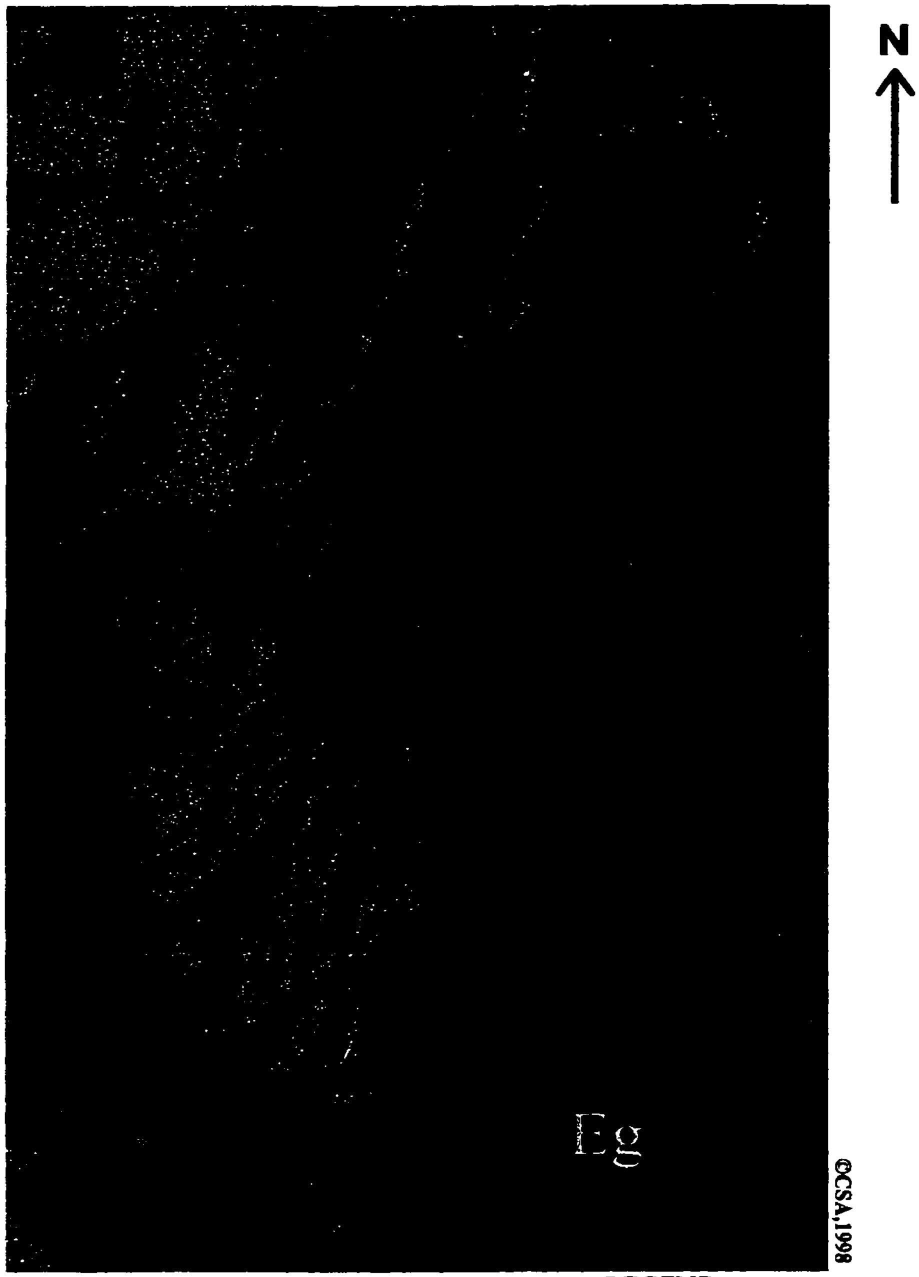

Beam Mode: Standard 7
Orbit: Descending
Incidence Angle Range:45-49°
Date: February 15, 1998
Pixel Spacing: 16m x 16m
Resolution (range x azimuth): 19,1m x 27m

LEGEND

Lower Cambrian

Eg Grant Land Formation: quartzite, phyllite and slate

Cambrian and/or older

Ea Aurland Fiord Formation: dolostone

Geological contact (Aurland Fiord Thrust)

0 1 2 3 km

quartzite, phyllite and slate unit. In this relatively low relief region, the dolostone shows a bright tone because this resistant unit breaks into large weathered fragments (Fig. 10). The quartzite, phyllite and slate are forming a more recessive unit resulting in finer weathered fragments and giving a darker tone (Fig. 10).

Changes in radar backscatter related to different lithological surface roughness have been recently studied (Budkewitsch *et al.*, 1996; Plaut *et al.*, 1999). Larger fragments resulting from the weathering of resistant lithologies (e.g. reefal carbonates and well cemented arenites) produce a brighter tone than finer fragments derived from more easily weathered units (e.g. fissile shale, poorly cemented sandstone and siltstone) which are characterized by a darker tone (Budkewitsch *et al.*, 1996).

The RADARSAT-1 potential to recognize surface roughness is an important tool for lithological discrimination, especially in low relief arid regions where the radar tones are not significantly influenced by the topography and/or the vegetation cover. Individual lithology displays commonly a distinctive breaking pattern related to their composition. The resulting fragments from a given weathered bedrock may thus develop a specific surface roughness signature and consequently a particular tone range in a radar image.

Lithological Mapping

This section will discuss the recognition of geological units in an arctic environment using radar imagery. RADARSAT-1 acquires images day or night (Parashar *et al.*, 1993) and independently of clouds cover and through dry snow (Ulaby, 1982; 1986) allowing an all year long acquisition of images. A preliminary analysis of the major geological contacts should provide a good knowledge of the study area before planning costly and complicated field seasons associated with arctic field work. Previous studies (D'Iorio *et al.*, 1997, 1995; Ford, 1998; Lewis *et al.*, 1998; Paradella *et al.*, 1998; Plaut *et al.*, 1999; Rivard *et al.*, 1994; Singhroy and St-Jean, 1998, 1997; Singhroy *et al.*, 1993; Webster *et al.*, 1997a and b; Desrochers *et al.* 1997) have demonstrated the potential of radar imagery for geological mapping but only a few studies were located in the arctic environment (Budkewitsch *et al.*, 1996 and 1997; Plaut *et al.*, 1999). This section will be subdivided in three parts: macro, meso and micro scale mapping corresponding to mapping geological features at the scale of geological provinces, formation units and sub-unit contacts respectively.

Macro Scale Mapping (>1:250 000)

The basal and intra Sverdrup Basin contacts and the contact below significant Quaternary sediments (Fig. 3) present in the study area, are well recognized on the RADARSAT-1 images (Fig. 11a and b). The identification is based on large-scale tone variations associated with changes in the surface parameters. These parameters are mainly dominated by the effects of the topographic relief especially in winter when the soil moisture effects are more subdued. Figure 12 shows examples of the radar tone associated with the major successions present in the study area (see also compiled information in Table 7).

Geological Province	Franklinian Mobile Belt	Sverdrup Basin (Carboniferous-Permian succession)	Sverdrup Basin (Triassic-Cretaceous succession)	Quaternary sediments
Radar Tone	Light grey	White and black	Grey	Dark grey
Local Relief	Moderate	High	Relatively flat to moderately high	Flat

Table 7. The general tone frequently present in the major successions exposed in the study area based on a winter Standard 7 beam mode image (Fig. 12).

Figure 11. The figures 11a and 11b are integrated images of the study area showing the high correlation of the Quaternary sediments, the Northern Heiberg Fold Belt succession and the Sverdrup Basin successions contacts with the tone of the Standard 7 beam mode ortho-image. The Figure 11a results form the fusion of a simplified geological map (derived from the geological map of Mayr *et al.*, 1998; see Fig.3) with the ortho-image. The Figure 11b was produced by the overlay of the geological contacts in a vector format (derived from the geological map of Mayr *et al.*, 1998) onto the ortho-image. The acquisition parameters are listed beside the images.

Figure 11a

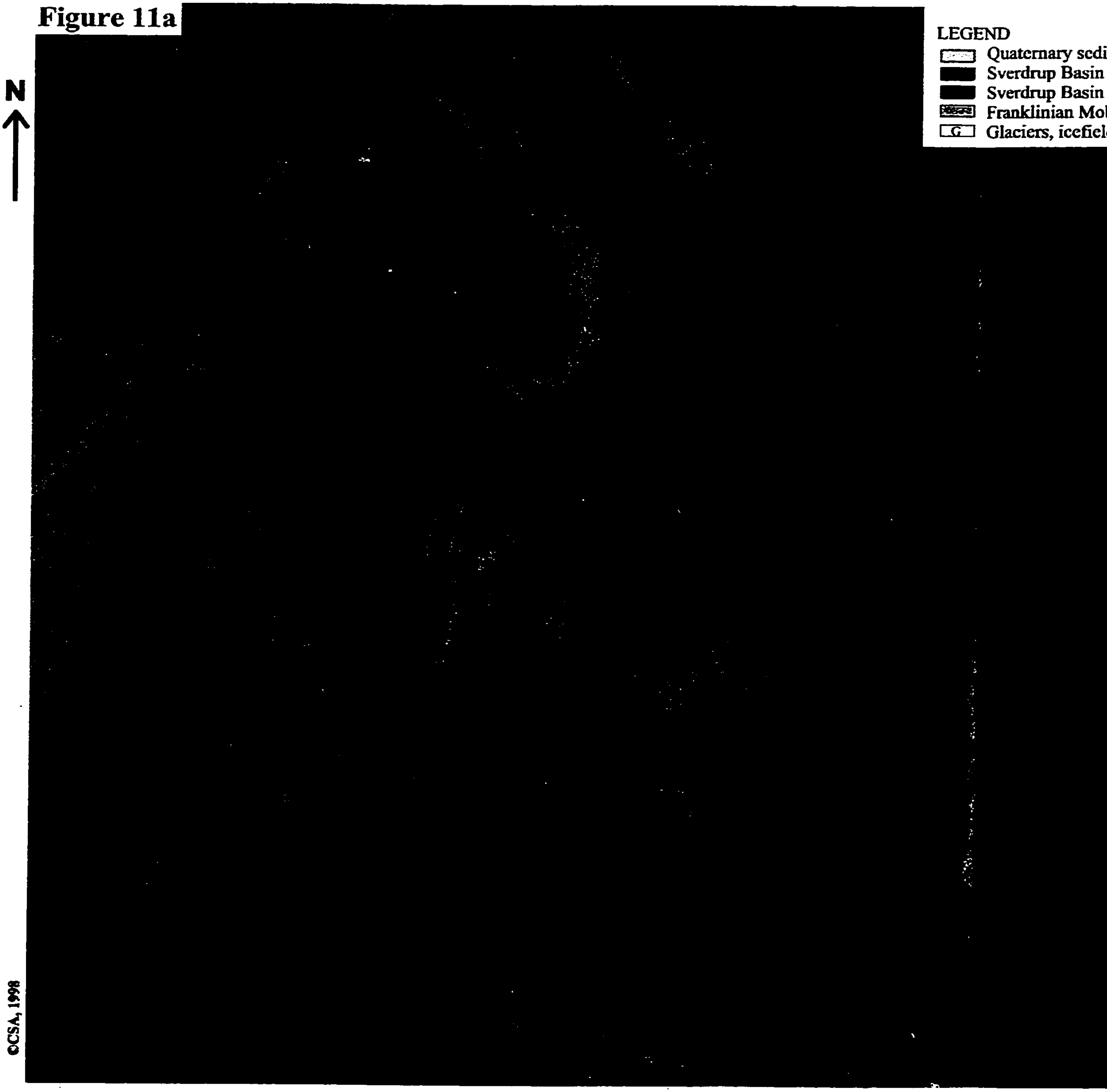

LEGEND
Quaternary sedi
Sverdrup Basin
Sverdrup Basin
Franklinian Mol
G
Glaciers, icefiel
N
©CSA, 1998

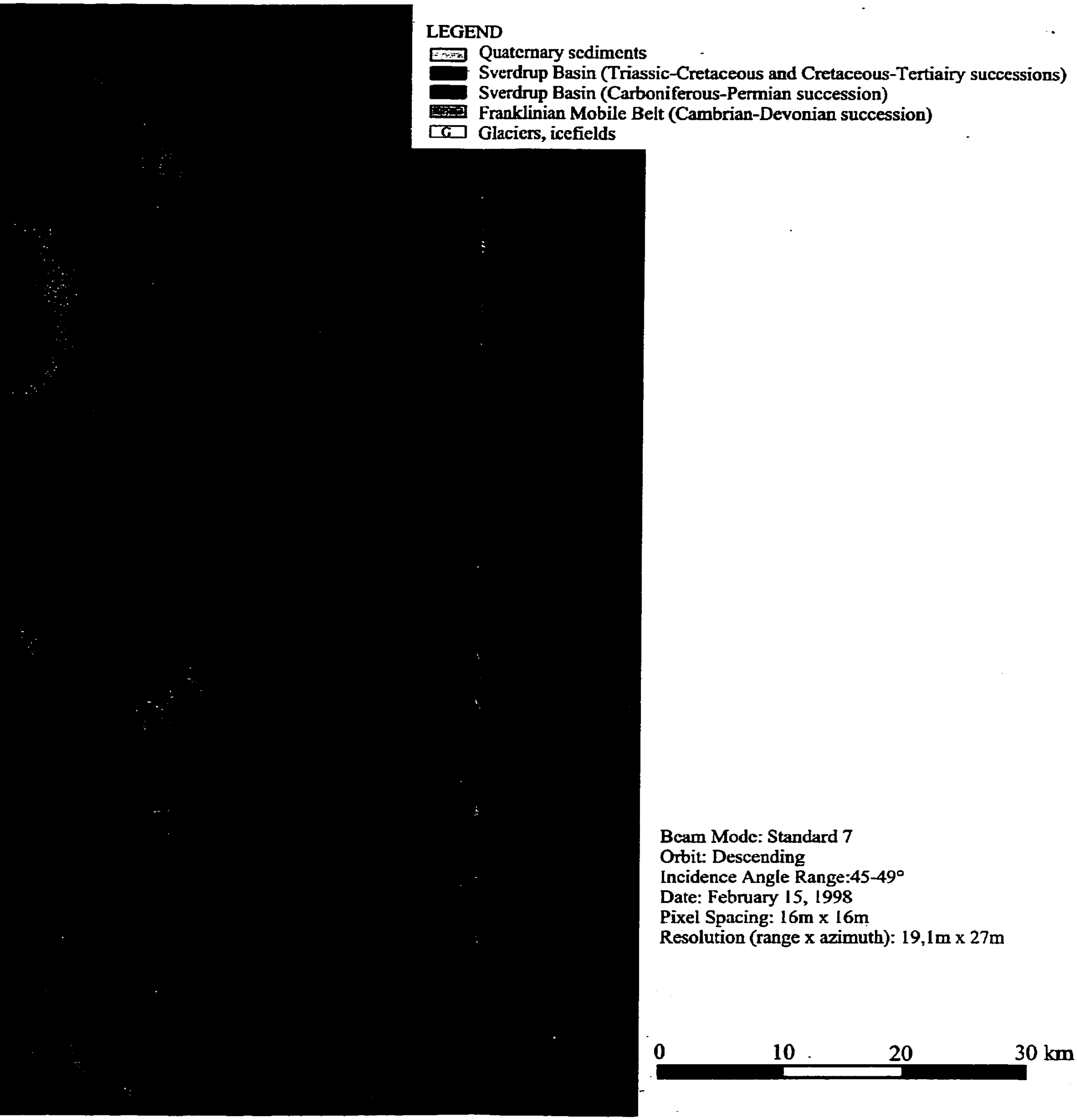
LEGEND
Quaternary sediments
Sverdrup Basin (Triassic-Cretaceous and Cretaceous-Tertiairy successions)
Sverdrup Basin (Carboniferous-Permian succession)
Franklinian Mobile Belt (Cambrian-Devonian succession)
G Glaciers, icefields
Beam Mode: Standard 7
Orbit: Descending
Incidence Angle Range:45-49°
Date: February 15, 1998
Pixel Spacing: 16m x 16m
Resolution (range x azimuth): 19,1m x 27m
0
10
20
30 km

N

Figure 11b

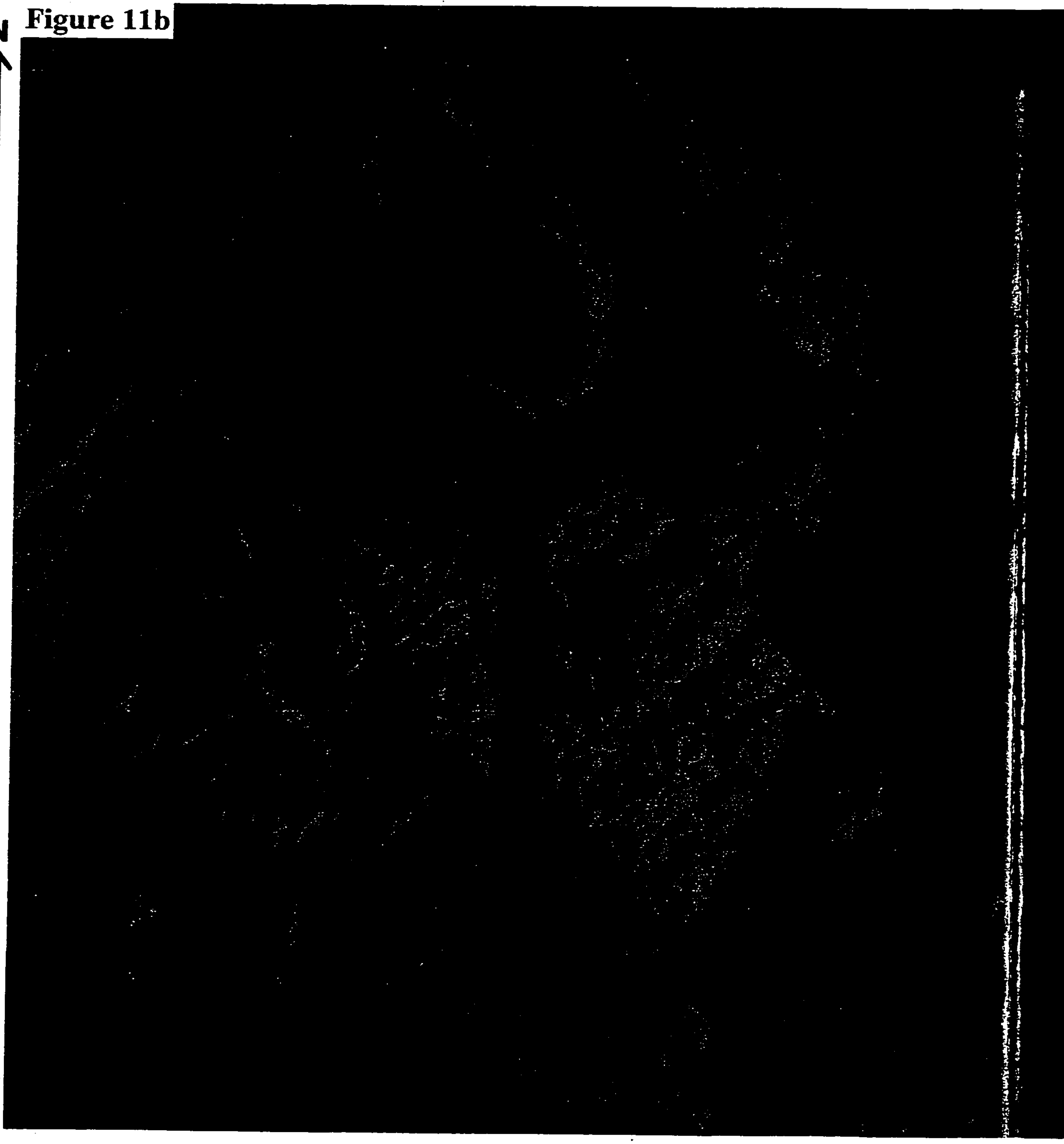

LEGEND

— Geological contacts between the major successions present in the study area (see Fig. 11a)

Beam Mode: Standard 7
Orbit: Descending
Incidence Angle Range:45-49°
Date: February 15, 1998
Pixel Spacing: 16m x 16m
Resolution (range x azimuth): 19,1m x 27m

0 10 20 30 km

Figure 12. This figure is composed of four sub-images derived from a Standard 7 beam mode image. These sub-images are examples of the radar signatures commonly associated with the major successions present in the study area: a) Quaternary sediments, b) Triassic-Cretaceous succession of the Sverdrup Basin, c) Carboniferous-Permian succession of the Sverdrup Basin, d) Cambrian-Devonian succession of the Franklinian Mobile Belt. The acquisition parameters are listed below the Standard 7 beam mode image.

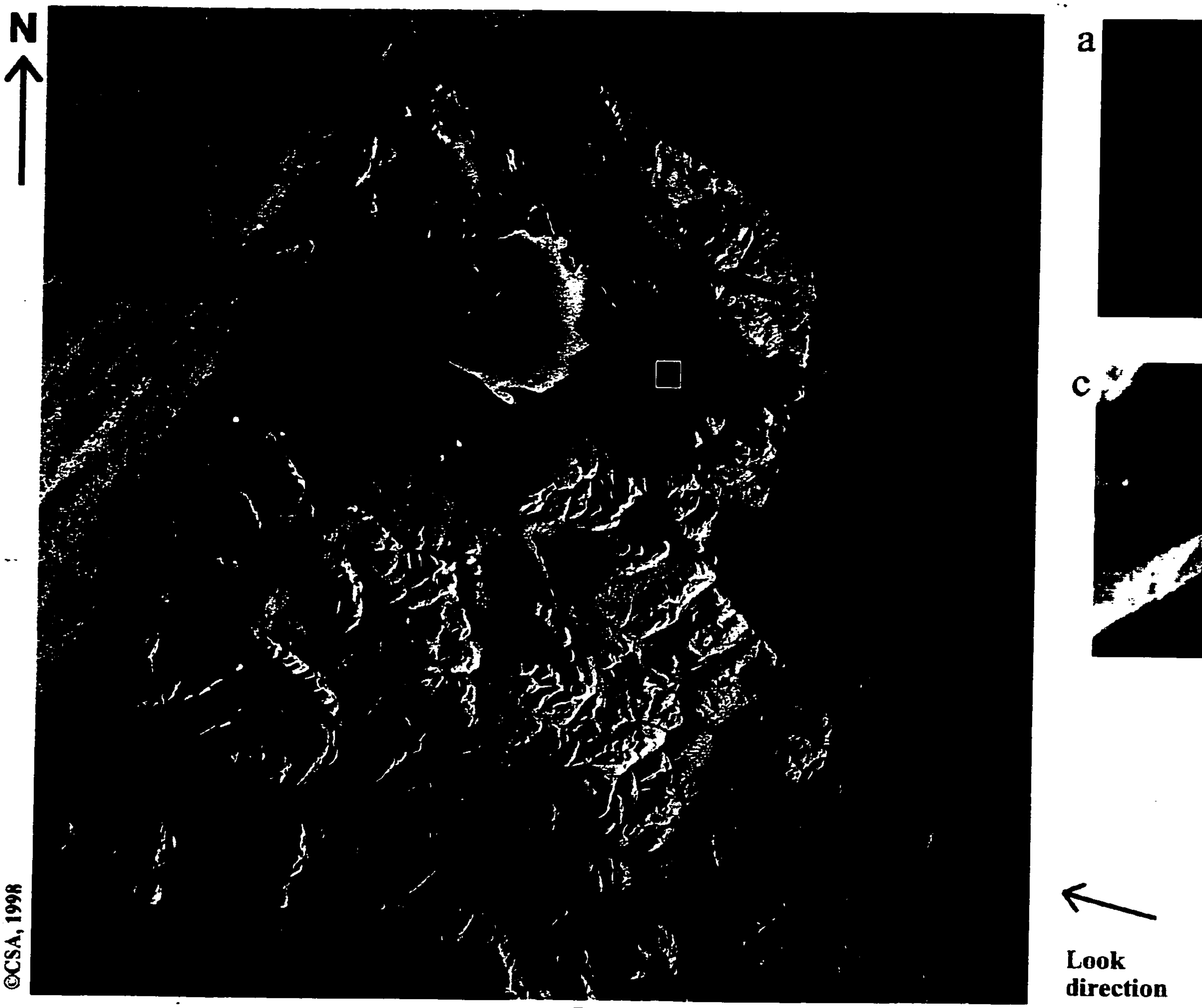

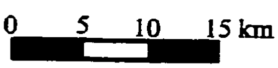

Beam Mode: Standard 7
Orbit: Descending
Incidence Angle Range: 45-49°
Date: February 16, 1998
Pixel Spacing: 25m x 25m
Resolution (range x azimuth): 19,1m x 27m

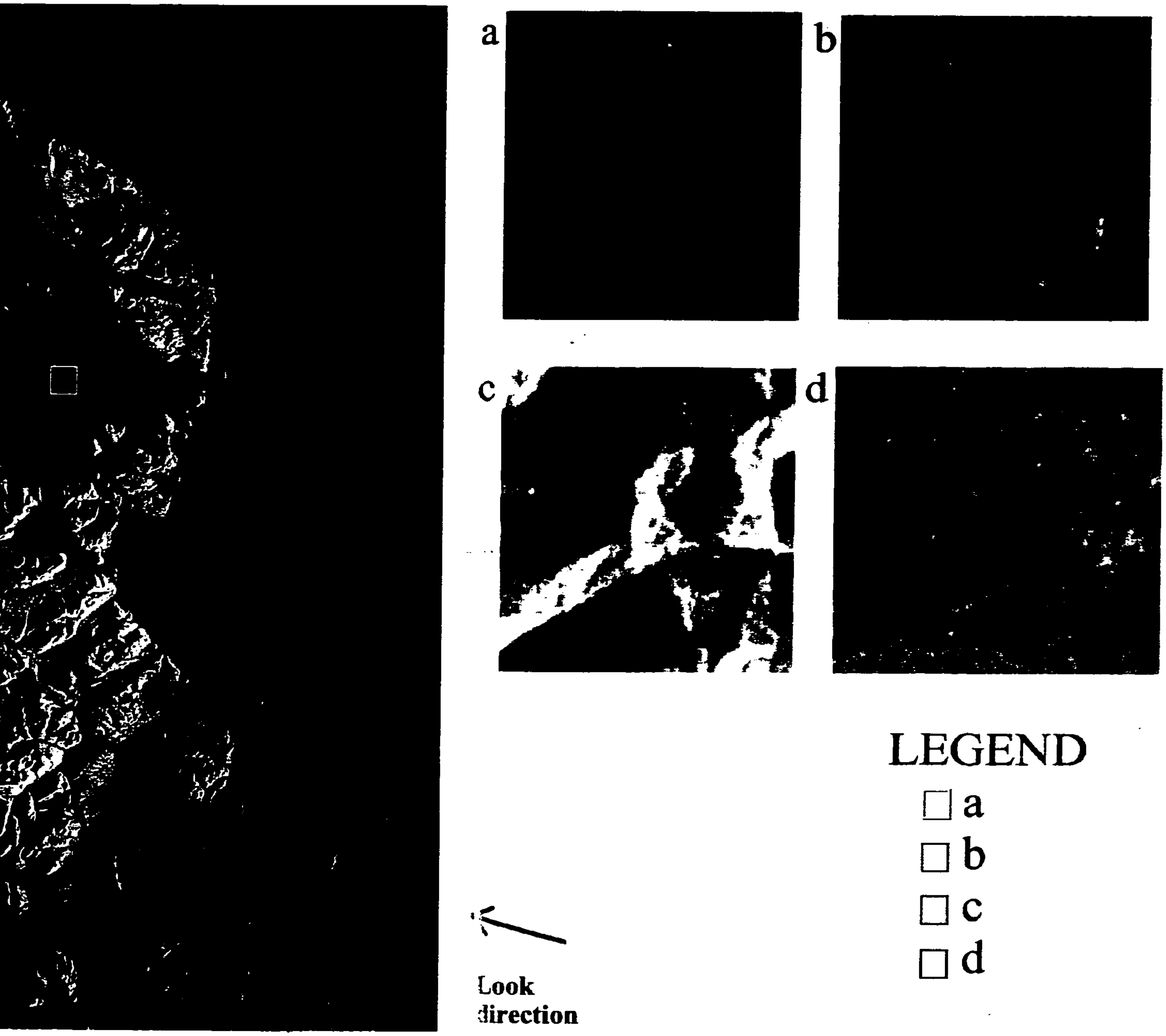

ım Mode: Standard 7
›it: Descending
idence Angle Range: 45-49°
c: February 16, 1998
el Spacing: 25m x 25m
solution (range x azimuth): 19,1m x 27m

Basal Sverdrup Basin Contact

A significant unconformable contact present in the study area separates the lower Paleozoic succession of the Franklinian Mobile Belt from the Carboniferous-Permian succession of the Sverdrup Basin (Fig. 3). This locally faulted contact is an angular unconformity that developed consequently to the Ellesmerian Orogeny (Trettin, 1998).

The succession of the Franklinian Mobile Belt present in the northern part of Axel Heiberg Island formed the Northern Heiberg Fold Belt. This belt is composed of Lower Cambrian to Lower Devonian sedimentary and volcanic rocks divided into six formations: Jaeger Lake, Aurland Fiord, Grant Land, Hazen, Svartevaeg and Stallworthy formations (Trettin, 1996; 1998).

The sedimentary and volcanic rocks forming the Carboniferous-Permian succession of the Sverdrup Basin present in the study area are subdivided into several formations: Emma Fiord, Borup Fiord, Otto Fiord, Hvitland Peninsula, Hare Fiord, Nansen, Raanes, Trappers Cove, Great Bear Cape, Esayoo, Sabine Bay and Assistance (undivided), Trold Fiord, Van Hauen, Lindström, and also unnamed volcanics formations (Mayr *et al.*, 1998; Fig. 13).

This contact is well identified on the RADARSAT-1 images including the orthorectified Standard 7 image (Fig.11b). At that scale, the general tone of the image is mainly controlled by the topographic relief (Sabins, 1997). The Cambrian to Devonian rocks of the Northern Heiberg Fold Belt form locally low relief slopes in opposite to the higher relief slopes of the Carboniferous-Permian succession of the Sverdrup Basin. Physical

Figure 13. This figure is the detailed geological map of the formation units of the Sverdrup Basin present in the northern part of Axel Heiberg Island. This map was created in SPANS 6.0 using a digital copy of the map. The legend and the digital copy of the geological map were provided by Mayr et al. (1998).


N
96°W
0 10 20 30 km

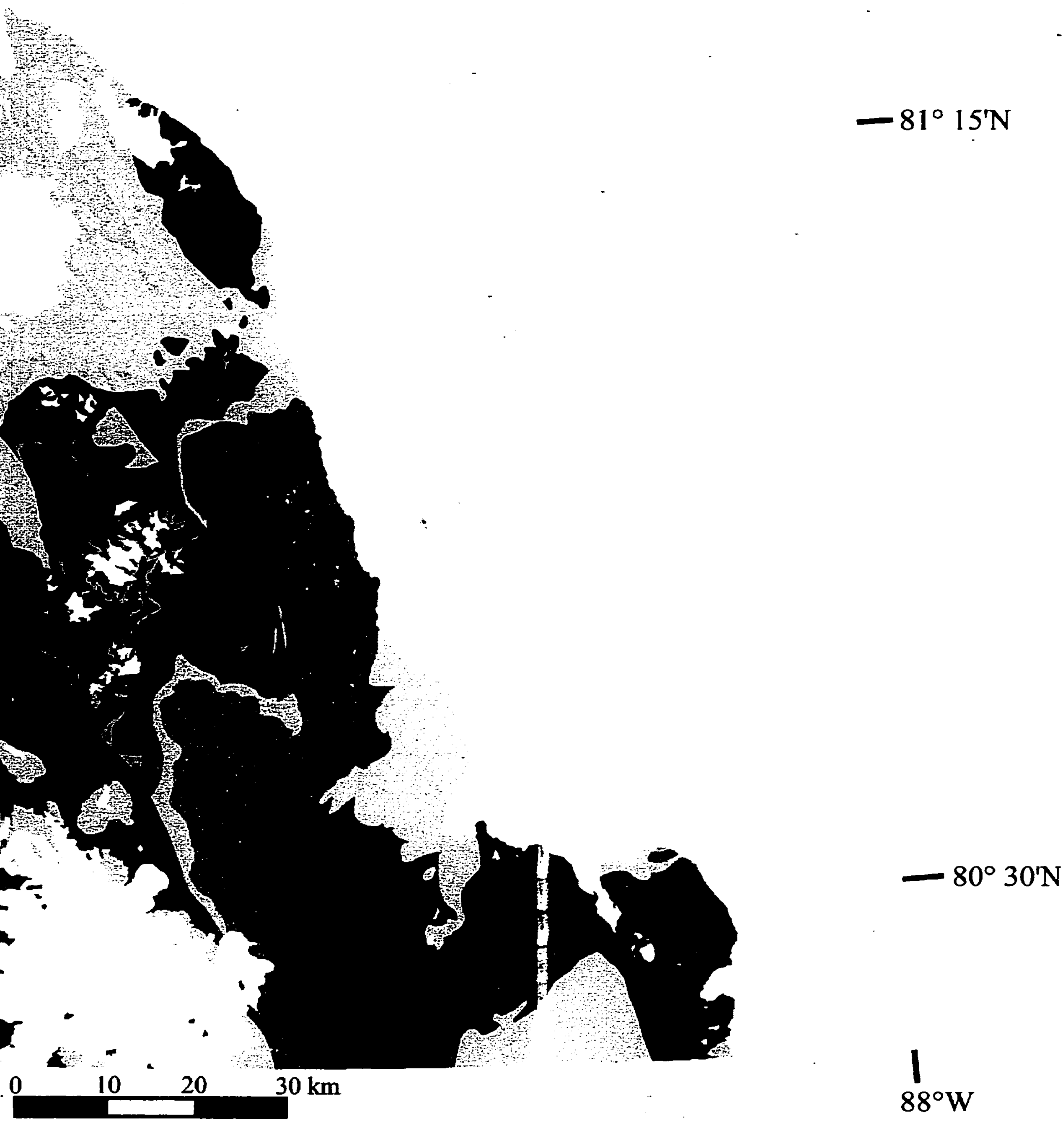
81° 15'N
80° 30'N
88°W
0
10
20
30 km

NORTHERN PART (Svartevaeg Cliff)

QUATERNARY

Q — *Quaternary sediments; gravel, sand, and mud*

TRIASSIC

BLIND FIORD FORMATION: medium grey siltstone, light grey-brown weathering; dark grey, silty shale; minor very fine to fine grained sandstone

PERMIAN

TROLD FIORD FORMATION: light green-brown and yellow, medium bedded, calcareous sandstone; silty chert; brachiopods common

SABINE BAY AND ASSISTANCE FORMATIONS, UNDIVIDED: buff, maroon or black sandstone, coal, shale and pyroclastics; plant fragments, brachiopods

ESAYOO FORMATION: red-black pillow basalt, volcanic breccia

GREAT BEAR CAPE FORMATION: light grey chert, weathers white; cherty, medium bedded limestone

RAANES FORMATION: brown, thin bedded, sandy limestone, shaly at base (see Note 6)

CARBONIFEROUS-PERMIAN

NANSEN FORMATION: grey, thick bedded to massive, fossiliferous limestone

CARBONIFEROUS

BORUP FIORD FORMATION: red weathering sandstone and conglomerate; minor limestone and siltsone

EMMA FIORD FORMATION: dark grey shale and sandstone; coal

CAMBRIAN TO DEVONIAN

COSD — *Undivided lower Paleozoic formations: slate, schist, phyllite, dolostone, sandstone, volcanics (see Note 8)*

SOUTHERN PART

QUATERNARY

?Quaternary sediments; gravel, sand, and mud

CRETACEOUS-TERTIARY

KTE — *EUREKA SOUND FORMATION: sandstone, conglomerate, siltstone, shale; minor coal*

CRETACEOUS

ISACHSEN FORMATION: white, fine to coarse grained sandstone; black basalt flows; dark green pyroclastic rocks, red weathering; minor shale, siltstone and conglomerate

JURASSIC AND CRETACEOUS

DEER BAY FORMATION: dark grey, silty shale; minor siltstone and sandstone
AWINGAK FORMATION: light brown, very fine to medium grained sandstone; minor shale and siltstone
RINGNES FORMATION: dark grey to black, silty shale; large dolomitic concretions
McCONNELL ISLAND FORMATION: medium dark grey shale; ironstone concretions
JAMESON BAY FORMATION: medium dark grey, silty shale; minor siltstone and sandstone

Undivided Awingak, Ringes, McConnell Island and Jameson Bay formations

TRIASSIC

HEIBERG FORMATION: white to light grey, medium fine grained sandstone; in lower part thick unit of med and siltstone; in upper part minor carbonaceous silt

BLAA MOUNTAIN GROUP

BLAA MOUNTAIN GROUP: undivided

BARROW FORMATION: medium to dark grey silty sh

HOYLE BAY FORMATION: medium to dark grey sha calcareous siltstone, in middle part light grey, very fin sandstone; in upper part light grey, calcareous siltsto

ROCHE POINT FORMATION: medium grey shale wi weathering ironstone concretions; medium to dark gr limestone, yellow weathering; medium grey, calcareo

MURRAY HARBOUR FORMATION: dark grey to blac minor siltstone

BLIND FIORD FORMATION: medium grey siltstone, medium to dark grey, silty shale; minor very fine graine

PERMIAN

LINDSTRÖM FORMATION: light green-grey, medium

VAN HAUEN FORMATION: very dark grey to black, m

TROLD FIORD FORMATION: buff and maroon sands or yellow, medium bedded, calcareous sandstone; ab

GREAT BEAR CAPE FORMATION: medium bedded l nodules; white chert in uppermost part

PTC — *TRAPPERS COVE FORMATION: chert, olive green, t limestone fleers (see Note 6)*

CARBONIFEROUS-PERMIAN

NANSEN FORMATION: thick bedded to massive lime

HARE FIORD FORMATION: very dark grey, thin bedd

Unnamed volcanics: green-black basalt flows

CARBONIFEROUS

HVITLAND PENINSULA FORMATION-Tellevak Memb

OTTO FIORD FORMATION: gypsum and anhydrite

BORUP FIORD FORMATION: sandstone and conglom minor limestone and siltstone

Unnamed volcanics

CAMBRIAN TO DEVONIAN

COSD — *Undivided lower Paleozoic formations: slate, schist, phy dolostone, sandstone, volcanics (see Note 8)*

NORTHERN PART (Svartevaeg Cliff)

uaternary sediments; gravel, sand, and mud

LIND FIORD FORMATION: medium grey siltstone, light grey-brown weathering; ark grey, silty shale; minor very fine to fine grained sandstone

ROLD FIORD FORMATION: light green-brown and yellow, medium bedded, alcareous sandstone; silty chert; brachiopods common

ABINE BAY AND ASSISTANCE FORMATIONS, UNDIVIDED: buff, maroon or black ndstone, coal, shale and pyroclastics; plant fragments, brachiopods

SAYOO FORMATION: red-black pillow basalt, volcanic breccia

REAT BEAR CAPE FORMATION: light grey chert, weathers white; cherty, medium dded limestone

ANES FORMATION: brown, thin bedded, sandy limestone, shaly at base ee Note 6)

JS-PERMIAN

NSEN FORMATION: grey, thick bedded to massive, fossiliferous limestone

JS

RUP FIORD FORMATION: red weathering sandstone and conglomerate; nor limestone and siltsone

MA FIORD FORMATION: dark grey shale and sandstone; coal

EVONIAN

divided lower Paleozoic formations: slate, schist, phyllite, dolostone, sandstone, canics (see Note 8)

PART

uaternary sediments; gravel, sand, and mud

ERTIARY

REKA SOUND FORMATION: sandstone, conglomerate, siltstone, shale; minor coal

CHSEN FORMATION: white, fine to coarse grained sandstone; black basalt flows; k green pyroclastic rocks, red weathering; minor shale, siltstone and conglomerate

RETACEOUS

ER BAY FORMATION: dark grey, silty shale; minor siltstone and sandstone
INGAK FORMATION: light brown, very fine to medium grained sandstone; minor shale l siltstone
GNES FORMATION: dark grey to black, silty shale; large dolomitic concretions
CONNELL ISLAND FORMATION: medium dark grey shale; ironstone concretions
ESON BAY FORMATION: medium dark grey, silty shale; minor siltstone and sandstone

ivided Awingak, Ringes, McConnell Island and Jameson Bay formations

TRIASSIC

HEIBERG FORMATION: white to light grey, medium to thick bedded, very fine to fine grained sandstone; in lower part thick unit of medium to dark grey shale and siltstone; in upper part minor carbonaceous siltstone and shale

BLAA MOUNTAIN GROUP

BLAA MOUNTAIN GROUP: undivided

BARROW FORMATION: medium to dark grey silty shale; medium grey, argillaceous siltstone

HOYLE BAY FORMATION: medium to dark grey shale; medium grey, variably calcareous siltstone, in middle part light grey, very fine to fine grained sandstone; in upper part light grey, calcareous siltstone

ROCHE POINT FORMATION: medium grey shale with brown-grey weathering ironstone concretions; medium to dark grey, silty, micritic limestone, yellow weathering; medium grey, calcareous siltstone

MURRAY HARBOUR FORMATION: dark grey to black shale; phosphatic nodules; minor siltstone

BLIND FIORD FORMATION: medium grey siltstone, light green-grey weathering; medium to dark grey, silty shale; minor very fine grained sandstone (see Note 7)

PERMIAN

LINDSTRÖM FORMATION: light green-grey, medium bedded chert

VAN HAUEN FORMATION: very dark grey to black, medium to thin bedded chert

TROLD FIORD FORMATION: buff and maroon sandstone and shale; light grey-brown or yellow, medium bedded, calcareous sandstone; abundant brachiopods (see Note 3)

GREAT BEAR CAPE FORMATION: medium bedded limestone with abundant chert nodules; white chert in uppermost part

PTC

TRAPPERS COVE FORMATION: chert, olive green, thin to medium bedded; limestone flasers (see Note 6)

CARBONIFEROUS-PERMIAN

NANSEN FORMATION: thick bedded to massive limestone, grey weathering

HARE FIORD FORMATION: very dark grey, thin bedded, argillaceous limestone and chert

Unnamed volcanics: green-black basalt flows

CARBONIFEROUS

HVITLAND PENINSULA FORMATION-Tellevak Member: reefal limestone

OTTO FIORD FORMATION: gypsum and anhydrite

BORUP FIORD FORMATION: sandstone and conglomerate, red weathering, minor limestone and siltstone

Unnamed volcanics

CAMBRIAN TO DEVONIAN

CDSD

Undivided lower Paleozoic formations: slate, schist, phyllite, dolostone, sandstone, volcanics (see Note 8)

weathering of the more resistant Carboniferous-Permian strata results locally in higher relief slopes (Fig. 14) that act as corner reflectors resulting in a high radar backscatter for the fore-slopes and a low radar backscatter for the back-slopes. Consequently, these areas adopt distinctive, but variable bright and dark tones on the radar images (Figs. 11b and 12). Inversely, the Northern Heiberg Fold Belt mainly characterized by low relief slopes present a more uniform darker tone (Figs. 11b and 12). This tonal radar difference is also exemplified in the enlarged area of Figure 15 where the locally faulted contact separating the Northern Heiberg Fold belt and the Sverdrup Basin succession is easily recognized.

Intra Sverdrup Basin Contact

The generally conformable contact (Embry, 1991) between the Carboniferous-Permian and Triassic-Cretaceous successions of the Sverdrup Basin is also recognized on the RADARSAT-1 images using tonal radar differences (Fig.11b). Figure 16 shows the difference in topographic relief and consequently in the tone variations between these two successions of the Sverdrup Basin. The thick bedded to massive limestone of the Carboniferous-Permian Nansen Formation and the medium bedded limestone with chert nodules of the Permian Great Bear Cape Formation (Mayr *et al.*, 1998) show high relief slopes in the field (Fig. 14), thus giving a bright radar tone on the fore-slopes and a darker tone on the back-slopes (Fig.16a). The Triassic formations with lower relief slopes have a relatively dark tone on the RADARSAT-1 image (Fig.16a). The contact between these two successions as well as other visualization products derived from RADARSAT-1 images are illustrated in Figure 16.

Figure 14. Field photographs showing examples of the high relief slopes of the Carboniferous-Permian succession. Figures 14a and b both illustrate medium bedded limestone and chert strata of the Great Bear Cape Formation (Mayr *et al.*, 1998). These photographs have been taken approximately 25 km north-east of Bukken Fiord.

a

b

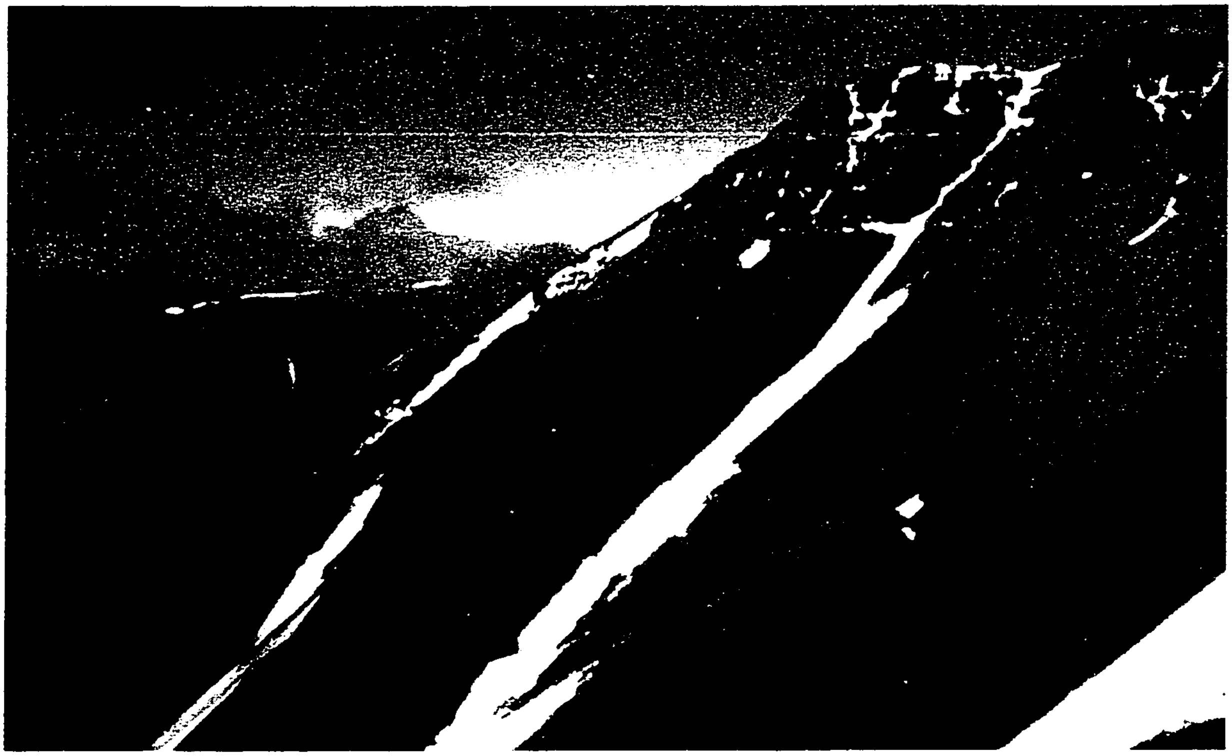

Figure 15. This figure illustrates the contact between the Franklinian Mobile Belt and the Sverdrup Basin successions: a) Standard 7 ortho-image integrated with the simplified geological map contacts (from Mayr *et al.*, 1998), b) simplified geological map (from Mayr *et al.*, 1998), and c) fusion of the simplified geological map with the Standard 7 ortho-image. This contact is an angular unconformity but locally the Northern Heiberg Fold Belt formations are thrust faulted over the Sverdrup Basin formations. The quartzite, phyllite and slate of the Lower Cambrian Grant Land Formation of the Northern Heiberg Fold Belt adopt a relatively uniform dark tone while the limestone and chert formations of the Carboniferous-Permian succession show a distinctive but variable bright and dark tone. The acquisition parameters are listed below the sub-images. For location of the sub-area see Figure 2.

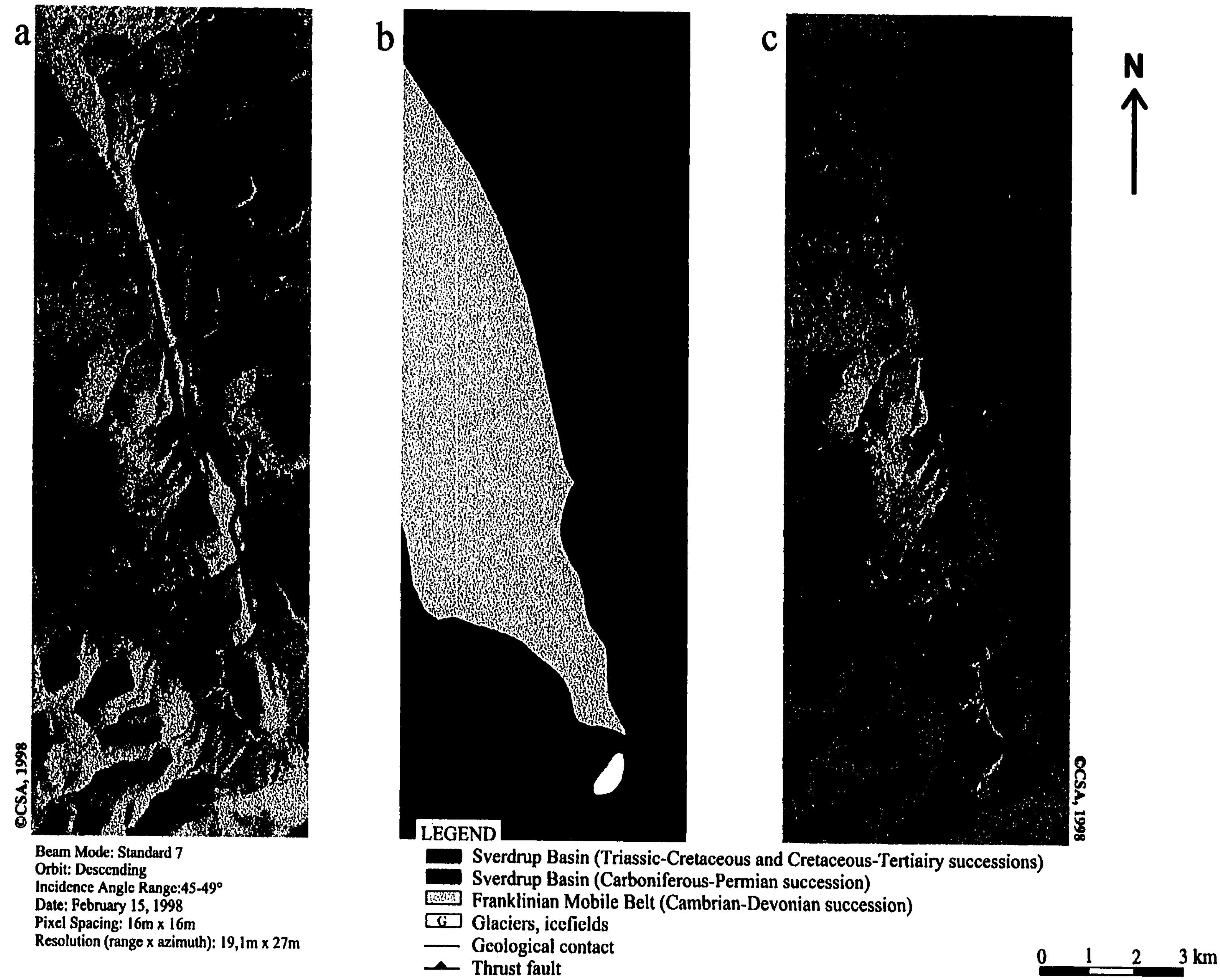

a
b
c
N
©CSA, 1998
©CSA, 1998
Beam Mode: Standard 7
Orbit: Descending
Incidence Angle Range:45-49°
Date: February 15, 1998
Pixel Spacing: 16m x 16m
Resolution (range x azimuth): 19,1m x 27m
LEGEND
Sverdrup Basin (Triassic-Cretaceous and Cretaceous-Tertiairy successions)
Sverdrup Basin (Carboniferous-Permian succession)
Franklinian Mobile Belt (Cambrian-Devonian succession)
G Glaciers, icefields
Geological contact
Thrust fault
0 1 2 3 km

Figure 16. These sub-images illustrate the geological contact between the Carboniferous-Permian and the Triassic-Cretaceous successions of the Sverdrup Basin: a) Standard 7 ortho-image integrated with the simplified geological map contacts (from Mayr *et al.*, 1998), b) detailed geological map (from Mayr *et al.*, 1998), and c) fusion of the detailed geological map with the Standard 7 ortho-image, d) perspective image of a (see c for look direction), e) perspective image of c (see c for look direction), f) perspective image of the chromo-stereoscopic image (see c for look direction). This contact between these successions is well recognized according to the tonal radar variations. The Carboniferous-Permian formations adopt a distinctive but variable bright and dark tone that contrast with the more uniform darker tones of the Triassic-Cretaceous formations. The locally faulted contact is well illustrated in the perspective images with their relief representation. The high relief of the Carboniferous-Permian formations differs from the lower relief of the Triassic-Cretaceous succession. Cretaceous dykes mapped by Thorsteinsson and Trettin (1972a) are also visible on these sub-images. The acquisition and the perspective images generation parameters are listed below the sub-images. For location of the sub-area see Figure 2.

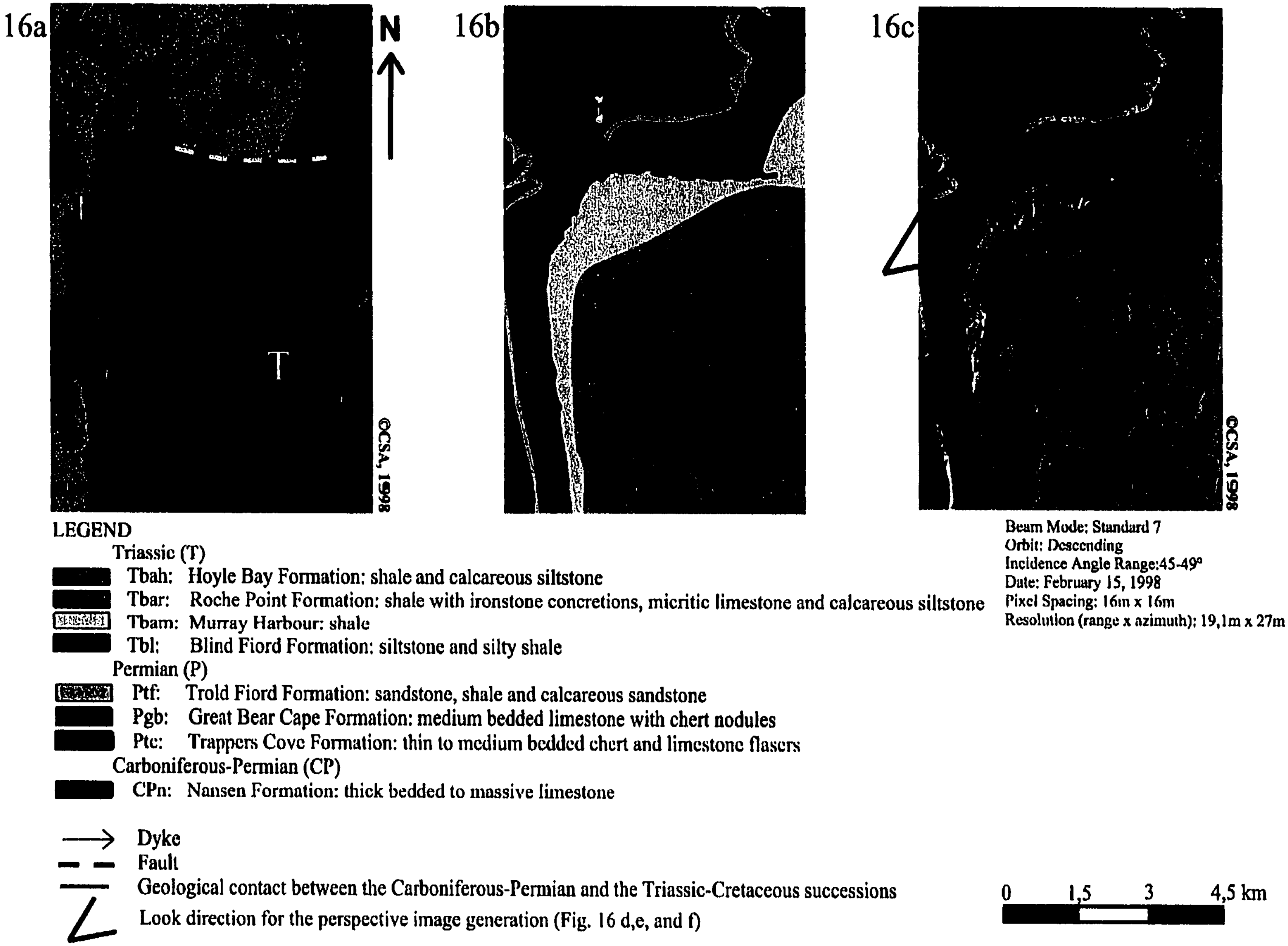
16a
N
T
©CSA, 1998
16b
16c
©CSA, 1998
LEGEND
Triassic (T)
Tbah: Hoyle Bay Formation: shale and calcareous siltstone
Tbar: Roche Point Formation: shale with ironstone concretions, micritic limestone and calcareous siltstone
Tbam: Murray Harbour: shale
Tbl: Blind Fiord Formation: siltstone and silty shale
Permian (P)
Ptf: Trold Fiord Formation: sandstone, shale and calcareous sandstone
Pgb: Great Bear Cape Formation: medium bedded limestone with chert nodules
Ptc: Trappers Cove Formation: thin to medium bedded chert and limestone flasers
Carboniferous-Permian (CP)
CPn: Nansen Formation: thick bedded to massive limestone
Dyke
Fault
Geological contact between the Carboniferous-Permian and the Triassic-Cretaceous successions
Look direction for the perspective image generation (Fig. 16 d,e, and f)
Beam Mode: Standard 7
Orbit: Descending
Incidence Angle Range:45-49°
Date: February 15, 1998
Pixel Spacing: 16m x 16m
Resolution (range x azimuth): 19,1m x 27m
0
1,5
3
4,5 km

16d

N E

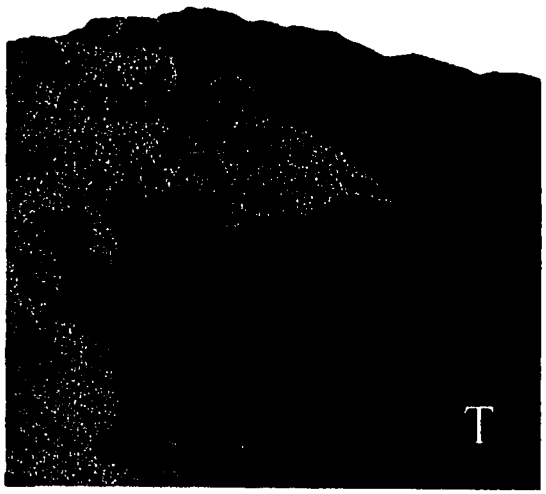

Beam Mode: Standard 7
Orbit: Descending
Incidence Angle Range:45-49°
Date: February 15, 1998
Pixel Spacing: 16m x 16m
Resolution (range x azimuth): 19,1m x 27m

16e

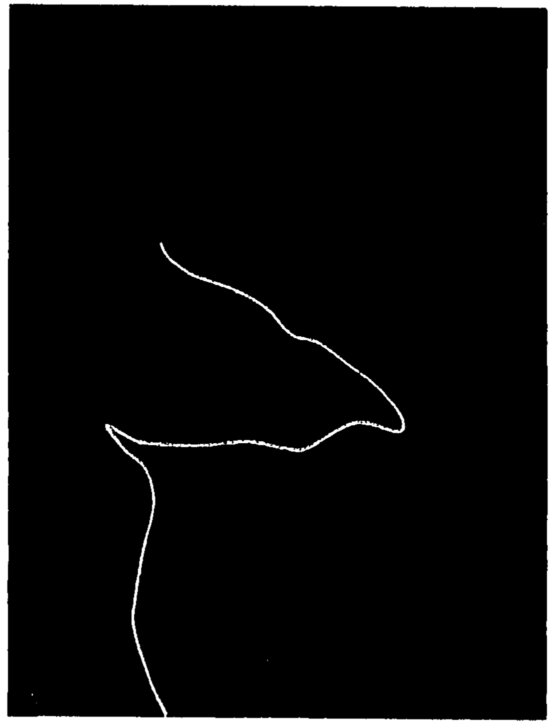

16f

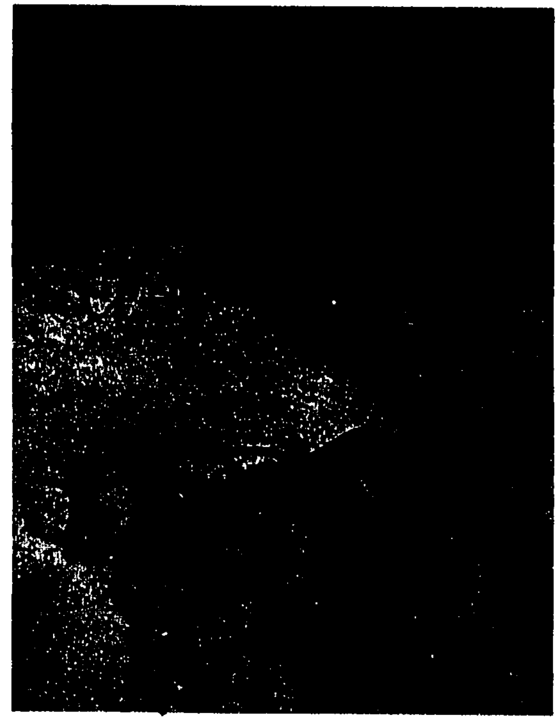

PERSPECTIVE IMAGE GENERATION PARAMETERS
Field of View Angle = 30°
View Angles: Direction = 45°N, Inclination = 45°
Elevation Exaggeration = 2
Viewing Height ~ 1350m (above sea level)
Front Pixels ~ 200

Quaternary Sediments

The contact with the overlying Quaternary sediments is well defined on RADARSAT-1 images (Fig. 9). The important Quaternary sediments (Mayr *et al.*, 1998; Trettin, 1996) present in the northern part of the study area represent glaciation drift sediments and fragments resulting from bedrock weathering. As mentioned previously in the Soil Moisture section, the delineation of the contact in RADARSAT-1 images is maximized in winter because of the dark radar tone of the Quaternary sediments with respect to the brighter tone of the bedrock. This increased contrast in the winter is explained by the reduced effects of the dielectric constant on the radar backscatter when the active layer is completely frozen (Fig. 9a *versus* 9b).

Meso Scale Mapping (1:250 000 to 1:125 000)

This sub-section will evaluate the RADARSAT-1 potential for mapping at formation scale. As mentioned above, formational units developed a specific surface roughness and topographic relief relative to their composition. Resistant units tend to fracture in larger fragments compare to non-resistant units in response to weathering processes. This phenomenon will cause different surface roughness influencing the tone and texture present in a radar image. Dipping formations and formations with locally high relief slopes due to weathering will display a different tone than formations with low relief slopes. Thus, the radar tone and texture used to identify these formations are related to surface roughness and topography when the soil moisture effect is minimized by the acquisition of winter images.

Figure 5 illustrates lower Paleozoic NW-SE striking formations of the Northern

Heiberg Fold Belt (Trettin, 1996; 1998) overlain by Quaternary sediments. These lower Paleozoic formations with moderate topography display a brighter tone helping their identification and delineation with respect to the Quaternary sediments.

In low relief areas, the lithological mapping of various formational units is also possible. The radar.backscatter of these units is largely controlled by the surface roughness rather than topography. Figure 10 illustrates two formations of the Northern Heiberg Fold Belt. The dolostone forming the Aurland Fiord Formation shows a relatively bright tone because this resistant formation is breaking into large fragments (Fig.10). Conversely, the quartzite, phyllite and slate of the Grant Land Formation are more easily weathered resulting into finer fragments and into a darker tone on the RADARSAT-1 image (Fig. 10). The contact is easily traced between these two formations using radar tone variations.

Figure 17 displays typical Triassic formations of the Sverdrup Basin identified with RADARSAT-1 images. The resistant shale with ironstone concretions of the Triassic Roche Point Formation is traced on the Standard 7 radar image. This formation characterized by high relief slopes displays a bright backscatter contrasting with the darker backscatter of the less resistant shales of the adjacent Murray Harbour and Hoyle Bay formations (Fig. 17).

Micro Scale Mapping (<1: 60 000)

This sub-section investigates the capabilities of RADARSAT-1 images to identify geological structures at the outcrop scale. Lithological mapping and strike/dip calculation examples are discussed below.

Figure 17. This figure illustrates the south plunging syncline-anticline structure intruded by Cretaceous mafic dykes: a) Standard 7 ortho-image overlaid by the detailed geological map contacts (from Mayr *et al.*, 1998), b) fusion of the detailed geological map with the Standard 7 ortho-image, c) perspective image of the chromo-stereoscopic image (see b for look direction). This Triassic fold is well seen on the images because of the bright radar tone of the resistant shale with ironstone concretions mainly forming the Triassic Roche Point Formation. The radar backscatter from the Roche Point Formation is also able to discriminate internal layering allowing possible formational sub-unit mapping. The N-S striking mafic dykes crosscutting these units are also recognized by their bright elongated radar trace. The acquisition and the perspective images generation parameters are listed below the sub-images. Geological interpretation is derived from Mayr et al. (1998) and Thorsteinsson and Trettin (1972a). For location of the sub-area see Figure 2.

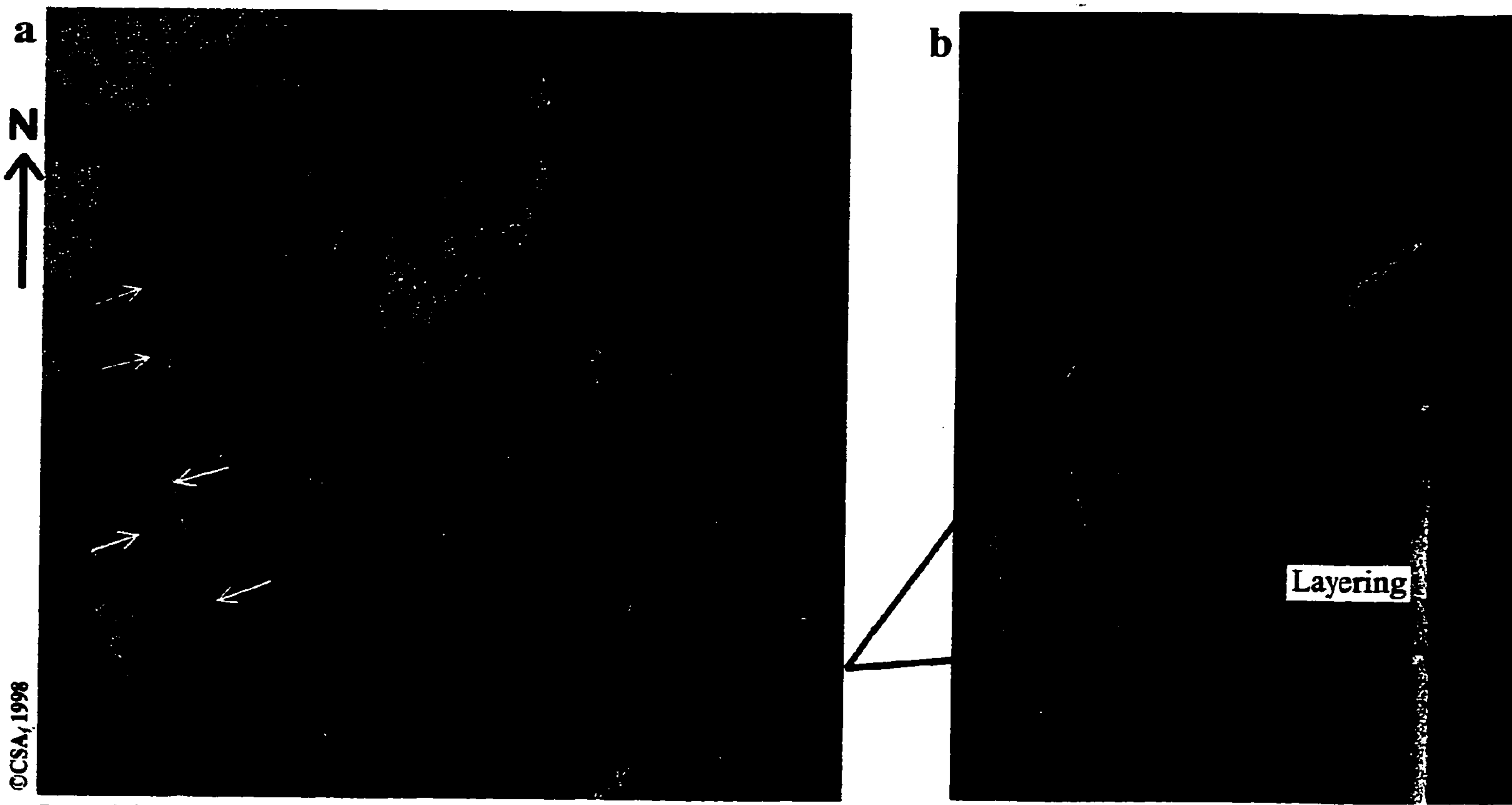

Beam Mode: Standard 7
Orbit: Descending
Incidence Angle Range:45-49°
Date: February 15, 1998
Pixel Spacing: 16m x 16m
Resolution (range x azimuth): 19,1m x 27m

0 2 4 6 km

Beam Mode: Standard 7
Orbit: Descending
Incidence Angle Range:45-49
Date: February 15, 998
Pixel Spacing: 16m x 16m
Resolution (range x azimuth):

LEGEND

Triassic (T)

- Tbah: Hoyle Bay Formation: shale and calcareous siltstone
- Tbar: Roche Point Formation: shale with ironstone concretions, micritic limestone and calcareous siltstone
- Tbam: Murray Harbour: shale
- Tbl: Blind Fiord Formation: siltstone and silty shale

Permian (P)

- Ptf:Trold Fiord Formation: sandstone, shale and calcareous sandstone
- Pgb:Great Bear Cape Formation: medium bedded limestone with chert nodules
- Ptc:Trappers Cove Formation: thin to medium bedded chert and limestone flasers

Carboniferous-Permian (CP)

- CPn: Nansen Formation: thick bedded to massive limestone
- Bedding
- Geological contact between the Carboniferous-Permian and the Triassic-Cretaceous successions
- Geological contacts between the Carboniferous to Cretaceous formations
- Dyke
- Fold axis: syncline, anticline
- Look direction for the perspective image generation (Fig. 17c)

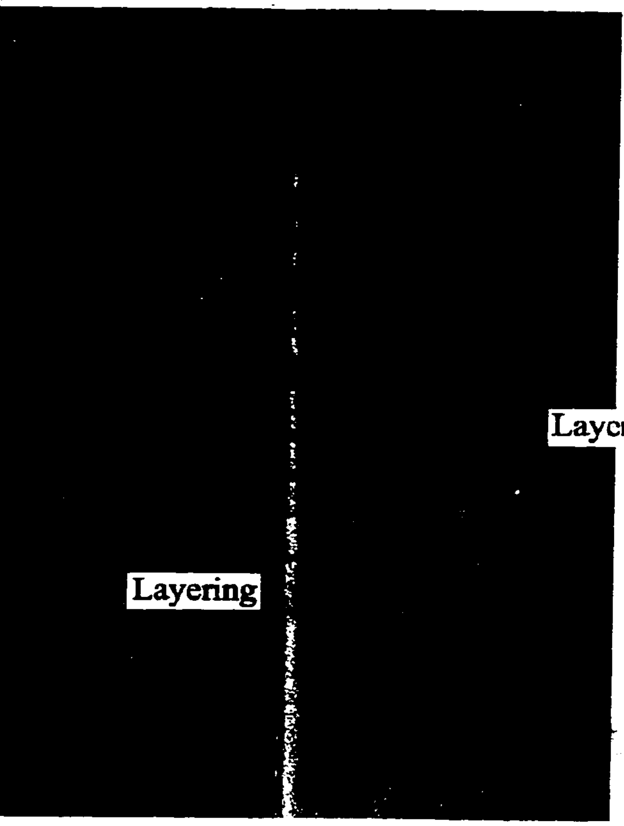

Beam Mode: Standard 7
Orbit: Descending
Incidence Angle Ra: ;e:45-49°
Date: February 15, 1·98
Pixel Spacing: 16m x 16m
Resolution (range x ε :imuth): 19,1m x 27m

lcareous siltstone

essions

c

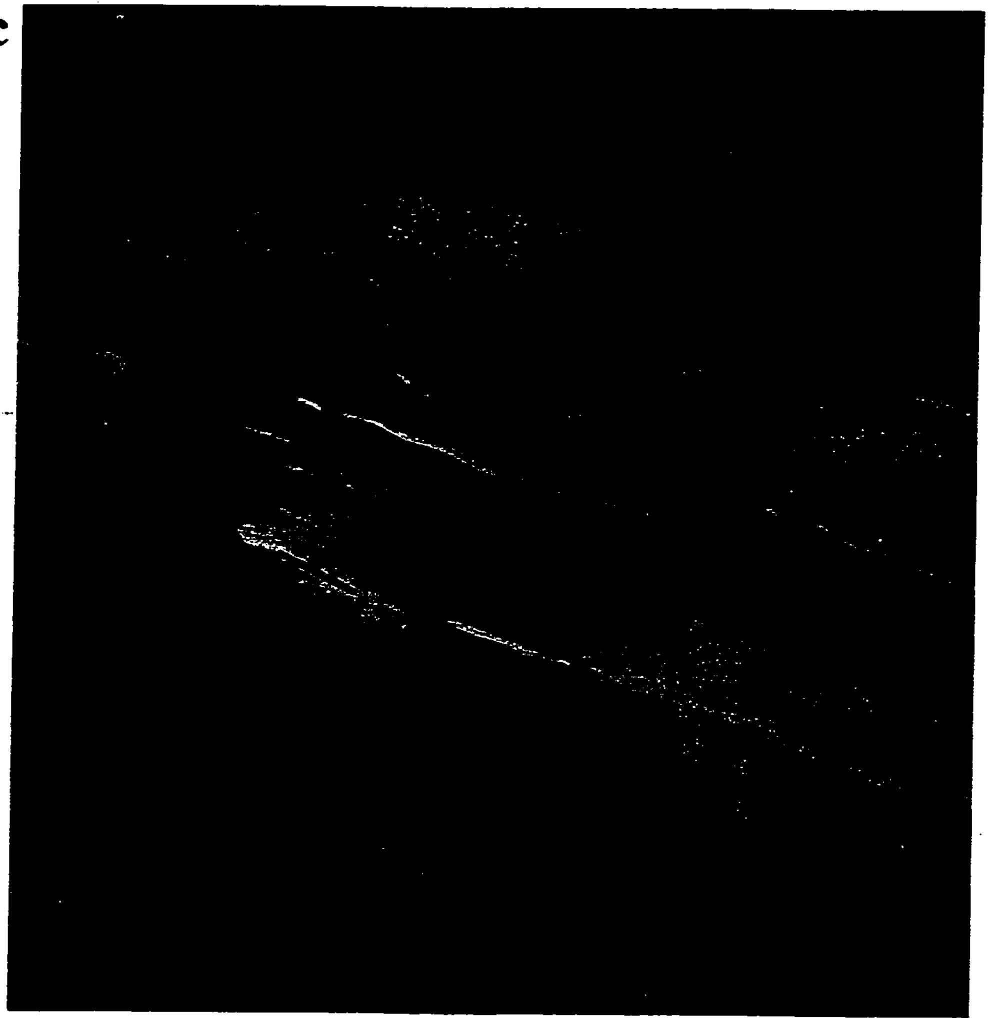

PERSPECTIVE IMAGE GENERATION PARAMETERS
Field of View Angle = 30°
View Angles: Direction = 45°N, Inclination = 45°
Elevation Exaggeration = 2
Viewing Height =2000m (above sea level)
Front Pixels = 200

Figure 18 illustrates formations present in the Northern Heiberg Fold Belt and Quaternary sediments. On both sub-scenes (Figs.18a and b), the sub-units of Member A and Member B of the Stallworthy Formation are recognized. At that scale the radar backscatter is more influenced by the surface roughness than the topography; especially in winter when the soil moisture effect is greatly reduced. When comparing the orthorectified Fine 3 Far beam mode sub-image (Fig.18 a) and the aerial ortho-photo sub-image (Fig.18 b), the amount of extractable geological features is similar but: i) the ortho-photo displays more detail because of an higher spatial resolution (2,5m x 2,5m versus 7,6m x 8,4m for the Fine 3 Far ortho-image) and ii) the radar sub-image facilitates the identification of geological structures because of the greater sensibility of the radar backscatter signal to surface characteristics.

Another example of the potential of RADARSAT-1 images for mapping micro scale is illustrated in Figure 17 where unmapped sub-units in the Roche Point Formation are present. Their identification facilitated by the presence of a distinctive succession of bright and dark tones is related to local surface roughness variations controlled by lithological variations in the field.

At the scale of the outcrop, strike/dip calculation for a given geological surface can be derived from a RADARSAT-1 ortho-image and a DEM. The calculation requires three points or more with X, Y and Z components chosen on the same strata (Haneberg, 1990). The calculation was performed using the DIP program of PCI (v.6.3) that used the equations described in Haneberg (1990). Three regions have been selected to evaluate the strike and dip

Figure 18. This figure illustrates sub-units of the Northern Heiberg Fold Belt that are unmapped on the geological map of Trettin (1996). These sub-units, present in the Member A (chert pebble conglomerate, quartzose sandstone and siltstone) and Member B (quartzose sandstone, chert pebble and coble conglomerate and breccia) of the Stallworthy Formation are recognized in both sub-images of Figures 18. These sub-units are more visible in the radar ortho-image (Fig. 18a) because of the pronounced tonal variations even if the spatial resolution of the ortho-photo is greater (Fig. 18b). The acquisition parameters are listed below the sub-images. The geological contacts are derived from Trettin (1996). For location of the sub-area see Figure 2.

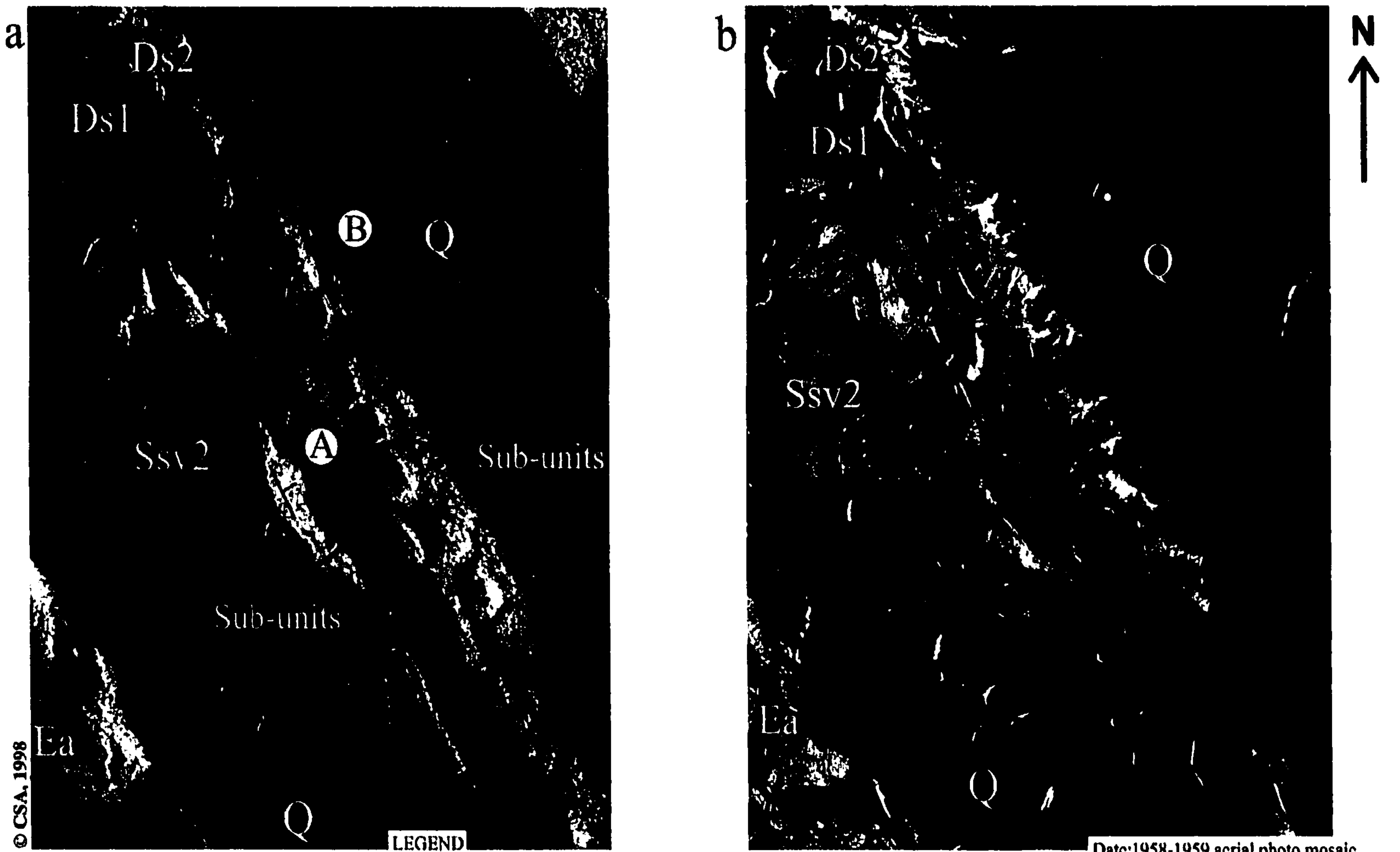

Beam Mode: Fine 3 Far
Orbit: Descending
Incidence Angle Range:41,8 - 44,3°
Date: February 11, 1998
Pixel Spacing: 8m x 8m
Resolution (range x azimuth): 7,6m x 8,4m

0 1 2 3 km

LEGEND

Quaternary
Q Unconsolidated sediments
Upper Silurian(?) and Lower Devonian
Ds2 Quartzose sandstone, chert pebble and coble conglomerate and breccia of the Member B, Stallworthy Formation
Ds1 Chert pebble conglomerate, quartzose sandstone and siltstone of the Member A, Stallworthy Formation
Lower Silurian
Ssv2 Volcanogenic sandstone, mudrock and minor conglomerate of the Svartevaeg Formation
Cambrian and/or older
Ea Dolostone of the Aurland Fiord Formation
Eetookashoo Bay Thrust fault
Bedding
Geological contact
(A) Region 1 for strike/dip calculation, Member A

Date:1958-1959 aerial photo mosaic
Pixel Spacing: 5m x 5m
Resolution (range x azimuth): 2,5m x 2,5m

calculation using this photogrammetric method including: i) region 1 composed of the Member A and Member B of the Stallworthy Formation, Northern Heiberg Fold Belt (east of Rens Fiord, Figs. 2 and 18), ii) region 2 composed of Triassic strata forming part of a thrust fault complex in the Sverdrup Basin (north of Bukken Fiord, Fig. 2), and iii) region 3 composed of similar strata but located 25km further south-west of region 2 (on Bjarnason Island, Fig. 2). The results were compared with measurements in the field. Table 8 summarizes calculated and field measured strike/dip for the three regions. In general, the calculated strike/dip values are similar with those measured in the field (see below Table 8).

Test region #	Calculated strike (°N) (DIP program in PCI)	Calculated dip (°) (DIP program in PCI)	Measured strike (°N) (Trettin, 1996; Mayr *et al.*, 1998)	Measured dip (°) (Trettin, 1996; Mayr *et al.*, 1998)
1, Member A	337	34	339	42
1, Member A	337	34	339	42
1, Member B	330	65	333	63
1, Member B	331	73	333	63
1, Member B	330	57	333	63
2	143	56	133, 129	70, 65
2	143	63	133, 129	70, 65
3	202	71	198	60
3	209	56	198	60
3	203	74	198	60
3	202	82	198	60

Table 8. Results from strike/dip calculation using a photogrammetric method for three regions in the study area.

Results with this method are excellent but important factors must be considered: 1) factors relative to the location of the three points and 2) factors relative to the DIP program. First, the location errors depend on the accuracy of the DEM and the radar image used in the calculation. The radar image, from which the X and Y components are derived for the calculation, must be orthorectified to minimize the geometric distortions induced by the side-looking sensor of the radar platforms. In addition, the accuracy of the DEM used to assign the three points' elevation (Z component) influence the strike/dip results. Furthermore, the radar image representation of geological surfaces may not facilitate the location of the three points. For example, strata oriented closely perpendicular to the look direction are best highlighted by showing a bright backscatter signal on the radar images. Unlike low dipping strata, highly dipping strata have a brighter tone on the radar image that facilitate their identification.

The image analyst must be aware of the DIP program functionality to calculate accurate strike/dip measurements. First, the three points have to be selected on the edge instead of on the apparent surface formed by the strata. When the three points are selected on the apparent surface of the strata, the calculated dip can be a measure of the local relief rather than the true dip. This is especially true in arctic environments where important physical weathering processes are currently active resulting locally in high relief slopes formed by the weathered fragments.

Structural Mapping

This section will present examples of thrusts, faults, intrusions and folds that are mappable from the RADARSAT-1 images.

Faults

The major thrust faults present in the study area are easily distinguished because of the abrupt change in topographic relief. The thrust faults are visible because of the tonal variations associated with contrasting lithologies along the fault trace. Figure 7 illustrates a thrust fault defined by the radar contrast between the variable bright and dark tones of the Carboniferous-Permian formations and the more uniform darker tone of the Triassic-Cretaceous formations. A similar example is presented in Figure 15 illustrating the Cambrian-Devonian succession thrust faulted over the Sverdrup Basin successions.

Normal, inverse and oblique faults present in the study area can be traced on the radar images. The amount of relative displacement is sometimes visible and can be approximated as illustrated in Figure 16. An inverse fault displaces the geological contact between the Carboniferous-Permian and the Triassic-Cretaceous successions of the Sverdrup Basin. This displacement is recognized because of the important tonal variation between the formations. The bright tones of the medium bedded limestone with chert nodules of the Great Bear Cape and the sandstone and shale of the Trold Fiord Permian formations contrast with the darker tones of the siltstone and the silty shale of the Triassic Blind Fiord Formation (Fig.16).

Dykes

Mafic dykes of mainly Cretaceous age intrude the Grant Land and Aurland Fiord formations of the Northern Heiberg Fold Belt located south of the Rens Fiord as well as the Carboniferous-Permian and the Triassic-Cretaceous successions of the Sverdrup Basin (Trettin, 1998). These N-S striking dykes are traced on the images because these resistant units act like corner reflectors causing high radar backscatter and enabling them to be recognized. Figure 17 illustrates dykes cross-cutting Triassic formations that are well defined by their very bright elongated radar trace. The dykes that intruded the Carboniferous-Permian succession of the Sverdrup Basin are not so clearly identified on the RADARSAT-1 images because of the relatively bright radar tone and intense topographic displacement associated with this locally high relief slope area: these factors mask their recognition.

Folds

Folds are also mapped on the RADARSAT-1 images. Anticlines and synclines, locally plunging, are recognized using stereoscopy and/or traditional photogeology techniques. The sensitivity of the radar to the topographic variation enables a good representation of the more resistant units forming folds. As an example, Figure 17 illustrates a south plunging syncline-anticline structure. This folded structure is defined by the bright radar tone of the resistant shales with ironstone concretions of the Triassic Roche Point Formation. The presence of layering is here helpful to define the continuity of the structure. The strike and dip representation of this fold structure is visible in the perspective image (Fig. 17c).

Airborne *versus* Satellite Platforms

Satellite platforms offer several advantages in comparison with the airborne platforms. First the cost is significantly lower when buying satellite images because the satellite is already in place and ready to acquired images while for airborne images, a flight mission must be planned where the plane must be sent to the study area with a crew. In addition, the acquisition frequency is higher with satellite platforms. For example, RADARSAT-1 can acquire the same beam mode image of a certain area of the world every 24 days. For arctic regions, an image covering a specific area can be acquired every day without considering a specific beam mode (RADARSAT User Guide, 1998).

Radar *versus* Optical Imagery

In addition to the capacity of radar platforms to acquire images independently of the cloud cover and the illumination conditions, radar can be used to monitor changes in the characteristics of the imaged terrain. For instance, changes in soil moisture can be more easily detected and mapped with radar images in comparison with optical imagery. The sensibility of radar platforms to surface roughness variations allows a good discrimination of various lithologies. Finally, relief differences are well represented on radar images where a large range of incidence angles is available.

RADARSAT-1 has an on-board tape recorder, in comparison with Landsat5, allowing acquisition of images for regions located outside of the covering extent of the Prince Albert reception station (RADARSAT User Guide, 1998). The northern extent of the Prince Albert reception station is south of our study area (Ben Foster, RADARSAT International, pers. comm.); thus explaining why Landsat 5 images were not used in our study.

RADARSAT-1 Images as part of a Geological Mapping Project

The satellite RADARSAT-1 is an important tool for geological mapping in the Canadian High Arctic. The RADARSAT-1 satellite is able of acquiring images with different resolutions, incidences angle, areas of coverage and also two different look directions (ascending and descending). Furthermore, the radar wavelength can penetrate cloud cover and a certain thickness of dry snow. This active sensor can acquire images day and night;

being especially suitable for arctic areas where complete darkness prevails in winter, and cloud and snow cover prevents image acquisition by optical sensors.

Arctic environments are hard to access and field campaigns are costly with a short field season. In preparation for field campaign, RADARSAT-1 images can be useful at the planning level. Preliminary investigations using these images can first give an overview of the major lithological and structural features present in the study area. RADARSAT-1 images cover several square kilometers enabling the possibility of regional investigations. As an example, our study area is covered by a single Standard beam mode (100km x 100km) whereas 37 aerial photos (1:60 000) cover only approximately one quarter of the same area. Regional structures are then easily recognized and the future field campaigns can be planned to identify and/or validate the preliminary interpretation. Fewer sites have to be visited in comparison to a traditional field campaign enabling a time and cost economy.

As demonstated in this project, several derived products can be produced from RADARSAT-1 images. The Standard 3 and 7 beam mode images are good examples. First a preliminary lithological and structural interpretation has been realized, assisted with stereoscopy. A DEM was generated from this stereo-pair. The DEM was used for orthorectification of the images to remove the geometric distortions. Various data integrations (i.e. vector overlay and fusion) were done using the Standard 7 ortho-image with the geological information or the DEM. Using the altimetric information of the DEM, perspective images were generated from the ortho-image and the integrated images. Finally, the generated DEM was used to calculate strike and dip in the study area. All these products enable an excellent lithological and structural mapping based on radar signatures variations. As described above, several formational units and sub-units could be mapped in our study area by radar imagery indicating that a similar approach may be applicable to other parts of the Canadian Arctic. In addition, the technique of mapping temporal variations in the active layer state using multi-date RADARSAT-1 images is also applicable in other permafrost regions of the world.

CONCLUSIONS

This study demonstrates the use of RADARSAT-1 imagery for lithological and structural mapping in the Canadian High Arctic including:

i) The identification of the geological contacts between the geological provinces, formations and even locally unmapped sub-units.

ii) The recognition of dykes, thrusts, faults, and folds.

iii) The identification of geological features in mountainous areas that are best seen in images acquired with a higher incidence angle.

iv) The recognition of strata dip especially when the dip direction is matching the radar look direction.

v) The identification of well defined seasonal effects due to active layer melting. This effect must be taken into account for geological mapping with RADARSAT-1 images. Lithological contrast is maximized in winter images when the active layer is frozen.

vi) The generation of accurate DEM from RADARSAT-1 stereo-pairs when the radiometric disparities are minimized while the geometric disparities are maximized between the two images.

vii) The creation of precise orthorectified RADARSAT-1 images.

viii) The development of integrated products resulting from the geological contacts overlay and the fusion of the orthorectified image with the geological map or the DEM (i.e. chromo-stereoscopic image) that are very useful for the geological interpretation.

ix) The creation of perspective images using ortho-images or integrated images with a DEM.

RADARSAT-1 ACQUISITION PARAMETERS RECOMMENDATIONS

This section based on our results will suggest the most useful RADARSAT-1 acquisition parameters for lithological and structural mapping in an arctic environment.

- In low relief areas, low incidence angle images (Standard and Fine beam modes images with lower incidence angles) should be acquired to enhance as much as possible the geological structures by maximizing the topographic displacement. On the other hand, higher incidence angles images (Extended high images with incidence angles ranging from 49° to 59°) should be considered in high relief regions to minimize the topographic displacement. Extended high images should always be acquired because of the higher incidence angle capability of this beam mode (from 49° to 59°) in opposite to Standard and Fine images that can only be acquired with a maximum incidence angle of 49° and 48° respectively.
- Because of the complementary representation of earth surface given by opposing orbits, both orbits (i.e. ascending and descending) should be considered for geological mapping. Also, images should be acquired if possible with a look direction

perpendicular to the orientation of geological structures to increase the identification potential.

- To allow the best lithological unit discrimination, especially where Quaternary sediments are present, images should be acquired in winter when the contrast is maximized between bedrock and the sediments because of the frozen state of the active layer.
- For a large-scale geological study, images with different resolution should be acquired. Standard beam modes are used for regional geological reconnaissance and for DEM generation because of their large area of coverage. Fine modes are required for more detailed analysis because of their higher resolution.
- SGX images should be acquired because of their smaller pixel spacing, even if their file size is larger.

	Acquisition parameters				
Geological features	Incidence angle – low relief	Incidence angle – high relief	Orbit	Date of acquisition	Resolution
Dyke	Lower	Higher	Ascending and descending, as perpendicular as possible	Winter	Standard, Extended High and Fine
Thrust fault	Lower	Higher, on back-slopes	Ascending and descending, on back-slopes, as perpendicular as possible	Winter	**<u>Extended High</u>**, Standard and Fine
Fault	Lower	Higher	Ascending and descending, as perpendicular as possible	Winter	Standard, Extended High and Fine
Fold	Lower	Higher	Ascending and descending	Winter	Standard, Extended High and Fine
Strike and dip representation	Higher, matching the orbit	Higher, matching the orbit	Ascending and descending, as perpendicular as possible	Winter	**<u>Fine</u>**, Standard and Extended High
Geological contact - macro scale	Lower to Higher	Lower to Higher	Ascending and descending, as perpendicular as possible	Winter	**<u>Standard</u>**, Extended High and Fine
Geological contact - meso scale	Lower	Higher	Ascending and descending, as perpendicular as possible	Winter	**<u>Standard</u>**, Extended High and Fine
Geological contact -micro scale	Lower	Higher	Ascending and descending, as perpendicular as possible	Winter	**<u>Fine</u>**

Table 9. This table lists the preferred acquisition parameters for the identification of geological features from RADARSAT-1 images in the Canadian High Arctic. Based on our study, we suggest the use of RADARSAT-1 beam modes highlighted in bold and underlined for mapping various geological features in similar arctic environments.

REFERENCES

Bannari, A., J.R. Gibson, and D. Morin, 1997, "The Necessity of Exterior Orientation Parameters for the Rigorous Geometric Correction of MEIS-II Airborne Digital Images", *Remote Sensing Reviews*, Vol. 16, pp.135-156.

Beauchamp, B., J.C. Harrison, and C.M. Henderson, 1989a, "Upper Paleozoic stratigraphy and basin analysis of the Sverdrup Basin, Canadian Arctic Archipelago: Part 1, time frame and tectonic evolution"; in *Current Research*, Part G, Geological Survey of Canada, Paper 89-1G, pp. 105-113.

Beauchamp, B., J.C. Harrison, and C.M. Henderson, 1989b, "Upper Paleozoic stratigraphy and basin analysis of the Sverdrup Basin, Canadian Arctic Archipelago: Part 2, transgressive-regressive sequences"; in *Current Research*, Part G, Geological Survey of Canada, Paper 89-1G, pp. 115-124.

Budkewitsch, P., M.A. D'Iorio, and J.C. Harrison, 1996, "C-band Radar Signatures of Lithology in Arctic Environments: Preliminary Results from Bathurst Island, Northwest Territories"; in *Current Research* 1996-B, Geological Survey of Canada, pp.67-72.

Budkewitsch, P., M.A. D'Iorio, L. Wilkinson, and J. Henderson, 1997, "Radar Images as a Source of Geological Information in Northern Barren Environments"; in *Geomatics in the Era of RADARSAT* (GER'97), Natural Resources Canada / National Defense, 7p.

Denyer, N., R.K. Raney, and N. Shepherd, 1993, "The Radarsat SAR Data Processing Facility", *Canadian Journal of Remote Sensing*, Vol.19, No.4, pp.311-316.

Desrochers, A., M.A. D'Iorio, and É. Gauthier, "Enhancement of the Geologic Mapping of Anticosti Island using SAR data"; in *Geomatics in the Era of RADARSAT* (GER'97), Natural Resources Canada / National Defense.

D'Iorio, M.A., L.N. Ley, P.A. Bubkewitsch, and R. Richardson, 1995, "Geological Map Update Using Airborne and RADARSAT Simulated SAR Data in Sarawak, Malaysia", *Geocarto International*, Vol.10, No.3, pp.43-50.

D'Iorio, M.A., P. Budkewitsch, and N.N. Mahmood, 1997, "Practical Considerations for Geological Investigations using RADARSAT-1 Stereo Images Pairs in Tropical Environments"; in *Geomatics in the Era of RADARSAT* (GER'97), Natural Resources Canada / National Defense, 8p.

Embry, A.F., 1991, "Mesozoic history of the Arctic Islands"; Chapter 14 in *Geology of the Innuitian Orogen and Arctic Platfrom of Canada and Greenland*, H.P. Trettin (ed.); Geological Survey of Canada, Geology of Canada, no.3, pp.369-434.

Ford, J.P., 1998, "Radar Geology"; Chapter 10 in *Principles and Applications of Imaging Radar – Manual of Remote Sensing*, R.A. Ryerson (ed.); John Wiley and Sons, Inc., third edition, Volume 2, pp.511-566.

French, H., 1996, *The Periglacial Environment*, London, Longman, 341 p.

Haneberg, W.C., 1990, "A Lagrangian Interpolation Method for Three-point Problems", *Journal of Structural Geology*, Vol.12, No.7, pp.945-947.

Harris, J., R. Murray, and T. Hirose, 1990, "IHS Transform for Integration of Radar Imagery with other Remotely Sensed Data", *Photogrammetric Engineering and Remote Sensing*, Vol.56, No.12, pp.1631-1641.

Harris, J.R., C. Bowie, A.N. Rencz and D. Graham, 1994, "Computer-Enhancement Techniques for the Integration of Remotely Sensed, Geophysical, and Thematic Data for the Geosciences", *Canadian Journal of Remote Sensing*, Vol.20, No.3, pp.210-221.

Hearty, D.B., D.A. Seeman, P. Maye, and R. Jackson, 1996, "Regional gravity survey of Ellesmere and Axel Heiberg islands, Northwest Territories"; in *Current Research* 1996-B; Geological Survey of Canada, pp.73-79.

Hodgson, D.A., 1991, "The Quaternary record"; Chapter 19 in *Geology of the Innuitian Orogen and Arctic Platfrom of Canada and Greenland*, H.P. Trettin (ed.); Geological Survey of Canada, Geology of Canada, no.3, pp.497-514.

Lewkowicz, A.G., and C.R. Duguay, 1999, "Detection of Permafrost Features Using SPOT Panchromatic Imagery, Forsheim Peninsula, Ellesmere Island, N.W.T.", *Canadian Journal of Remote Sensing*, Vol.25, No.1, pp.34-44.

Lewis, A.J., and F.M. Henderson, 1998, "Radar Fundamentals: The Geoscience Perspective"; Chapter 3 in *Principles and Applications of Imaging Radar – Manual of Remote Sensing*, R.A. Ryerson (ed.); John Wiley and Sons, Inc., third edition, Volume 2, pp.131-182.

Luscombe, A.P., I. Ferguson, N. Shepherd, D.G. Zimcik and P. Naraine, 1993, "The Radarsat Synthetic Aperture Radar Development", *Canadian Journal of Remote Sensing*, Vol.19, No.4, pp.298-310.

Mayr, U., Beauchamp, B., A.F. Embry and J.C. Harrison, 1998, *Geology of Carboniferous, Permian and Triassic formations, parts of Cape Stallworthy and Bukken Fiord, District of Franklin, Northwest Territories*; Geological Survey of Canada, scale 1:125,000.

Okulitch, A.V., and H.P. Trettin, 1991, "Late Cretaceous – Early Tertiary deformation, Arctic

Islands"; Chapter 17 in *Geology of the Innuitian Orogen and Arctic Platfrom of Canada and Greenland*, H.P. Trettin (ed.); Geological Survey of Canada, Geology of Canada, no.3, pp.467-490.

Paradella, W.R., A.R. dos Santos, R. Dall'Agnol, R.W. Pietsch and M.V. Sant'Anna, 1998, "A Geological Investigation Based on Airborne (SAREX) and Spaceborne (RADARSAT-1) SAR Integrated Products in the Central Serra dos Carajás Granite Area, Brazil", *Canadian Journal of Remote Sensing*, Vol.24, No.4, pp.376-392.

Parashar, S., E. Langham, J. McNally, and S. Ahmed, 1993, "Radarsat Mission Requirements and Concept", *Canadian Journal of Remote Sensing*, Vol.19, No.4, pp.280-288.

Plaut, J.J., B. Rivard, and M.A. D'Iorio, 1999, "Radar: Sensors and Case Studies"; Chapter 12 in *Remote Sensing for Earth Sciences – Manual of Remote Sensing*, R.A. Ryerson (ed.); John Wiley and Sons, Inc., third edition, Volume 3, pp.613-642.

RADARSAT Illuminated: Your guide to products and services, 1998, Canada, RADARSAT International, 113 p.

Raney, R.K., 1998, "Radar Fundamentals: Technical Perspective"; Chapter 2 in *Principles and Applications of Imaging Radar – Manual of Remote Sensing*, R.A. Ryerson (ed.); John Wiley and Sons, Inc., third edition, Volume 2, pp.9-130.

Rivard, B., R.L. Kellett, R. Saint-Jean, and V. Singhroy, 1994, "Characterization of fault and dyke intrusion in the Benny Deformation Zone, North Range of Sudbury, from airborne magnetics and SAR", *Canadian Journal of Remote Sensing*, Vol.20, No.3, pp.324-328.

Sabins, F.F.Jr., 1997, *Remote Sensing: Principles and Interpretation*, third edition, New York, W.H. Freeman and Company, 450p.

Singhroy, V., R. Slaney, P. Lowman, J. Harris and W. Moon, 1993, "Radarsat and Radar Geology in Canada", *Canadian Journal of Remote Sensing*, Vol.19, No.4, pp.338-351.

Singhroy, V., and R. St-Jean, 1997, "Guidelines for the Selection of RADARSAT Beam Modes for Geological Mapping"; in *Geomatics in the Era of RADARSAT* (GER'97), Natural Resources Canada / National Defense, 10p.

Singhroy, V., and R. St-Jean, 1998, "Effects of Relief on the Selection of RADARSAT Incidence Angle for Geological Applications"; in *Proceedings of the Final RADARSAT ADRO symposium*, Montréal, Canada, 13-15 October.

Thorsteinsson, R., and H.P. Trettin, 1972a, *Geology Of Bukken Fiord, District of Franklin, Northwest Territories*, Geological Survey of Canada, "A" Series Map 1310A, scale 1:250 000.

Thorsteinsson, R., and H.P. Trettin, 1972b, *Geology Of Cape Stallworthy, District of Franklin, Northwest Territories*, Geological Survey of Canada, "A" Series Map; 1305A, scale 1:250 000

Toutin, T., 1995, "Intégration de données multisources: comparaison de methodes géométriques et radiométriques", *International Journal of Remote Sensing*, Vol.16, No.15, pp.2795-2811.

Toutin, T., 1997, "Qualitative Aspects of Chromo-Stereoscopy for Depth Perception", *Photogrammetric Engineering and Remote Sensing*, Vol.63, No.2, pp.193-203.

Toutin, T., 1998a, "Évaluation de la précision géométrique des images de RADARSAT", *Journal canadien de télédétection*, Vol. 24, No.1, pp.80-88.

Toutin, T., 1998b, "Stereo RADARSAT for Mapping Applications"; in *Proceedings of the Final RADARSAT ADRO symposium*, Montréal, Canada, 13-15 October.

Toutin, T., 1999, "Radar Stereo Pairs for DEM Generation, RADARSAT for Stereoscopy", *GIM International*, Vol.13, No.1, pp.6-9.

Toutin, T., and Carbonneau, Y., 1992, "La création d'ortho-images avec MNE: description d'un nouveau système", *Journal canadien de télédétection*, Vol. 18, No.3, pp.136-141.

Toutin, T., and B. Rivard, 1997, "Value Added Radarsat Products for Geoscientific Applications", *Canadian Journal of Remote Sensing*, Vol.23, No.1, pp.63-70.

Toutin, T., D. Hoja, E. Hoeppner, A. Rémond and C. King, 1998, "GCPs Selection from Multi-source Data Over Mountainous Topography"; in *Proceedings of the IEEE International Geoscience and Remote Sensing Symposium Proceedings*: Volume V, Seattle, USA, CD-ROM, 6-10 July.

Trettin, H.P., 1989, "The Arctic Islands", in Bally, A.W., and Palmer, A.R., eds., *The Geology of North America - An overview*: Boulder, Colorado, Geological Society of America, The Geology of North America, v.A., p. 349-370.

Trettin, H.P., 1991, "Tectonic Framework"; Chapter 4 in *Geology of the Innuitian Orogen and Arctic Platfrom of Canada and Greenland*, H.P. Trettin (ed.); Geological Survey of Canada, Geology of Canada, no.3, pp.57-66.

Trettin, H.P., 1996, *Geology, parts of Cape Stallworthy and Bukken Fiord, District of Franklin, Northwest Territories*, Geological Survey of Canada, Map 1884A, scale 1:250 000.

Trettin, H.P., 1998, *Pre-Carboniferous Geology of the Northern Part of the Arctic Islands*, Isotopic Age Determination by J.E. Gabites and Paleontological Appendices by B.S. Norford, T.T. Uyeno, M.J. Copeland, T.A. de Freitas and others, Geological Survey of Canada, Bulletin 425, 401 p.

Ulaby, F.T., 1982, "Radar Signatures of Terrain: Useful Monitors of Renewable Resources", *Proceedings of the IEEE*, Vol. 70, No. 12, pp.1410-1428.

Ulaby, F.T., Moore, R.K., and Fung, A.K., 1986, *Microwave Remote Sensing: Active and Passive, Volume III: From Theory to Applications*, Artech House, Norwood, MA, pp.1065-2162.

Webster, T., B.J. Murphy, and S.M. Barr, 1997a, "Remote Sensing and GIS analysis of the St.Marys Basin, Central Nova Scotia"; in *Geomatics in the Era of RADARSAT* (GER'97), Natural Resources Canada / National Defense, 18p.

Webster, T., D. Raymond, and M.S. Akhavi, 1997b, "Preliminary Analysis of Spaceborne Radar Imagery Integrated with Geoscience Datasets for Central Nova Scotia"; in *Geomatics in the Era of RADARSAT* (GER'97), Natural Resources Canada / National Defense, 16p.

APPENDIX 1: GLOSSARY

Source: Raney, R. Keith, 1999, Radar Glossary, Johns Hopkins University, Applied Physics Laboratory, 11100 Johns Hopkins Road, Laurel, MD 20723-6099.

AZIMUTH

The relative position of an object within the field of view of an antenna in the plane intersecting the moving radar's line of flight. The term is commonly used to indicate linear distance or image scale in the along-track direction.

AZIMUTH RESOLUTION

Resolution characteristic of the azimuth dimension, usually applied to the image domain. Azimuth resolution is fundamentally limited by the Doppler bandwidth of the system. Excess Doppler bandwidth is usually used to allow extra looks, at the expense of azimuth resolution.

BACKSCATTER

The (microwave) signal reflected by elements of an illuminated scene back in the direction of the radar. It is so named to make clear the difference between energy scattered in arbitrary directions, and that which returns to the radar and thus may be received and recorded by the sensor.

BRIGHTNESS

Property of a radar image (digital or optical) in which the observed strength of the radar reflectivity is expressed as being proportional to a digital number (digital image file) or to a gray scale mapping, which, for a photographic positive, shows "bright" as "white".

C-BAND

Microwave band in which the wavelengths are at or near 5.6 cm.

CANADA CENTRE FOR REMOTE SENSING (CCRS)

The leading centre in Canada for the development of imaging radar and other remote sensing applications and technology.

CANADIAN SPACE AGENCY (CSA)

Organisation located in St. Hubert, Québec, Canada.

CONTRAST

Difference between the tone of two neighbouring regions.

CORNER REFLECTOR

Combination of two or more intersecting specular surfaces that combine to enhance the signal reflected back in the direction of the radar. Strongest reflection is obtained when the materials are good conductors.

DIELECTRIC

Material which has neither "perfect" conductivity nor is perfectly "transparent" to electromagnetic radiation. The electrical properties of all intermediate materials, such as ice, natural foliage, or rocks, may be described by two quantities: relative dielectric constant and loss tangent. Reflectivity of a smooth surface and the penetration of microwaves into the material are determined by these two quantities.

DIELECTRIC CONSTANT

Fundamental (complex) parameter, also known as the complex permittivity, that describes the electrical properties of a lossy medium. (See permeability.) By convention, the relative dielectric constant of a given material is used, defined as the (absolute) dielectric constant divided by the dielectric constant of "free space". The (relative) dielectric constant is usually defined as $\varepsilon = \varepsilon' - j\varepsilon''$ (It is common practice to refer to the real component ε' as "the dielectric constant", whose partner, the loss tangent, accounts for ε''.)

DIGITAL NUMBER (DN)

A number, between zero and 255 for example, assigned to each spatial grid position in the file representing the brightness levels of an image. The digital numbers may be related to sigma nought of scene elements through the process of calibration.

DYNAMIC RANGE

A description of the variety of signal amplitudes (or power levels) available in a system, or present in a data file. Dynamic range is specified either i) to be within minimum and maximum values, or ii) with respect to the ratio of maximum to minimum values. The most important specification is linear dynamic range over which signals combine according to the property of linearity.

FORESHORTENING

Spatial distortion whereby terrain slopes facing a side-looking radar's illumination are mapped as having a compressed range scale relative to its appearance if the same terrain were level.

Foreshortening is a special case of elevation displacement. The effect is more pronounced for steeper slopes, and for radars that use steeper incidence angles. Range scale expansion, the complementary effect, occurs for slopes that face away from the radar illumination.

FREQUENCY

Rate of oscillation of a wave. In the microwave region, frequencies are on the order of 1 GHz (Gigahertz) to 100 GHz. ("Giga" implies multiplication by a factor of a billion.) For electromagnetic waves, the product of wavelength and frequency is equal to the speed of propagation, which, in free space, is the speed of light.

GROUND RANGE

Range direction of a side-looking radar image as projected onto the nominally horizontal reference plane, similar to the spatial display of conventional maps. For spacecraft data, an Earth geoid model is used, whereas for airborne radar data, a planar approximation is sufficient. Ground range projection requires a geometric transformation from slant range to ground range, leading to relief or elevation displacement, foreshortening, and layover unless terrain elevation information is used.

HERTZ

Named after H. R. Hertz, a 19th century German physicist, it is the standard unit for frequency, equivalent to one cycle per second.

IMAGE

Mapping of the observed radar reflectivity of a scene. For radars with digital image processing, the image consists of a file of digital numbers assigned to spatial positions on a grid of pixels, and presented either as hard copy (such as a photographic print) or soft copy (such as a digital data record). All radar images are subject to statistical variations, mainly speckle and noise, which must be accommodated in either visual or numerical image interpretation. The most commonly used image formats occur after detection. After calibration (and compensation for speckle and noise effects), image files from magnitude squared detection are proportional, on average, to sigma nought σ^0. Magnitude scaling (formed by taking the square root of the detected, look-summed file to yield an image proportional to $(\sigma^0)^{1/2}$ is the "standard" for most SAR image files. A magnitude image often yields a photographic copy that is more readily interpreted visually, and requires less dynamic range and data storage space. A digital SAR image file may be retained in complex format (before detection) for specialized applications.

INCIDENCE ANGLE

Angle between the line of sight from the radar to an element of an imaged scene, and a vertical direction characteristic of the scene. The definition of "vertical" for this purpose is important. One must distinguish between the (nominal) "incidence angle" determined by the large scale geometry of the radar and the Earth's geoidal surface, and the local incidence angle which takes into account the mean slope with each pixel of the image. Smaller incidence angle refers to viewing line of sight being closer to the (local) vertical, hence "steeper". (See aspect angle.) In general, reflectivity from distributed scatterers decreases with increasing incidence angle.

LAYOVER

Extreme form of elevation displacement or foreshortening in which the top of a reflecting object (such as mountain) is closer to the radar (in slant range) than are the lower parts of the object. The image of such a feature appears to have fallen over towards the radar. The effect is more pronounced for radars having smaller incidence angle.

LOOKS

Each of the sub-images used to form the output summed image, implemented in a SAR processor.

Speckle, the radiometric uncertainty in each estimate of the scene's reflectivity, is reduced by the averaging implied by adding together different detected images of the same scene. For N statistically independent looks (which may be implemented in various ways), the standard deviation of each estimate is reduced by $N^{1/2}$. Multiple looks may be generated by averaging over N_r range and/or N_a azimuth resolution cells. For an improvement in radiometric resolution using multiple looks there is an associated degradation in spatial resolution. Note that there is a difference between the number of looks physically implemented in a processor, and the effective number of looks as determined by the statistics of the image data.

MICROWAVE

An electromagnetic wavelength in (or near) the span 1-100 cm.

NOISE

Any unwanted or contaminating signal competing with the desired signal. In a SAR, two common kinds of noise are additive (receiver) noise and signal dependent noise, usually either additive or multiplicative. The relative amount of additive noise is described by the signal-to-noise ratio. Signal dependent noises, such as azimuth ambiguities or quantization noise, arise from system imperfections, and are dependent on the strength of the signal itself. "Good" SAR systems usually keep these noise levels below acceptable levels, by design. (Speckle is sometimes considered to be a kind of signal dependent multiplicative noise in a SAR system.)

PARALLAX

Apparent change in the position of an object due to an actual change in the point of view of observation. For a SAR, true parallax occurs only with viewpoint changes that are away from the nominal flight path of the radar. In contrast to aerial photography, parallax cannot be created by forward and aft looking "exposures". Parallax may be used to create stereo viewing of radar images.

PENETRATION

Act of microwaves entering a medium such as dry sand or forest leaf canopy. Microwave penetration, in general, is proportional to the wavelength, and inversely proportional to the loss tangent. The penetration depth D_{pen} for most natural materials (except highly conductive media such as water) encountered in radar remote sensing is given by $D_{pen} = \lambda/(\pi \tan\delta)$, where λ is the wavelength, and $\tan\delta$ is the loss tangent.

PIXEL

Term derived from "picture element" in a digital representation to indicate the spatial position of a sample of an image file, which consist of a spatial array of digital numbers. A two-dimensional ensemble of pixels forms the geometric grid on which an image is built. The fundamental parameter describing this grid is the inter-pixel spacing in each of the two image directions. (To confuse matters, pixel spacing is often referred to as "pixel" or "pixel size" in the literature. Pixel "size" is to be avoided.)

POLARIZATION

Orientation of the electric (E) vector in an electromagnetic wave, frequently "horizontal" (H) or "vertical" (V) in conventional imaging radar systems. Polarization is established by the antenna, which may be adjusted to be different on transmit and on receive. Reflectivity of microwaves from an object depends on the relationship between the polarization state and the geometric structure of the object. Common shorthand notation for band and polarization properties of an image file is to state the band, with a subscript for the receive and the transmit state of polarization, in that order. Thus, for example, LHV indicates L-band, horizontal receive polarization, and vertical transmit polarization. Possible states of polarization in addition to vertical and horizontal include all angular orientations of the E vector, and time varying orientations leading to elliptical and circular polarizations. (See quadrature polarization.)

PROCESSING

Sometimes denoted "preprocessing", it is the means of converting the received reflected signal into an image. Processing consists of image focusing through matched filter integration, detection, and multi-look summation. The output files of a SAR processor usually are presented with unity aspect ratio (so that range and azimuth image scales are the same). Images may be either in slant range or ground range projection. Both of these spatial adjustments require resampling of the image file.

RADAR

Electromagnetic sensor characterized by RAdio Detection And Ranging, from which the acronym RADAR is derived. Predicted in the early part of the 20th century, the first important system was built in England in 1938. Basic building blocks of a radar are the transmitter, the antenna (normally used for both transmission and for reception), the receiver, and the data handling equipment. A synthetic aperture radar system, by implication, includes an image processor, even though it may be remotely located in time or space from the radar electronics.

RANGE

Line of sight distance between the radar and each illuminated scatterer (see one-way).
In SAR usage, the term is also applied to the dimension of an image away from the line of flight of the radar. (See slant range and ground range.)

RANGE RESOLUTION

Resolution characteristic of the range dimension, usually applied to the image domain, either in the slant range plane or in the ground range plane. Range resolution is fundamentally determined by the system bandwidth in the range channel.

RELIEF DISPLACEMENT

Image distortion in the range direction of a side and downward looking radar caused by terrain features in the scene being above (or below) the reference elevation contour, and thus in fact being closer to (or further from) the radar than their planimetric position. The effect may be used to create radar stereo images (see parallax). It may be removed from an image through independent knowledge of the terrain profile. In many applications, an approximate correction may be derived through shape from shading techniques.

RESOLUTION (RADAR)

Generally (but loosely) defined as the width of the "point spread function", the "Green's function", or the " impulse response function", depending on whether one has an optics, a physics, or an electronic systems background. More properly, "resolution" refers to the ability of a system to differentiate two image features corresponding to two closely spaced small objects in the illuminated scene when the brightness of the two objects in question are comparable and fall within the dynamic range of the radar in question. (Definition adapted from Lord Rayleigh [1879]). "Higher resolution" refers to a system having a smaller impulse response width.

RESOLUTION CELL

A three-dimensional cylindrical volume surrounding each point in the scene. The cell range depth is slant range resolution, its width is azimuth resolution, and its height, which is conformal to the illumination wavefront, is limited only by the vertical beam width of the antenna pattern. Resolution cell often is defined with respect to the local horizontal. (See ground range).

ROUGHNESS

Variation of surface height within an imaged resolution cell. A surface appears "rough" to microwave illumination when the height variations become larger than a fraction of the radar wavelength. The fraction is qualitative, but may be shown to decrease with incidence angle.

SAR

Synthetic Aperture Radar, so-called because azimuth resolution is achieved through computer operations on a set of (coherently recorded) signals such that the processor is able to function like a large antenna aperture in computer memory, thus realizing azimuth resolution improvement in proportion to aperture size. The SAR concept was introduced by C. Wiley (USA) in 1951.

SHADOW

From an optical point of view as seen from the position of a radar, a region hidden behind an elevated feature in the scene would be out of sight. This region corresponds to that which does not get illuminated by the radar energy, and thus is also not visible in the resulting radar image. The region is filled with "no reflectivity", which appears as small digital numbers, or a dark region in hard copy.

SPECKLE

Statistical fluctuation or uncertainty associated with the brightness of each pixel in the image of a scene. A single look SAR system achieves one estimate of the reflectivity of each resolution cell in the image. Speckle may be reduced, at the expense of resolution, in the SAR processor by using several looks. Speckle appears as a multiplicative random process whose variance and spatial correlation are determined primarily by the SAR system.

TEXTURE

Second order spatial average of brightness. Scene texture is the spatial variation of the average reflectivity. For areas of nominally constant average reflectivity, image texture consists of scene texture multiplied by speckle.

TONE

First order spatial average of image brightness, often defined for a region of nominally constant average reflectivity.

TOPOGRAPHIC DISPLACEMENT

Alternative term for relief displacement.

WAVELENGTH (λ)

Minimum distance between two events of a recurring feature in a periodic sequence, such as the crests in a wave. (Units of length, such as metres).